Punctual acoustic-wave therapy for the super-selective ablation of squamous cell carcinoma

Inaugural dissertation

for the attainment of the title of doctor
in the Faculty of Mathematics and Natural Sciences
at the Heinrich Heine University Düsseldorf

presented by

Maja Strugačevac
from Osijek

Düsseldorf, November 2018

from the Institute of Applied Physics
at the Heinrich Heine University Düsseldorf

Published by permission of the
Faculty of Mathematics and Natural Sciences at
Heinrich Heine University Düsseldorf

Supervisor: Prof. Dr. Mathias Getzlaff
Co-supervisor: Prof. Dr. med. Dr. h.c. Jörg Schipper

Date of the oral examination:

23.01.2019

Abstract

This dissertation summarizes the author's work on the development of new, cell-selective treatment strategies for tumors originating from the head and neck area. This work comprises of three main parts: determination of suitable staining parameters for the observed cell lines, characterization of the cells and acoustic wave irradiation.

As all the measurements were made using a fluorescence confocal laser scanning microscope, the suitable staining concentration and staining time had to be determined. In this way, the image quality can be ensured and the influence of the method used on the cells can be minimized.

In a second part the morphology of the cells was observed to find the differences between healthy, dysplastic and cancerous cells. The differences in cytoskeleton filaments may lead to the differences in the elasticity of the cells which is of great importance for the development of a new cancer treatment based on the mechanical properties of the cells.

The third part of this thesis deals with the irradiation of the cells using acoustic waves exhibiting frequencies from 0.5 kHz to 10.0 kHz. The main aim was to observe whether those acoustic waves can induce a resonance catastrophe which would lead to a cell death. The reaction of the cells on the variation of the frequency, the oscillation amplitude, the irradiation duration and the probe-cells distance was observed to investigate whether the change of those parameters induces different reactions of the cells.
The parameter set on which the cells react the most was determined. The observed cancer and dysplastic cells were then irradiated using this parameters to examine the reaction of different cell lines on the same parameter set. The different reaction of the cells indicates that the therapy has to be adjusted for every patient individually.

This thesis presents fundamental results of great importance for further research and the development of super-selective ablation of cancer cells.

Contents

1 Introduction **1**

2 Theoretical background **3**
2.1 Biological background of the cells 3
2.1.1 Cell structure and function 3
2.1.2 Epithelium 6
2.1.3 Cell cycle and cell death 7
2.1.4 Characteristics of cancer cells 9
2.2 Solid body deformation 10
2.2.1 Elastic deformation 10
2.2.2 Elasticity of cells 13
2.3 Fluorescence microscopy 14
2.3.1 Fluorescence 14
2.3.2 Confocal Laser Scanning Microscopy 16
2.3.3 Fluorochromes 17
2.3.4 Fluorescence microscopy problems 18
2.4 Sound 19
2.4.1 Acoustic waves 19
2.4.2 Generation of acoustic waves 21
2.4.3 Sonication of cells 22

3 Materials and methods **24**
3.1 Cell lines and cell culture 24
3.1.1 Cell lines 24
3.1.2 Cell culture 25
3.2 Cell preparation for live cell imaging 26
3.2.1 Used fluorochromes 27
3.2.2 Cell staining procedure 28
3.3 Live cell imaging 29
3.3.1 Olympus Fluoview 1000 29
3.3.2 Cell imaging procedure 32
3.3.3 Data analysis 33
3.4 Acoustic wave irradiation 36
3.4.1 Experimental setup 36
3.4.2 Irradiation of the cells 38
3.4.3 Data analysis software 39

4 Results and discussion **42**
4.1 Suitable staining parameters 42
4.1.1 Determination of suitable staining parameters 42
4.1.2 CellMask Green 45
4.1.3 Cytoskeleton staining kits SiR-actin and SiR-tubulin 45
4.1.4 Hoechst 33342 46
4.1.5 MitoTracker Orange 46
4.2 Morphology of the cells 47
4.2.1 Overall cell volume 47
4.2.2 Cytoskeleton filaments 51
4.2.3 Cell nuclei 61
4.2.4 Mitochondria 62
4.2.5 Remarks 66
4.3 Acoustic wave irradiation of the cells 66
4.3.1 Characterization of the probe 66
4.3.2 Frequency variation 70
4.3.3 Variation of irradiation duration 76
4.3.4 Input voltage variation 78
4.3.5 Probe-cells distance variation 80
4.3.6 Irradiation of cancer and dysplastic cells 82
4.3.7 Irradiation of co-cultivated cells 89

5 Conclusion and outlook **93**

Appendices

Appendix A **97**
A.1 Concentration variation of SiR-tubulin for UD-SCC-01 cells 97
A.2 Staining time variation of SiR-tubulin for cell line UD-SCC-01 . . . 98

Appendix B **99**
B.1 Concentration variation of SiR-actin for UD-SCC-01 cells 99
B.2 Staining time variation of SiR-actin for cell line UD-SCC-01 100

Appendix C **101**
C.1 Concentration variation of Hoechst 33342 for UD-SCC-01 cells . . . 101
C.2 Staining time variation of Hoechst 33342 for cell line UD-SCC-01 . 102

Appendix D **103**
D.1 Concentration variation of MitoTracker Orange for UD-SCC-01 cells 103
D.2 Staining time variation of MitoTracker Orange for cell line UD-SCC-01 104

Appendix E **105**
E.1 Nuclei cross section of all observed cell lines 106
E.2 Distribution of the cell nuclei to overall cell volume ratios for all cell line used 107

Appendix F **108**
F.1 Reaction of the UD-SCC-01 cells on irradiation with acoustic waves 108
F.2 Reaction of the UD-SCC-04 cells on irradiation with acoustic waves 109
F.3 Comparison of the UD-SCC-04 and UD-SCC-01 cells' reaction on acoustic waves treatment 110

Appendix G **111**
G.1 Variation of irradiation duration for cell line UD-SCC-01 111
G.2 Variation of irradiation duration for cell line UD-SCC-04 112

Appendix H **113**
H.1 Variation of input voltages for UD-SCC-01 cells 113
H.2 Variation of input voltages for UD-SCC-04 cells 113
H.3 Cell reaction on input voltage variation for UD-SCC-01 cells 114
H.4 Cell reaction on input voltage variation for UD-SCC-04 cells 114

Appendix I **115**
I.1 Cell reaction on probe-cells distance variation for UD-SCC-01 cells . 115

Appendix J **116**
J.1 Reaction of densely populated monolayers on acoustic wave irradiation 116
J.2 Reaction of non-densely populated monolayers on acoustic wave irradiation 116

Bibliography **122**

Publications **123**

Conference contributions **124**

Acknowledgements **126**

Eidesstattliche Versicherung **127**

1. Introduction

One of the most challenging diseases with very high mortality rate nowadays is cancer. It is a disease caused by genetic mutation of the cells causing them to have a high proliferation rate, grow abnormally and invade the surrounding tissue. Despite excessive cancer research, the number of patients increases daily. Squamous cell carcinoma located at the head and neck area is the fifth most common cancer worldwide [1] and oral cavity cancers have a survival rate of 61% for the first 5 years after the treatment [2].

Current treatments consider surgical removal of the tumor, chemotherapy and irradiation therapy. Nevertheless, these are in some cases not applicable or not effective enough to overcome the disease. In addition, the side effects of the treatments are often unpleasant and painful for the patients. The great disadvantage of all therapies is that the healthy tissue surrounding the tumor is also affected by the treatment. Therefore, additional cancer research and search for new treatment methods is indispensable. The investigation of cancer cell mechanics and morphology has the potential to elucidate the cell properties and to drive the development of more effective cancer treatments.

A working group at the Institute of Applied Physics at Heinrich Heine University in Düsseldorf, in cooperation with Düsseldorf University Hospital, Department of Otorhinolaryngology, is working on the development of a new, more effective cancer therapy. This thesis was created as a part of the aforementioned project. The main idea behind the new therapy is to induce a resonance catastrophe in cancer cells and initiate the cell death.

A resonance catastrophe can be induced when the observed system is forced to oscillate with its resonance frequency. Periodically applied forces make the system oscillate, the oscillation amplitude increases until the system reaches its limit and collapses. In case of cancer cells, this can be achieved by acoustic wave irradiation. These acoustic waves can induce the oscillation of the cells. If the oscillation frequency is close to the resonance frequency of the cells, they can be destroyed. On one hand, the acoustic wave frequency can be matched to the resonance frequency of the cell membrane which would lead to membrane rupture and cell death called necrosis. On the other hand, the frequency can be matched to the resonance frequency of the cell organelles, e.g., cytoskeleton or cell nucleus, which can be destroyed what would induce cell death as well. In this case apoptosis may be initiated, which would reduce the risk of inflammation.

The proportionality between the resonance frequency and the elastic modulus plays an important role in the development of the new therapy. Different working groups have shown that the elastic modulus of cancer cells is notably reduced

when compared to healthy cells [3, 4, 5]. As there is a proportionality between the resonance frequency and the elastic modulus of the cells, it is possible to expect that cancer cells react on lower frequencies, which do not affect healthy cells. This enables a cell-selective treatment where the cell death of the cancer cells could be induced without influencing healthy cells.

The main focus of this project at Heinrich-Heine-University Düsseldorf is on squamous cell carcinoma cells originating from the head and neck area. Therefore, during this thesis, investigations on four cancer, one dysplastic and one healthy cell line from this area were made. As the cells were observed under a confocal laser scanning microscope, suitable staining parameters had to be determined. Afterwards, a detailed characterization of the cells was made. The size, shape, volume and the way the cells grew was investigated to find the differences between the cells. Moreover, the microtubules and actin filaments were characterized as the elasticity of the cells is mainly determined by the cytoskeleton. In the last step, the irradiation of the cells using acoustic waves exhibiting frequencies between 0.5 kHz and 10.0 kHz was made to observe whether those waves induce a resonance catastrophe leading to a cell death. Different parameters like frequency, oscillation amplitude, irradiation duration and probe-cells distance were varied to investigate whether and how those parameters influence the degree of cell reaction.

2. Theoretical background

In the following chapter the fundamental knowledge relevant for the rest of this thesis will be elucidated. The first part is dedicated to the biology of a cell. A brief introduction of the cell structure and function, as well as the cell cycle will be given. The transformation from healthy to cancerous cells and the characteristic properties of cancer will be illustrated as well. In the second part physical aspects like elasticity, fluorescence, confocal microscopy and sound waves and their generation will be explained in detail.

2.1 Biological background of the cells

Cells are the smallest structured and functional units of life. They can be categorized as prokaryotic and eukaryotic cells. Prokaryotic cells include bacteria and archaea which are more simply structured organisms compared to eukaryotic cells. One of the main differences between the two cell types is the lack of nuclei in prokaryotic cells. As the human body consists of eukaryotic cells, they will be in the focus during this thesis. [6]

2.1.1 Cell structure and function

Eukaryotic cells are complexly structured units with clearly defined functions of every cell subunit. These specialized subunits are called cell organelles. Even though human body cells are differentiated by their functions and complexity, most of the cell's organelles and functions are identical for all cell types. Some of these functions are transport and metabolic processes, cell motility and division. Figure 2.1 shows the structure of eukaryotic cells. The cell organelles of interest for this thesis are highlighted and will be explained in the following.

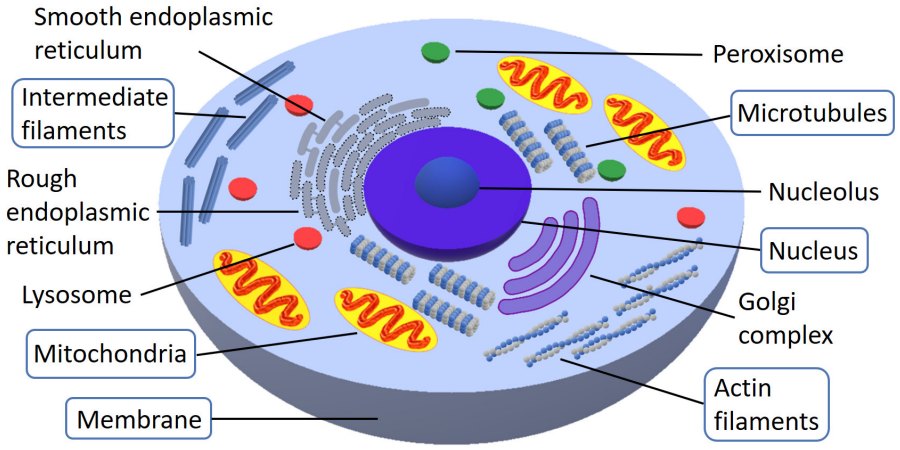

Figure 2.1: Structure of an eukaryotic cell with highlighted organelles of interest for this thesis.

The **cell membrane** is the boundary of the cell that separates all the cell components from the environment. Its structure is explained with the fluid mosaic model proposed by J.Singer and G. Nicolson as shown in Figure 2.2. Outer and inner hydrophilic protein layers surround a lipid bilayer which consists of polar hydrophilic lipid ends and non-polar hydrophobic inner regions. [7]

The cell membrane possesses selective permeability to control the transport of substances into and out of the cell. The cell membrane is, among other, also involved in processes like cell adhesion and signaling allowing the cell to adopt itself to the outside environment and its changes. [8]

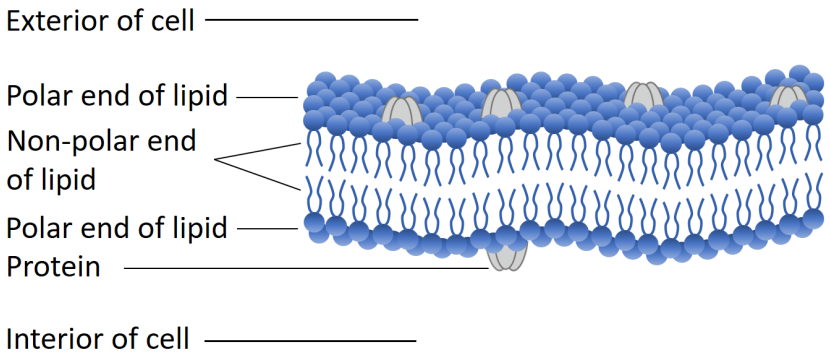

Figure 2.2: Cell membrane structure

Cytoplasm and **cell nucleus** are encapsuled by the cell membrane. The cytoplasm comprises cell organelles and cytosol (intracellular fluid). The cell nucleus contains hereditary material and controls the activity of the cell by regulating gene expression. It consists of three important parts: nuclear membrane, nucleolus and chromosomes. The nuclear membrane has two cellular membranes and separates the genetic material from the cytoplasm. The nucleolus is a nuclear structure not surrounded by a nuclear membrane. Its main function is to synthesize ribosomal ribonucleic acid (rRNA) and assemble ribosome. Chromosomes are composed of chromatin fibers containing the genetic material of the cell. [6]

The main role of **mitochondria** is the production of adenosine triphosphate (ATP). Apart from generating energy for the cell, mitochondria also take part in lipid synthesis, ancient DNA replication as well as in the apoptotic cascade. As it contains two membranes, a mitochondrion is divided into four distinct parts: the outer membrane, intermembrane space, inner membrane and the matrix where each of those parts performs one of the mitochondrial functions. [9]

Organization of the cell organelles, cell stability and movement are some of the main functions of the **cytoskeleton**. It consists of three main proteins: microtubules, intermediate and actin filaments shown in Figure 2.3. Each of these proteins will be explained in detail.

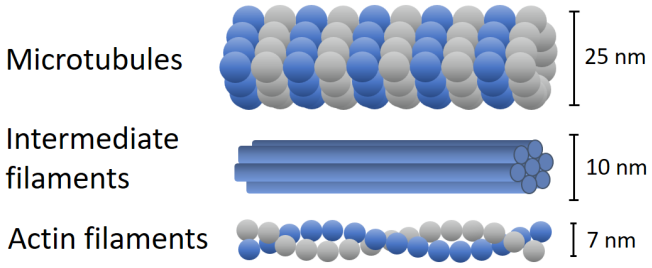

Figure 2.3: Cytoskeleton proteins: microtubules, intermediate and actin filaments

Microtubules are the largest and stiffest cytoskeleton proteins. By polymerization of alpha and beta tubulin, polymers called protofilaments are formed. Thirteen such polymers make microtubules, which are polar molecules with positive and negative ends. Positive ends are able to grow fast or polymerisate, negative ends are able to lose subunits or depolymerisate. [6]

During cell division, microtubules play an important role in intracellular traffic. When the cell division starts, the cytoplasmic network of microtubules diassembles and rearranges into a mitotic spindle. In this phase, the main function of the cytoskeleton is to find the chromosomes, align them and divide them to daughter cells. Microtubules build up cilia and flagella, the contractile filamentous appendages of the cytoplasm important for cell movement and other mechanical functions. Even though signal transduction mechanisms are still not very well understood, the connection between a drug-mediated depolymerization of microtubules and gene expression was observed as well. [6, 10, 11]

Intermediate filaments are about 10 nm large and the most flexible cytoskeleton proteins. Depending on the cell type, intermediate filaments are composed of different proteins. There are six groups of proteins, based on the similarities of their amino acid sequences. Type one are acidic and type two neutral or basic keratins which can be expressed by epithelial cells. Type three is, e.g., vimentin found in fibroblasts or white blood cells. Type four are neurofilament proteins expressed by neurons. Nuclear lamins are the fifth protein type found in nuclear lamina of all cell types. The last type of intermediate proteins are nestin proteins, expressed by stem cells of the central nervous system. [12]

The functions of intermediate filaments are mostly determined by the proteins they consist of. Among other, intermediate filaments are involved in maintaining the shape of cell and nucleus as well as regulating cell motility and adhesion. [13]

Actin filaments are the smallest cytoskeleton proteins, less rigid then microtubules but more than intermediate filaments. Like microtubules, actin filaments are polarized polymers. They can be found as free monomers called G-actin (globular) or a linear polymer microfilament called F-actin (filamentous).

Actin filaments are involved in many cellular processes. The actin protein network maintains the cell shape and allows cell signaling. Due to fast assembling and disassembling, they enable cell motility and migration. During mitosis, the actin filaments network is rearranged to form rounded cells with increased cortical rigidity. After mitosis, this network is again reorganized in the way that the cell can regain its usual shape and attach to the substrate. Due to their function, actin filaments have a great impact on the mechanical properties of cells. [10, 14]

2.1.2 Epithelium

Epithelial tissue, also known as epithelium, is – together with connective, muscle and nervous tissue – one of four basic tissue types. It is a continuous sheet of tightly joined cells with almost no intercellular space, covering a body's or organ's surface. Epithelial tissue can be classified as simple epithelium with a single cell layer or stratified epithelium as cell multilayer. Both of this types can be further classified as squamous, cuboidal or columnar, based on the surface cell's shape. A detailed epithelial tissue classification is shown in Figure 2.4. [15]

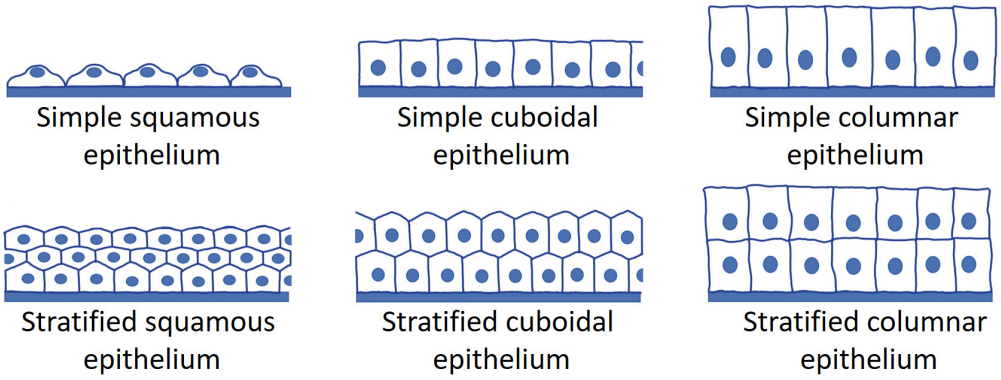

Figure 2.4: Epithelium classification

Epithelial cells are interconnected through junctions, multiprotein complexes which ensure communication between neighbouring cells. Through the basement membrane the epithelial cells are connected with the underlying tissue. The main task of the epithelial tissue is to protect the underlying tissue from infection, mechanical damage, desiccation or ultraviolet radiation. Epithelial cells also regulate the exchange of substances between body cavity and underlying tissue or serve as receptor cells as they are exposed to external influences. [16]

The functions of the epithelium depend on its type. In focus of this thesis are squamous epithelial cells. They are categorized as monolayer or multilayer. A simple squamous epithelium is a monolayer composed of flattened and mostly irregular shaped cells. This kind of epithelium forms thin tissues and is involved in passive transport of substances. It can be found, among other, in the alveolus

or blood capillaries. Contrary to the simple squamous epithelium, the stratified squamous epithelium is composed of a number of cell layers upon a basement membrane. Different layers contain different cell types. Cells at the surface are flattened, but the cells close to the basement membrane can be cuboidal. The function of the stratified squamous epithelium is to protect the underlying tissue from abrasions, since surface cells can be replaced before the basement membrane or underlying tissue is damaged. It can be found in the oral cavity, pharynx, anal canal, cervix or vagina. [17]

2.1.3 Cell cycle and cell death

The cell cycle describes the events from the formation of a cell from the mother cell until the end of the division into two daughter cells. This cycle is divided in two main phases: interphase and cell division phase which can both be subdivided in further ones. A schematic overview of the cell cycle is shown in Figure 2.5.

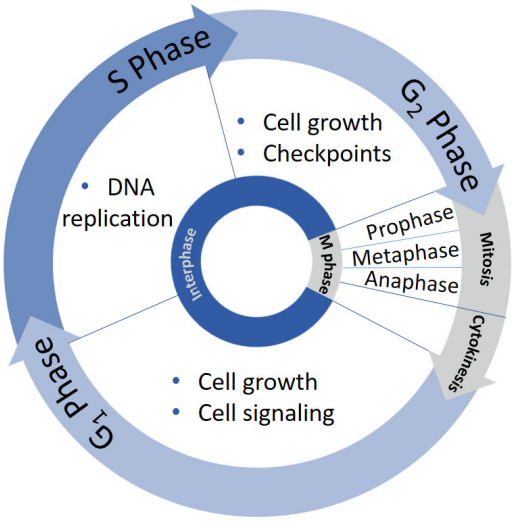

Figure 2.5: Cell cycle phases

After the division from the mother cell, a cell enters the first gap phase called $\mathbf{G_1}$. This phase is characterised with cell growth. In G_1 phase most of the cells get intracellular or extracellular signals which determine whether the cell cycle will be continued and the cell will further divide or not. If the cell continues the cell cycle, it enters synthesis or **S phase** where deoxyribonucleic acid (DNA) is replicated and chromosomes are duplicated. The proteins open the DNA double helix which is then ready for the DNA syntheses. During this process, enzymes copy two DNA strands which are then packed into chromosomes. When the DNA replication and chromosome duplication is finished, the cell enters the $\mathbf{G_2}$ **phase**. As in G_1 phase, the cell continues to grow during this phase. Control mechanisms, also called checkpoints, ensure that the cell is ready for the next phase.

This is the **M phase** in which the cell goes through two main processes: **mitosis**, i.e. nuclear division, and **cytokinesis**, i.e. cell division. During mitosis the duplicated chromosomes are equally divided into two daughter nuclei. In early mitosis (prophase) chromosomes are attached to a mitotic spindle which then in

the next part of mitosis, called metaphase, aligns the chromosomes in one plane also known as metaphase plate. In the next phase (anaphase) the chromosomes are divided and pulled to the opposite sides of the cell. Two chromosome sets are herewith divided into two daughter nuclei. During cytokinesis, the rest of the cell divides and forms, together with the two nuclei, two daughter cells. When two identical daughter cell have been produced, the cell cycle ends and a new cell cycle for both daughter cells starts. For healthy cells, this cycle cannot repeat indefinitely, but reaches a limit. This limit is called proliferation maximum. [18]

When the cell reaches its proliferation maximum or mutations during cell division occur, the programmed cell death starts. This is in most cases apoptosis. On the other hand, external influences like mechanical trauma, infections, frostbite, etc. can induce cell death as well. This type of cell death is called necrosis. Figure 2.6 shows the processes of both, apoptosis and necrosis.

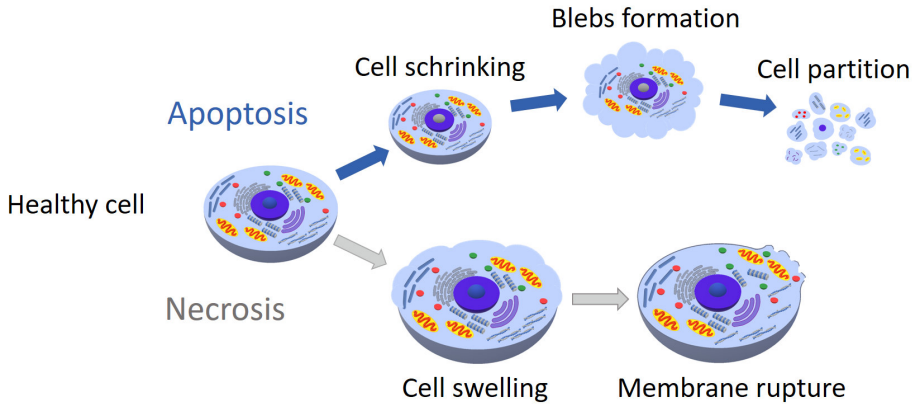

Figure 2.6: Apoptosis and necrosis processes

The **apoptosis** is initiated by intrinsic or extrinsic pathways. The intrinsic or mitochondrial pathway is activated by the cell itself in cases of DNA damage, cytoskeletal disruption, unfolded protein accumulation or others. The extrinsic pathway is triggered by signals received trough extracellular death receptors on the cell surface.

During apoptosis the DNA is fragmented, chromosomes condensed, all intercellular components decomposed and the cell membrane forms so-called blebs. Decomposed intracellular fragments get inside of a bleb and together they form apoptotic bodies which are then separated from the cell. In this way the whole cell is partitioned into small portions which undergo phagocytosis. During apoptosis all cell content remains inside of the cell membrane and is not spread into the extracellular space. Thus, inflammation is avoided. [19]

Unlike apoptosis, **necrosis** is a passive type of cell death induced by external influences. During necrosis various cell organelles distend, DNA disassembles randomly and the cell swells. When the cell swelling has reached its maximum the cell membrane ruptures and the cell content spreads into extracellular space, possibly causing inflammation. The cell residues are then eliminated by phagocytes. [20]

2.1.4 Characteristics of cancer cells

The term cancer is related to a type of diseases caused by genetic mutations which manifests through abnormal growth of tissue cells and possible invasion in surrounding tissue or other body parts. Multiple mutations of the genes responsible for cell growth and reproduction (oncogenes) and/or the genes which control cell cycles and trigger apoptosis (tumor suppressor genes) lead to cancer. If a cell with such mutations proliferates, accumulation of abnormal cells called dysplasia occurs. Those cells are genetically modified and abnormal in comparison to the surrounding tissue cells, but still not cancer cells. If those cells further proliferate, a primary tumor arises. By migration of its cells, the primary tumor can spread and affect other body parts by developing secondary tumors or metastases. Figure 2.7 shows the grading steps in transformation from healthy to cancerous cells. Although the cause of the genetic mutations leading to cancer is still not fully clarified, external influences like smoking, obesity, radiation or inherited predisposition can increase the risk of those. [21]

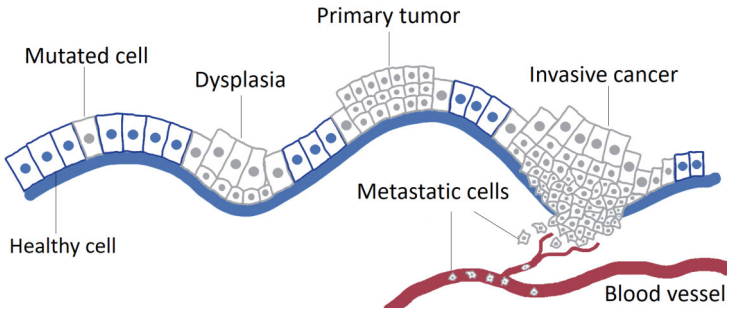

Figure 2.7: Cancer grading

Due to genetic mutations, many cell organelles undergo changes during the transformation from healthy to cancerous. In cytoplasm ribosomal and messenger ribonucleic acid (rRNA and mRNA) accumulate, some new structures develop and some normal structures disappear. For instance, secondary lysosomes appear but the golgi complex is usually less developed compared to healthy cells. Volume, shape, structure and density of the cell nucleus changes as well. The variability in shape and the decreased volume of mitochondria is connected with a changed metabolism of cancer cells. [22]

Changes in cytoskeleton can be observed as well. The amount of actin filaments in cancer cells is markedly reduced which leads to reduced cell elasticity in comparison to healthy cells [23]. The activity of actin filaments in cancer cells is increased leading to increased cell mobility. The microtubules are reorganized and form membrane protrusions which are important for cell mobility during metastases formation. Altered expression of tubulin isotypes and changes in the expression of microtubules-associated proteins are consequences of the transformation from healthy to cancerous cells [24]. Intermediate filaments play an important role in cell progression as well. Vimentin proteins regulate the detachment of the cells from the tumor, invasion into new tissue and the establishment at secondary site [25].

Through modifications of cell organelles, the cells themselves change. They have irregular sizes and shapes and are more deformable, i.e. their elasticity is changed. The cell cycle is accelerated, cell proliferation rate is higher and cell mobility is increased. The cell-cell communication is reduced and the cancer cells do not respond to signals of the surrounding tissue, i.e. cancer cells do not stop growing when they encroach surrounding tissue, but invade it. As a result of fast growth and division before the cells are mature, the cancer cells do not undergo maturation. The metabolism of cancer cells is modified as well. Unlike healthy cells which gain energy through oxidative phosphorylation in mitochondria, cancer cells generate most of their energy through lactic acid fermentation out of mitochondria. This is known as Warburg effect [26]. A further characteristic of cancer cells is that they do not repair cell damage or undergo apoptosis due to the inactivated tumor suppressor genes. Due to all characteristics of cancer cells, and especially invasiveness, cancer is one of the most challenging diseases nowadays.

2.2 Solid body deformation

The term solid body deformation is related to changes of the body's shape or size. This deformation can be the result of an external force applied or a temperature change. The focus of this thesis lies on deformations caused by external forces: tensile, compression, shear, bending or torsion deformation.

When an external force is applied to a solid body, it displaces solid body's atoms from equilibrium positions. The internal forces between the atoms oppose this external force to achieve a balance. If the external force is not too high, the internal forces can resist it and the body is in equilibrium state. When the external force is no longer applied, the atoms turn back to the equilibrium position. This kind of deformation is called reversible or elastic deformation as the solid body returns to its original shape after the application of force. If the external force is high enough that the internal forces cannot resist it, no balance between the forces will be reached and a permanent deformation occurs. This means, when the external force is no longer applied, the solid body's atoms do not return to their equilibrium position and the shape of the solid body is changed due to the external force. This kind of deformation is called irreversible or plastic deformation. Through further application of the external force it comes to the fracture of the material. A more detailed description of solid body deformation can be found in [27].

2.2.1 Elastic deformation

Elastic deformation is, as above already mentioned, a temporary deformation caused by an external force. When the external force is no longer applied, the solid body regains its shape. The elasticity of a solid body is its ability to resist this external force and return into its original size and shape when the force is no longer applied. It is described by two parameters, modulus and elastic limit. The first expresses the amount of force per area unit required for a certain amount of elastic deformation. Depending on the force's direction, three different moduli can be defined. Bulk modulus describes the reaction of a solid body to hydrostatic

force, applied equally from all directions. Shear modulus describes deformation by non-coaxial forces. Elastic or Young's modulus describes the behaviour of the solid body exposed to uni-axial stress in the direction of this stress. It corresponds to the slope of the stress(tension)-strain(amount of deformation) curve in the elastic deformation region. The higher the modulus, the harder it is to deform a material. The second parameter, elastic limit, expresses the maximal amount of force per area unit that can occur, before permanent deformation arises. On a stress-strain curve (see Figure 2.8), this is the transition point from elastic to plastic behaviour. [27]

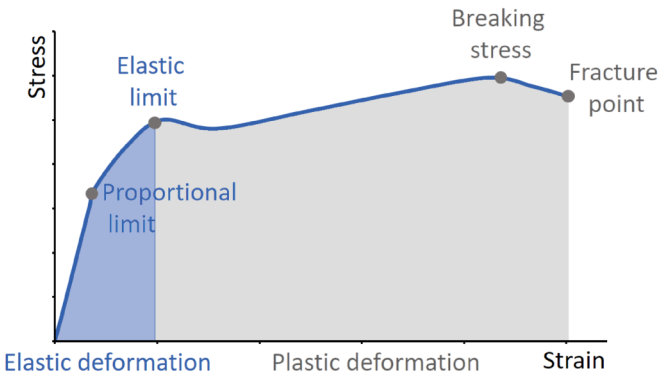

Figure 2.8: Stress-strain curve adapted to [28, page 170, Figure 2-66]

If a body's stress to strain ratio is constant for elastic deformation, it is considered linear-elastic. This behaviour appears usually by small deformations and can be described by Hook's law:

$$F = k \cdot \Delta l \tag{2.1}$$

where F is tensile force, k rate constant and Δl elongation. In terms of stress σ and strain ϵ, Hook's law can be expressed as:

$$\sigma = E \cdot \epsilon \tag{2.2}$$

with proportionality constant E, known as elastic modulus.

External forces can have other influences on linear elastic bodies as well. For instance, a short force impulse can set the body into periodic motion called vibration. This body will then oscillate around its equilibrium point with one or more natural frequencies, i.e. frequencies which the body tends to oscillate at without the influence of any external forces. During this kind of motion, the body can vibrate freely.

If the external force is periodic, the body undergoes forced vibration. In cases when an external force is periodically applied to the body without damping and the forced frequency matches the natural frequency the body experiences a phenomenon called resonance. According to this phenomenon, a small external periodic force enforces the body to oscillate with greater amplitudes for specific

frequencies, called resonance frequencies. The oscillating amplitude A is described as follows

$$A(t) = \sqrt{C_0^2 + (S_0 + t\frac{c_1}{2f_0})^2} \tag{2.3}$$

with constants C_0 and S_0 which can be determined from the initial conditions, t as oscillation time, c_1 as development coefficients and f_0 as natural frequency which is in this case equal to the resonance frequency. The oscillating amplitude is time-dependent and over the course of time the body will break.

If we observe forced vibration of a body with damping, the oscillating amplitude A depends on the frequency f:

$$A(f) = \frac{c_1}{\sqrt{4\gamma^2 f^2 + (f_0^2 - f^2)^2}} \tag{2.4}$$

For frequencies close to the resonance frequency, the amplitude can be intensified multiple times causing the solid body's destruction. This is known as resonance catastrophe with one of the most famous examples, Tacoma Narrows bridge. More details about Tacoma Narrows bridge catastrophe can be found in [29]. Figure 2.9 shows the amplitudes for resonance with damping and elongation for resonance without damping. [30]

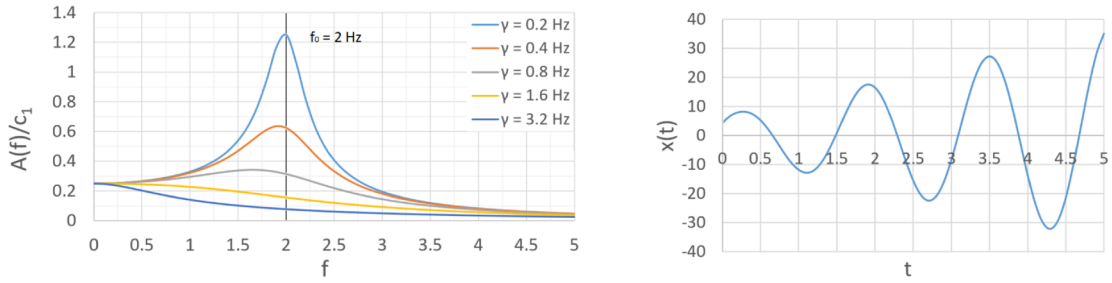

Figure 2.9: Oscillating amplitude for resonance with damping (left) and elongation for resonance without damping (right)

In materials science the resonance frequency is used to determine the elastic modulus of the material as the frequency depends on the material's geometry and elasticity. The American Society for Testing and Materials (ASTM) has specified standard test methods for the determination of the elastic modulus. The calculation equations depend on the shape of the observed material. For example, the elastic modulus of a rod with circular cross section can be calculated as follows:

$$E = 1.6067\frac{L^3}{D^4}mf^2T \tag{2.5}$$

where L is the length of the rod, D the diameter, m the mass, f the fundamental resonance frequency and T a correction factor. [31]

Even though individual cytoskeletal proteins have the shape of a rod, Equation 2.5 cannot be applied to the cytoskeleton network. As the cells are inhomogeneous, they react differently on the application of mechanical force. Furthermore,

the application of external force may cause new biological events in the cell, e.g. cytoskeleton rearrangement, which affect the elasticity of the cells. Due to the complexity of the cell structure and cytoskeleton network, more intricate models have to be developed. [32]

Nevertheless, the proportionality of elastic modulus and resonance frequency is valid regardless of the complexity of the system.

As a result of this proportionality, the resonance frequency of two materials with the same geometry, but a different elastic modulus, will differ as well as the reaction on the excitation frequencies. This is one of the fundamental premise for the development of a cancer cell selective treatment based on mechanical properties of the cells and their resonance frequencies.

2.2.2 Elasticity of cells

Cells are considered to be linear-elastic. In biophysical research, their elasticity is expressed through the elastic modulus. The methods used for cell elasticity determination can be divided into three main groups: optical, magnetic and mechanical methods.

One of the most commonly used optical method are optical tweezers. Beads are fixed to the cell and held in an optical trap. Using laser light, one of them can be moved and the reaction of the others can be measured. The diverse applications of this technique are described in [33]. Another known optical method for determination of a cell's elasticity is the use of optical stretchers [34].

Well known magnetic methods are magnetic twisting, attached magnetic beads and embedded magnetic beads. All of them are based on a similar principle. Magnetic beads are attached to the cells and when the cells are exposed to a magnetic field, the deformation of the cells can be observed and measured [35].

There is a wide range of mechanical methods used to determine cell elasticity. Some of them are micropipette aspiration, cell poking, microplates and tensile tester. The most commonly used one is atomic force microscopy (AFM). A cantilever with spherical or pyramidal tip slides over the cell. Using laser light, the cantilever deflection can be measured and the cell's topography can be derived. By performing force spectroscopy measurements, the elastic modulus of the cell can be determined. The cantilever is pressed onto the cell and the force required to impress the cell is measured. A data set called force distance curve, enables the determination of the cell's elastic modulus. As the elasticity at the edge of the cell differs from the elasticity above the cell nucleus, the mapping of a whole cell is recommended. [36]

Detailed research has shown that the elasticity of cells is mainly determined by the cytoskeleton [37, 38]. Furthermore, Haga et al. [39] showed that intermediate and actin filaments contribute to the cell elasticity more than microtubules. Nevertheless, not only cytoskeleton, but also the cell nucleus, influences the elasticity of the cell [40, 41]. Therefore, the elastic modulus measured over the nucleus is higher than the elasticity of the cell periphery.

The elasticity of the cells is also affected by the environment. The stiffness of the surrounding tissue in vivo or the substrate in vitro influences the elasticity of the cells [42]. Sunyer et al. showed that temperature changes cause changes in

elasticity as well [43].

Investigating the differences between cancer and healthy cells, various authors showed that the elastic modulus of cancer cells is reduced compared to healthy cells [3, 4, 5]. One of the reasons are changes in the cytoskeleton due to the transformation from healthy to cancer cells (see Chapter 2.1.4). If the elastic modulus of cancer cells is lower, due to the proportionality of elastic modulus and resonance frequency, latter has to be lower as well. Fraldi et al. [32] suggest different models implementing physical principles on a simplified cell structure, based on different connections of viscous and elastic elements. Moreover, using purposed models and elasticities of the cells know from literature, they have determined the resonance frequencies of healthy and cancer cells. The results show substantial differences in the resonance frequencies between cancer and healthy cells.

Using differences in the resonance frequency, a resonance catastrophe could be induced to selectively destroy cancer cells. As for the healthy cells of the surrounding tissue the resonance frequencies should be higher, exposure to resonance frequencies of cancer cells should not harm them. In this way a super-selective ablation therapy could be developed to destroy cancer cells and spare surrounding tissue.

2.3 Fluorescence microscopy

With a wide range of applications, fluorescence microscopy became one of the most commonly used imaging techniques in biology and biophysics. It enables highlighting of different specimens, from cell organelles to single molecules. Using fluorescent labels or fluorochromes, specimens which do not fluoresce naturally can be imaged using this technique as well.

2.3.1 Fluorescence

Fluorescence is, along with phosphorescence, a type of luminescence, i.e. spontaneous emission of radiation by the specimen in an excited state. More precisely, fluorescence and phosphorescence are types of photo-luminescence, which is a result of photon absorption. Both processes, resulting in photon emissions, are illustrated in the Perrin-Jablonski diagram shown in Figure 2.10.

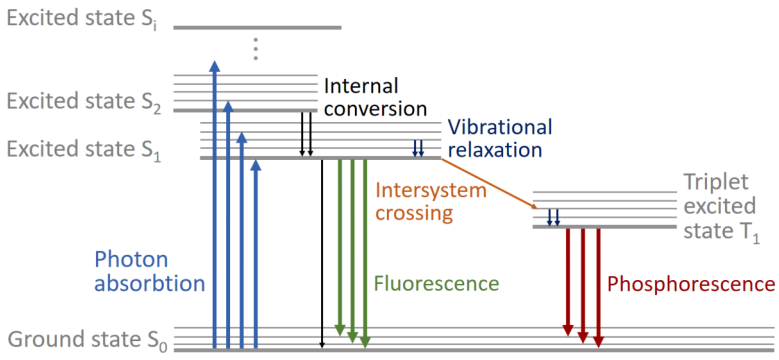

Figure 2.10: Perrin-Jablonski diagram

At equilibrium, electrons of an atom or molecule are at the ground state S_0, which is energetically most favourable for the electrons. If the fluorochrome is exposed to electromagnetic radiation, its orbital electron may absorb a photon of light and it is excited to an energetically higher electronic state S_i. To each of those electronic states belong several vibrational states. The energy of the absorbed photon $h\nu$ (where h is the Planck constant and ν the frequency of the photon) must be equal to the difference between two discrete energy levels. The higher energetic state is energetically unfavourable and the electron tends to return to the energetically favourable state. Through vibrational relaxation, the electron can release its energy in form of, e.g., heat and return to the lowest vibrational state S_1. This process is called internal conversion and occurs within about 10^{-12} s. Electrons in the S_1 state can undergo non-radiative processes like internal conversion or radiative processes with photon emission like fluorescence or phosphorescence.

In the case of fluorescence, the electron spontaneously emits a photon and deexcites to the ground state S_0. This process takes about 10^{-8} s. Its efficiency is defined as quantum yield, i.e. the ratio of emitted to absorbed photons.

An electron in excited state S_1 can, instead of fluorescence or internal conversion, undergo spin conversion to the first triplet state T_1 called intersystem crossing. The transition from T_1 to a singlet ground state S_0 is an electric dipole transition and as such forbidden. As electric quadrupole transition is allowed, the transition from T_1 to S_0 occurs with the emission of a photon. This transition is termed phosphorescence and it can take from a few seconds to hours. A detailed explanation of forbidden transitions can be found in [44]. Fluorescence and phosphorescence are covered in the work of Aleksander Jablonski [45] or [46, 47].

Observing the Perrin-Jablonski diagram, one can notice that the emitted photon can maximally have the energy of the absorbed one.

$$E_e \leq E_a \tag{2.6}$$

During non-radiative processes an electron in an excited state releases its energy in form of, e.g., heat. Due to that and also general considerations regarding the conservation of energy, the emitted photon must have a lower energy than the absorbed one. The energy of an emitted and absorbed photon can be expressed using their wavelengths:

$$\frac{hc}{\lambda_e} < \frac{hc}{\lambda_a} \tag{2.7}$$

As it can be seen, the lower energy of an emitted photon is displayed through its longer wavelength:

$$\lambda_e > \lambda_a \tag{2.8}$$

The differences in wavelengths were described by Sir George Gabriel Stokes in [48]. The shift of the emission photon's wavelengths to the red part of the spectrum is also known as Stokes' shift, shown in Figure 2.11.

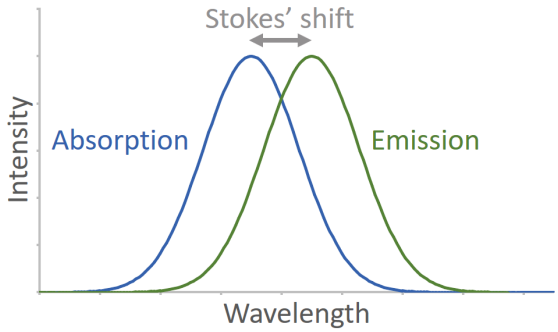

Figure 2.11: Stokes' shift

2.3.2 Confocal Laser Scanning Microscopy

Confocal laser scanning microscopy (CLSM) is a well known microscopy technique by which out-of-focus light can be blocked resulting in high resolution and high contrast images. This is realized through the confocal principle introduced by Marvin Minsky [49]. Contrary to standard optical microscopes where the whole specimen is equally illuminated, in confocal microscopy only one spot of a specimen is illuminated at a time. The confocal principle is achieved using pinholes.

The light path through a simple fluorescence confocal microscope goes as follows. Different light sources like xenon or mercury lamps, light-emitting diodes (LEDs) or laser beams can be used. They emit light which passes through an excitation filter which is set up to filter all of the wavelengths, except the one chosen for the excitation of the specimen. In the case of CLSM a laser beam of a specific wavelength is used and does not have to be filtered. The light emitted from the laser passes through a first pinhole, also called excitation or source pinhole to the dichroic mirror. This mirror is specially coated, so that specific wavelengths are reflected and the other ones pass through. The excitation light reflects on this mirror and passes through the objective to the specimen. In the specimen, fluorescent molecules get excited and by relaxation emit light of a longer wavelength due to Stokes' shift. It should be noted that specimen's molecules out of the focal plane get excited and emit light as well. The emission light passes through the objective and the dichroic mirror coated in a way that it allows the emission light through, due to its longer wavelength. A second pinhole, the detection pinhole, is placed in the specimen's image plane so that the emission light from the focal plane can pass through. In this way most of the emission light from the planes above and below the focal plane is blocked. Herewith a higher lateral and axial resolution can be achieved, compared to standard optical microscopy. In the end of the light path the emission light is detected usually by a photomultiplier (PMT) or charge coupled device cameras (CCD). The setup of a confocal fluorescence microscope is illustrated in Figure 2.12. [50]

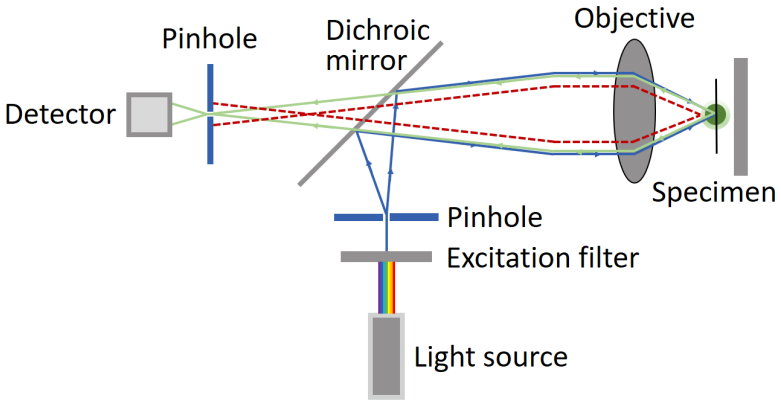

Figure 2.12: Illustration of the light path through a confocal fluorescence microscope

As the confocal principle entails one point at a time imaging, the whole specimen area has to be scanned point-to-point to obtain the whole image of the specimen in two dimensions. Therefore three different techniques were developed: sample, objective and beam scanning. Most of modern microscopes use the beam scanning technique which can be implemented in several ways, such as replacing the pinhole with an optical fiber or a Nipkow disc or using an acousto-optic cell. The most commonly used scanning solution is the use of a pair of galvanometer mirrors which move the beam in x-y direction. Those are positioned between dichroic mirror and objective and allow scanning without changing the confocal setup or moving the specimen. [51]

One of the solutions to collect three-dimensional images, which is often integrated into modern microscopes and corresponding software, is to select the focus plane at the top/bottom of the specimen and scan through the whole z dimension of the specimen. The step size between the images can usually be determined by the user.

2.3.3 Fluorochromes

To do fluorescence microscopy of a specimen which does not undergo fluorescence naturally, specifically designed fluorescent labels or fluorochromes must be used. Those are compounds of fluorophores and molecules able to target the structures to be observed. The fluorophores are able to fluoresce upon the light excitation what makes them suitable for fluorescence microscopy. They are characterized through optical properties like excitation spectrum, emission spectrum, excitation coefficient, quantum yield and lifetime.

The **excitation spectrum** defines which part of electromagnetic radiation can induce fluorescence of a fluorophore and the **emission spectrum** defines the spectrum of electromagnetic radiation in which this fluorophore emits the radiation upon fluorescence. A larger gap between excitation and emission spectrum, due to Stokes' shift, is beneficial for better detection of emitted light. The **excitation coefficient** is a measure of the amount of absorbed light for a specific wavelength. **Quantum yield** is the ratio of emitted to absorbed photons. Its value

is 1 when each absorbed photon induces the emission of one photon. Nonetheless, substances with a quantum yield of 0.1 are already considered to be good fluorescent substances. The **lifetime** of a fluorophore is defined as the time from the excitation of the fluorophore until the emission of radiation. It is independent of the fluorophore concentration, sample thickness or excitation intensity.

Fluorochromes or fluorescence labels, the combination of fluorophore and targeting molecule, must meet several conditions, depending on what they are intended for. For live cell imaging the fluorochrome has to be permeative to pass through the cell membrane and bind to the organelle of interest. It should not be toxic for the cells or influence their biological activity or mechanics. The targeting has to be specific, so that just the organelle of interest is highlighted and marked completely. Different types of fluorochromes fulfil those conditions and can be distinguished by the fluorophore or targeting molecule. Different proteins, lipids, polysaccharides, as well as nanoparticles or quantum dots can be used for fluorescence labeling. Further information on fluorochromes, their structure and characteristics as well as application can be found in [52, 53, 54].

2.3.4 Fluorescence microscopy problems

Fluorescence microscopy is one of the most used techniques in cell biology. In combination with the confocal principle it enables high resolution imaging of single cell organelles, morphology analysis, investigation of cellular processes as well as cell dynamics. Despite all benefits of fluorescence microscopy, some problems during live cell imaging can arise. Those can be divided into two categories: one influencing the image quality like photobleaching, quenching, cross-talk or bleed-through and one influencing the cells like phototoxicity.

Photobleaching is an effect caused by photo-induced cleavage of covalent bonds leading to a permanent loss of the fluorophores ability to fluoresce. The fluorophores can undergo a defined number of excitation-emission cycles, before covalent bonds cleave due to single to triplet state transitions. When the maximal number of cycles is reached and the bonds cleaved, the fluorophore cannot fluoresce anymore. During imaging more and more fluorophores are losing their ability to fluoresce and the image is getting darker and darker. The photobleaching effect can be reduced by applying lower laser intensities, reducing the imaging time or using more stable fluorochromes. [55, 56]

The **quenching** effect leads to a reduction of the fluorescence intensity as well. This effect may occur due to molecular rearrangements, energy transfer, ground-state complex formation or molecular collisions. When the fluorophore in excited state collides with a non-fluorescing atom or molecule (quencher), dynamic quenching can occur. The quencher absorbs an amount of the fluorophore's energy. Due to this energy loss, the fluorophore does not emit a photon by relaxation to the ground state. If the quencher-fluorophore collision creates a new compound, static quenching occurs and the new compound usually does not fluoresce. The quenching effect usually occurs when the fluorochrome concentration is too high as the probability of collisions rises. By determining a suitable staining concentration and staining time, this effect can be prevented. [46, 57]

During simultaneous cell staining, using two or more fluorochromes, it can come

to two similar effects, **cross-talk** and **bleed-through**. As a result of those effects the fluorescence signals cannot be clearly separated in the images. Cross-talk occurs by a spectrum overlap or insufficient separation of the excitation wavelengths. Unlike cross-talk, bleed-through occurs when the emission wavelengths overlap and the detector cannot distinguish between them [58].

Phototoxicity is one of the effects induced by high laser intensity. When the fluorochrome is in excited state it can react with the molecules from the environment. During this reaction a transfer of an electron or a hydrogen atom from or to this molecules can arise. Those molecules become toxic radicals which can damage the cell. A second type of phototoxicity happens when the fluorochrome in excited state transfers from singlet to triplet state and reacts with molecular oxygen. This reaction forms singlet excited oxygen which is also toxic and can lead to cell damage or even cell death. Reduction of laser intensity can minimize this effect. [59]

In addition to the above described effects, excessive laser intensity can cause other problems as well. For instance, by increasing laser intensity over a critical level, the intensity of the focal plane will not increase, but the one from the planes above or below. In this case, some organelles appear to be bigger than they are. If fluorescence confocal microscopy is used for 3D imaging and volume calculation, results gained in this way are inaccurate.

A big challenge of time-lapse microscopy in general is **focal drift**. This is described as inability of a system to preserve the focal plane preselected by the user. External influences like environmental temperature changes, vibrations of the system, laser intensity, sample heaters or addition of reagents can lead to focal drift. Reduction of this effect can be accomplished by keeping the environmental temperature constant, using anti-vibrational tables or collecting image stacks periodically and do a software analysis as described in [60].

Careful selection of suitable staining concentration and staining time for the observed specimen, decreasing laser intensity and external temperature changes or vibrations can largely reduce the described problems. Nevertheless, they can always arise during live cell imaging. When the measurements are planned individually and possible issues are taken into consideration, the measurements are well comparable and reproducible.

2.4 Sound

Sound or acoustic waves are longitudinal waves that propagate in a medium like gases, liquids or solids by compression and decompression. If those waves exhibit frequencies between 20 Hz and 20 000 Hz they can be perceived by humans as sound. Waves with frequencies higher than 20 000 Hz cannot be perceived by humans and are called ultrasound.

2.4.1 Acoustic waves

Acoustic waves in liquids and gases propagate as longitudinal waves and in solids as both longitudinal and transversal waves. Longitudinal waves are the waves

in which the particles of the medium oscillate about the mean position in the direction of wave propagation. Transversal waves are waves in which particles of the medium oscillate about the mean position perpendicularly to the wave propagation direction. [61]

As acoustic waves are periodical waves they can be described with the following parameters: amplitude, wavelength, period, frequency and velocity as well as acoustic pressure and acoustic intensity. A deviation of the particle from the equilibrium position is called particle displacement, the greatest deviation is also known as the amplitude. The smallest distance between two particles which are oscillating in the same phase is called wavelength. The time interval in which the particle completes one oscillation cycle is called time period. These described dimensions can be seen in Figure 2.13.

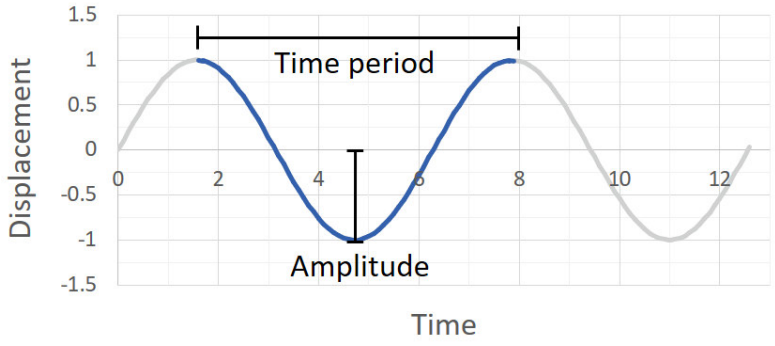

Figure 2.13: Dimensions describing waves: amplitude and time period

The frequency expresses the number of oscillations in one second. It is equal to the reciprocal value of the time period. Wave velocity is the distance that the wave travelled in the time period of one second. Acoustic pressure is the deviation of the local pressure from atmospheric pressure caused by acoustic waves. Acoustic intensity is defined as the average rate of the acoustic energy flow through an area unit normal to the wave propagation direction. It can be expressed as:

$$I = \frac{1}{2} A^2 \omega^2 \rho v \tag{2.9}$$

where A is the wave amplitude, $\frac{\omega}{2\pi}$ the frequency, ρ the medium density and v the velocity. [61] The acoustic intensity is influenced by factors like oscillation amplitude and surrounding area and, for spherical waves, decreases with the square of the distance from the source.

The propagation of acoustic waves in gasses or liquids can be described with following wave equations:

$$\Delta p - \frac{1}{c_0^2} \frac{\partial^2 p}{\partial^2 t} = 0 \qquad \Delta v - \frac{1}{c_0^2} \frac{\partial^2 v}{\partial^2 t} = 0 \tag{2.10}$$

where p is the aforementioned acoustic pressure, t the time and v the particle velocity. The sound velocity c_0 is defined as:

$$c_0 = \frac{1}{\sqrt{\rho_0 \kappa_0}} \tag{2.11}$$

with ρ_0 as density and κ_0 as compressibility. [62]

Liquids and gasses possess volume elasticity. Unlike fluids, solids possess volume and shear elasticity making the description of wave propagation in solids much more complicated. Instead of pressure, the concept of force related to a surface unit is introduced. The wave equation for the propagation in solids is based on Newton's second law for elementary volume. It describes the propagation of acoustic waves along the x axis as follows:

$$\rho\frac{\partial^2 u_x}{\partial t^2} - (\Lambda + \mu)\frac{\partial_\epsilon}{\partial_x} - \mu\nabla^2 u_x \tag{2.12}$$

where Λ and μ are Lame constants and ∇^2 the Laplace operator. A more detailed explanation of acoustic wave propagation in solids can be found in [63].

2.4.2 Generation of acoustic waves

Acoustic waves can be generated in many different ways. For medical purposes, their parameters like wavelength, amplitude, frequency, intensity and pressure must be well defined. The generation of this kind of acoustic waves is possible using piezoelectric actuators. They convert electric quantities into mechanical ones. This can be expressed as:

$$E = \frac{1}{d}S \tag{2.13}$$

where the applied electric field E results in mechanical strain S with the piezoelectric coefficient d. [62]

The working principle of piezoelectric actuators is based on the piezoelectric effect. There are two types of piezoelectric effects: direct and inverse. The piezoelectric effect can be explained on piezoelectric crystals. Their elementary cells possess an electric dipole moment. Without external influences the centers of charges coincide and the crystal is electrically neutral. When an external mechanical force is applied to the crystal, the charges relocate and a voltage can be measured. This is called direct piezoelectric effect.

The inverse piezoelectric effect considers the application of an external electric field to induce a deformation of the crystal. The external electric field induces an additional dipole moment in the opposite direction. Since the system tends to be at equilibrium state, the crystal is spreading or shrinking to balance the additional dipole moment, which results in mechanical deformation. The latter effect can be used in piezoelectric actuators to generate acoustic waves. If piezoelectric actuators can undergo both effects, they are called piezoelectric transducers. Figure 2.14 shows both piezoelectric effects. [64]

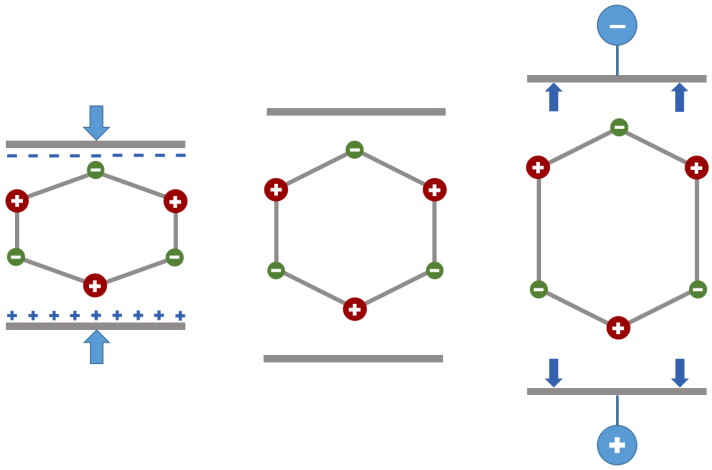

Figure 2.14: A crystal undergoes the direct piezoelectric effect (left), crystal in equilibrium (middle) and crystal undergoes the inverse piezoelectric effect (right)

There are different types of piezoelectric actuators, depending on the type of generated displacement. Contracting actuators are usually made of two piezo elements acting simultaneously to produce contracting motion usually in one direction. Even though they have a small displacement, they can generate high forces. Tube actuators have a radial polarization and can be displaced in axial, radial or lateral direction depending on the way of voltage application. Shear actuators consist of multiple layers of piezo elements polarized horizontally. Displacement in the horizontal plane creates shear motion. Longitudinal actuators are, as well as shear actuators, multi-layers of piezo elements. Those elements are stacked on top of each other. By combining the displacement of each element they can generate a high linear displacement. [65]

More about the piezoelectric effect, its usage and piezoelectric actuators can be found in [64].

2.4.3 Sonication of cells

Sonication of cells is a well known technique in medical diagnostics and therapy. Acoustic waves of high frequencies enable medical diagnostics based on ultrasound imaging. This technique is less complex and harmful compared to computed topography (CT) or magnetic resonance imaging (MRI).

Sonication using ultrasonic waves can produce well known side effects due to acoustic cavitation. Ultrasonic waves of great amplitudes generate high velocities which can, according to Bernoulli's principle, cause a decrease of local pressure. If the amplitudes are high enough to bring the local pressure below the saturated vapour pressure, vapour bubbles form. When the deflection of the ultrasonic wave reaches the turning point, the velocity is equal zero what increases the local pressure which is then higher than vapour pressure. This leads to the collapse of the vapour bubbles. Herewith a high amount of energy is released, resulting in a temperature increase and causing shock waves. This effect is used in medicine for kidney stones removal or prostate cancer therapy. Due to the locally uncontrolled spread of the heat, the surrounding tissue is also affected by this type of cancer

therapy. [66, 67, 68]

Acoustic waves may be used for one more type of cancer therapy, selective ablation of cancer cells. This kind of therapy would be based on mechanical resonance and not cavitation which would reduce effects on the surrounding tissue. If the cancer cells are irradiated with acoustic waves which force the cancer cells to oscillate with their resonance frequencies, a resonance catastrophe could be induced. The cells could directly burst or the apoptosis could be triggered. As the resonance frequency of healthy cells differs, those cells should not be affected. [32, 69]

3. Materials and methods

The topic of this thesis is to investigate the irradiation of cancer cells with acoustic waves. Ranging from 0.5 to 10.0 kHz, these waves may lead to cancer cell destruction by a resonance catastrophe. So far, this development process of a new cancer therapy comprises of three main parts. As all experiments were made using fluorescence microscopy, the first part deals with the determination of suitable staining parameters for the fluorochromes and cell lines used. In the second part, the morphology of the used cell lines and their organelles like microtubules, actin filaments and mitochondria was determined to characterize the cell lines and investigate the differences between cancer and healthy cells. The third part deals with the acoustic wave irradiation of the cells. This chapter elucidates the materials and methods used during this thesis.

3.1 Cell lines and cell culture

Four cancer cell lines of the head and neck area (UD-SCC) as well as dysplastic oral keratinocytes (DOK) and human oral keratinocytes (HOK) were used. All cancer cell lines were established in the research laboratory of the Department of Otorhinolaryngology of the Düsseldorf University Hospital from primary tumors of four different patients. The procedure of cell line establishing is explained by Ballo [70]. DOK and HOK are commercially available cell lines used as examples for dysplastic and healthy cells. The following subsections describe the used cell lines and their cultivation.

3.1.1 Cell lines

The observed cancer cell lines are head and neck squamous cell carcinoma cell lines originating from different areas. They are classified according to TNM classification, where T provides details on the size of the primary tumor, N describes involved regional lymph nodes and M gives information whether distant metastases have been found.

Cell line **UD-SCC-01** originates from a primary tonsil cancer classified by TNM classification as tumor larger than 5 cm (T3), with infection of a lymph node at the internal thoracic artery (N2b) and without distant metastases (M0).

The **UD-SCC-02** cell line is originating from a hypopharynx cancer. The primary tumor is classified as smaller than 2 cm (T1), infecting the lymph nodes (N2) but without distant metastases (M0).

The two cancer cell lines UD-SCC-04 and UD-SCC-06 both originate from tongue cancer. The primary tumor of cell line **UD-SCC-04** is classified as larger than 5 cm (T3) with infestation of an axillary lymph node, displaced (N1). Distant metastases were not found (M0). The primary tumor of cell line **UD-SCC-06** is between 2 cm and 5 cm big (T2), without lymph node infection (N0) or distant metastases (M0). Patient and primary tumor details are given in Table 3.1.

Cell line	Sample origin	Lesion type	TNM classification	Patient age
UD-SCC-01	Tonsil	Primary	T3N2bM0	64 years
UD-SCC-02	Hypopharynx	Primary	T1N2M0	58 years
UD-SCC-04	Tongue	Primary	T3N1M0	47 years
UD-SCC-06	Tongue	Primary	T2N0M0	64 years

Table 3.1: Tumor and patient details of the four cancer cell lines

Co-cultivation – simultaneous cultivation of two cell lines in the same Petri dish – enables observing the reaction of two cell lines on the acoustic wave irradiation at the same time. To distinguish two different co-cultivated cell lines during simultaneous observation, cancer cell line UD-SCC-01 was infected using viral vectors to express the blue fluorescence protein (BFP). When the cell line UD-SCC-01 with BFP was co-cultivated with, for example, the DOK cell line, using a fluorescence microscope, cells of both cell lines could be distinguished due to an additional blue fluorescence signal of the cells expressing BFP. The infection of the cell line UD-SCC-01 was done by the personnel of the research laboratory of the Department of Otorhinolaryngology.

Cell lines DOK and HOK were used for the comparison of cancer cell lines' properties with the properties of dysplastic and healthy cells. The **DOK** cell line is a commercially available dysplastic oral keratinocytes cell line. According to the data sheet [71] this cell line was established from the remaining dysplasia of a 57 year old patient after a dorsal tongue tumor had been removed. The dysplasia degree was mild to moderate and the cells are non-tumorogenic in athymic nude mice.

Oral keratinocytes cell line **HOK** is, as well as DOK, commercially available [72]. The cells are isolated from human oral mucosa and cryopreserved at passage one. They were additionally immortalized in the research laboratory of the Department of Otorhinolaryngology to achieve a higher proliferation rate.

3.1.2 Cell culture

All the cell lines were cultivated by the author in the research laboratory of the Department of Otorhinolaryngology. The cultivation process of cancer and DOK cell lines differs to the one of HOK due to the cells' sensitivity. Both processes will be explained hereinafter.

Cultivation of cancer and DOK cells

The cancer and DOK cell lines were cultivated in 10 cm diameter Petri dishes without additional coating. To cultivate cancer cell lines, Dulbecco's modified Eagle's

medium with additional 4.5 mM glucose and 2 mM GlutaMAX supplemented with 10 % fetal bovine serum (FBS), 100 $\frac{U}{ml}$ penicillin and 100 $\frac{\mu g}{ml}$ streptomycin (later in text DMEM medium) was used. For the cultivation of DOK cells, DMEM medium contained additional 0.5 % of hydrocortisone to stimulate the cell growth.

In the first step DMEM medium was aspirated out of the dish containing cells. The cells were washed using 5 ml of Phosphate-Buffered Saline (PBS), i.e. PBS was given into a dish with the cells, the dish was carefully swivelled and the PBS was aspirated. Afterwards, 2 ml of Trypsin/EDTA Solution (later in text Trypsin) was given to the cells. Trypsin is a solution used in cell culture to detach adherent cells from the surface which they grow on. The cells were incubated at 37°C in an incubator containing humidified air with 5 % CO_2. After several minutes, the cells detached from the surface and could be cultivated in a new dish.

8 ml of DMEM medium was given to the detached cells to stop the reaction of the Trypsin. The wished concentration of cells was pipetted into a new Petri dish containing 10 ml of a medium suitable for the cultivated cell line. The cells were then incubated for several days until the Petri dish bottom was about 90 % covered with cells. Those cells were then cultivated again or prepared for the measurement.

Cultivation of HOK cells

The HOK cell line was cultivated in 10 cm diameter Petri dishes coated with 5 ml of 0.1 % gelatine in oral keratinocyte medium (OKM) containing 500 ml of basal medium, 5 ml of oral keratinocyte growth supplement and 5 ml of penicillin/streptomycin solution [73].

The first steps of HOK cell line cultivation were the same as described above. The medium which the cells grew in was aspirated, cells were washed and Trypsin was given to the cells to detach from the surface. After detaching of the cells, 5 ml of OKM medium was given to the cells and they were centrifuged for 5 minutes. In this way the cells could be separated from the mixture of medium and Trypsin. As the HOK cells are sensitive to Trypsin, this mixture was aspirated and fresh 10 ml of OKM medium was given to the cells. The desired concentration of cells was then given into a new, coated Petri dish containing 10 ml of OKM medium.

For the fluorescence microscopy investigations all cells were cultivated in 35 mm diameter dishes with inserted glass bottom of 18 mm diameter, coated with 2 ml of 0.1 % gelatine in for each cell line suitable medium. All cancer and DOK cell lines were plated one day before observation under the microscope. Due to slower cell growth, HOK cells were plated three days before microscopy investigation.

3.2 Cell preparation for live cell imaging

Fluorescence microscopy enables observation of single organelles on *living* cells. Nevertheless, this is a challenging task as the method of observation should not influence the cells, their morphology or dynamics. For this reason the used fluorochromes and fluorescence labels have to be chosen carefully. Suitable staining parameters like staining time and concentration should be determined for each

specimen of interest to minimize side effects. This section describes the used fluorochromes, cell staining and preparation for imaging.

3.2.1 Used fluorochromes

For fluorescence microscopy cell organelles of the observed cell lines had to be highlighted with different fluorochromes. As live cell imaging was performed, those had to be chosen carefully to minimize their influence on the cells. Five different organelles were investigated during this thesis: cell membrane, microtubules, actin filaments, cell nuclei and mitochondria. Suitable fluorochromes have been chosen and will be described below.

Cell membrane staining was made using **CellMask^{TM} Green plasma membrane stain (C37608)**, further in text CellMask Green. The molecules of CellMask Green are both hydrophilic and lipophilic. The hydrophilic units are able to anchor in the cell membrane and the lipophilic enable good membrane loading. The excitation maximum of CellMask Green is at 522 nm and the emission maximum at 535 nm. During this thesis, the filter set Enhanced Yellow Fluorescent Protein (EYFP) with a spectrum between 530 nm and 570 nm was used for live cell imaging of cells stained with CellMask Green. Further information and the staining protocol suggested by the manufacturer can be found in [74].

Cytoskeleton proteins microtubules and actin filaments were stained using Cytoskeleton Kit (CY-SC006) containing two fluorescence labels, SiR-tubulin and SiR-actin.

Fluorochrome **SiR-tubulin** is a compound of the fluorophore silicon rhodamine and Docetaxel, a drug binding on microtubules. Even though SiR-tubulin is made for live cell imaging, in high concentration during time-lapse imaging it can influence the dynamics of the microtubules by prolonging the mitotic duration and reducing cell proliferation [75]. Its excitation maximum is at 652 nm and emission maximum at 674 nm. During this thesis, the filter set Cy5 with a spectrum between 661 nm and 761 nm was used.

To stain actin filaments, fluorescence label **SiR-actin** was used. It is based, like SiR-tubulin, on silicone rhodamine fluorophores. For actin filaments targeting, the natural actin binding product jasplakinolide [76] was used. During time-laps imaging, in a high concentration, SiR-actin can interfere with the dynamics of the actin filaments and reduce cell proliferation. As SiR-actin and SiR-tubulin have the same excitation and emission maxima, the same filter setup was used. This has been shown as disadvantage because simultaneous staining and imaging of microtubules and actin filaments is not possible. The spectra overlap and crosstalk and bleed-through effects occur, which means that actin filaments are shown in the channel of microtubules and vice versa. More details about both cytoskeleton labels can be found in [75].

Cell nuclei of the observed cell lines were stained using **Hoechst 33342**, fluorochrome based on trihydrochloride. It binds to all nucleic acids, but when binding with double-stranded DNA it enhances fluorescence. Hoechst 33342 is suitable for cell nucleus visualization, automated DNA determination, determination of cell number, chromosome sorting or nuclear damage detection [77]. The excitation maximum of Hoechst 33342 is at 350 nm and emission at 461 nm, thus, the DAPI

filter set with a spectrum from 425 nm to 475 nm was used.

MitoTracker® Orange CMTMRos is a rosamine-based fluorochrome containing a mildly thiol-reactive chloromethyl moiety [78], used to highlight active mitochondria. It is able to passively diffuse into the cell and accumulate in active mitochondria. MitoTracker Orange has its excitation maximum at 554 nm and emission maximum at 576 nm. During this thesis the filter set MitoTracker with a spectrum defined between 570 nm and 670 nm was used.

The stock solutions of all used fluorochromes were prepared in the same way. The content of the fluorochrome vial was diluted in dimethyl sulfoxide (DMSO) to get a staining kit concentration of 1 mM. Those stock solutions were used for cell staining as described in the following subsection.

3.2.2 Cell staining procedure

Cell staining using the aforementioned fluorochromes is a standardized procedure and it can be applied to all cell lines and fluorochromes used. The parameters which have to be adapted to every fluorochrome and cell line are the concentration of the fluorochrome and the duration of staining (staining time). In order to avoid a contamination of the cells, cell staining must be made under the cell culture hood. The person working with the cells must wear gloves and all the equipment like microtubes, pipettes or aspiration pump's tips must be sterilized.

In general, the staining procedure was carried out as follows: in the first step the staining solution was prepared. In the beginning it was calculated how much of the stock solution of fluorochrome must be diluted in 1 ml PBS to gain the staining concentration of interest. The staining solution was mixed in a microtube in the way that the calculated amount of fluorochrome's stock solution was given to 1 ml of PBS.

In the second step, the medium which cells grew in was aspirated from the cells and the staining solution was added. The cells were then incubated for the desired staining time. After the staining time elapsed, the staining solution was aspirated and the cells were washed using 1 ml PBS. Through this procedure the rest of the staining solution, deceased cells and cell debris could be aspirated. In the end, 1 ml of FluoroBrite DMEM medium was given to the cells. This medium is based on DMEM medium thereby containing all required nutrients for the cells and additionally containing substances for the reduction of background fluorescence, i.e. enhancing the signal-to-noise ratio.

For some measurements the cells were stained with two fluorochromes simultaneously. If the staining time of both fluorochromes was equal, the stock solution of both fluorochromes was diluted in 1 ml PBS and given to the cells accordingly to the described protocol. If the staining times of two fluorochromes differ, the staining solution with the stock solution of the fluorochrome requiring more time was prepared and given to the cells. The cells were then incubated for the time difference between the staining times of the two fluorochromes. When that time elapsed, the stock solution of the second, less time requiring, fluorochrome was given to the cells and, using a pipette, the stock solution and staining solution were mixed. The cells were then incubated for the rest of the staining time. When this time elapsed, the cells were washed with PBS and FluoroBrite DMEM medium

was given to the cells. To avoid staining time inaccuracy, the staining time had to be measured precisely and the addition of the second staining solution had to be planned carefully and made quickly, to not induce other influences on the cells.

3.3 Live cell imaging

The development of microscope technology opened a wide spectrum of research possibilities. Nowadays, live cell imaging is a standard method in biology and biophysics. 3D imaging of cells and their organelles enables better characterization of cells and better comparison of different cell lines. Time-lapse microscopy allows the observation of the cell's behaviour, mechanics and their reaction on externally caused changes. As an output, a great amount of data is produced which has to be analysed with suitable software. The microscope used, as well as the imaging procedure and data analysis software will be explained in the following.

3.3.1 Olympus Fluoview 1000

The fluorescence microscopy measurements performed during this thesis were made using the inverse confocal laser scanning microscope system Olympus Fluoview 1000. This microscope was provided by the Center of Advanced Imaging and is located at the Institute for Molecular Physical Chemistry, both at Heinrich-Heine-University Düsseldorf. The work station and the microscope can be seen in Figure 3.1.

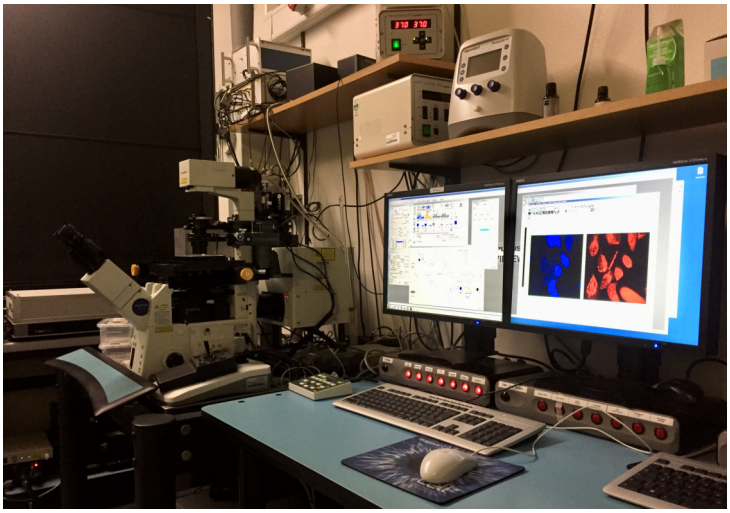

Figure 3.1: Work station Olympus Fluoview 1000

The Olympus Fluoview 1000 is equipped with diode lasers with wavelengths of 405 nm, 559 nm and 635 nm as well as a multi-line Argon gas laser with 458 nm, 488 nm and 515 nm wavelengths. The simultaneous scanning unit enables imaging with up to three different laser wavelengths (three fluorochromes) at the same time. The detection of the fluorescence signal is achieved through a high sensitivity photomultiplier tube. In addition to the fluorescence illumination, the Olympus Fluoview 1000 is equipped with a conventional illumination system.

The used microscope is an inverse microscope which means that the objectives and the laser light are placed below the specimen. Nevertheless, the conventional illumination, achieved through a halogen lamp, is placed above the specimen. The conventional illumination equipment can be easily detached from the microscope in order to install other equipment, e.g. a piezoelectric actuator.

The available objectives exhibit a magnification of 10, 20, 40 and 60 times. Two objectives with 60 times magnification are available, one with water as immersion medium and one with oil. The technical data about the available objectives are given in Table 3.2. Further details about the Olympus Fluoview 1000 can be found in [79].

Objective	Magnification	Numerical aperture	Working distance (mm)	Slide thickness (mm)	Immersion medium
UPLSAPO10X2	10 times	0.40	3.10	0.17	Air
UPLSAPO20X	20 times	0.75	0.60	0.17	Air
UPLSAPO40X2	40 times	0.95	0.18	0.11-0.23	Air
UPLSAPO60XO	60 times	1.35	0.15	0.17	Oil
UPLSAPO60XW	60 times	1.20	0.28	0.13-0.21	Water

Table 3.2: Technical data of the objectives [79]

To better understand Table 3.2, some dimensions will be explained. The **numerical aperture** of the objective is a measure of the ability to gather light and to resolve details at a fixed object distance. The higher the numerical aperture, the higher the amount of light collected, which enables a clearer image and more details can be distinguished from another. Increase of the numerical aperture can be achieved using an immersion medium. [80]

The distance between the last lens of the objective and the specimen is called **working distance**. It decreases with the increase of the objective magnification and numerical aperture. [80]

Slide thickness represents the value of the microscopic slide thickness used during the design of the objective. If this value differs from the microscopic slide used, it can come to unwanted aberrations, i.e. the light will not be focused to the specimen, but spread over. [81]

For live cell imaging, an on-stage sample heater was available to keep the temperature of the cells constant. In this way the cells were not influenced by temperature fluctuation.

The software Olympus Fluoview Ver.4.0a was used to operate the microscope and define different parameters and settings. The most relevant functions are marked in Figure 3.2 and will be explained.

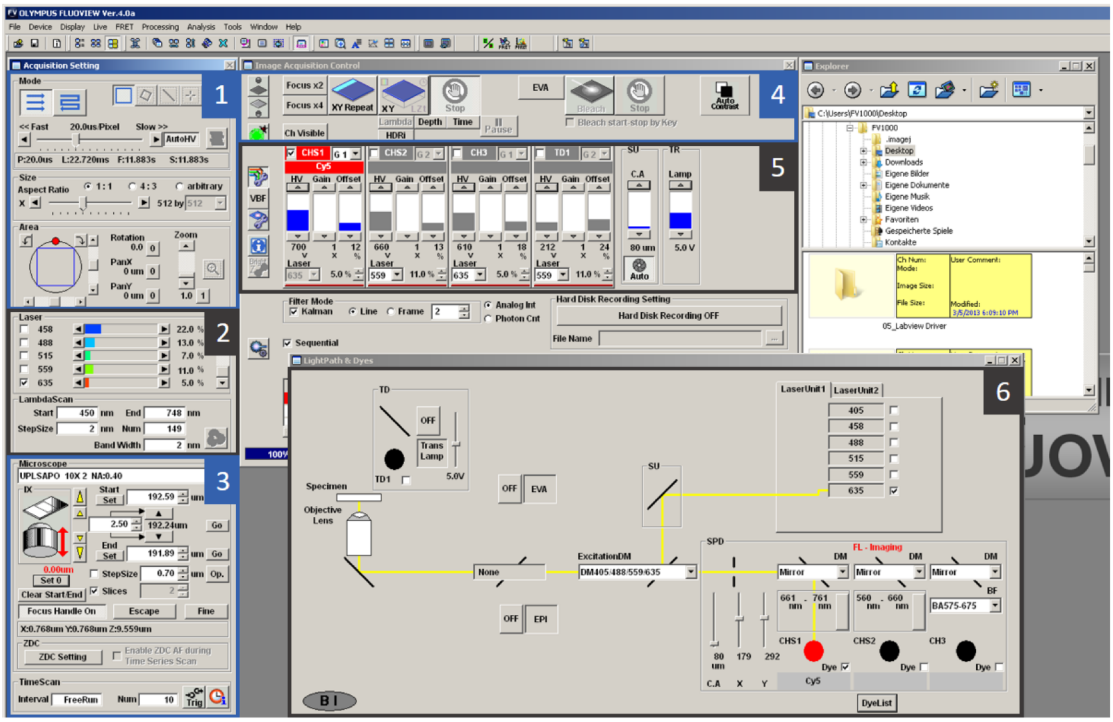

Figure 3.2: Screenshot of the Olympus Fluoview Ver.4.0a software

The software contains three main windows where different parameters can be set. First of them is **Acquisition Setting** divided into three parts. The first part, marked with 1 in Figure 3.2, enables the setting of the imaging parameters as scanning speed, aspect ratio of the image, rotation and zoom. In a second part (2) the user can choose wavelength and laser power in percent for the laser used for imaging. In the third part (3) one of the available objectives can be chosen and fine or coarse focus adjustment can be made. When the focal plane of interest is found it can be set as zero, using the Set 0 function. This can be used for example to measure the height of the sample, i.e. the bottom focal plane of the sample is set as 0 and the top focal plane can be found. The distance between the two focal planes, presenting the height of the sample, is shown. In the same part of the Acquisition Setting window the start and the end point of a z-stack of images, as well as the step size between two images can be set. For time-lapse microscopy the number of images to be taken can be given.

The second window, **Image Acquisition Control**, contains two important parts for this thesis. In the first one (4) XY Repeat or XY functions can be chosen. The XY Repeat function starts live scanning and the XY function starts recording. Additional functions for z-stack recording (Depth) or time-laps (Time) can be selected as well. In the second part of this window (5) detector settings for all three possible fluorescence channels and the one conventional light channel can be set. Those are HV (high voltage), Gain and Offset allowing fine tuning of the detector's sensitivity.

In the third window, **LightPath & Dyes** (6) the light path through the microscope and the used laser unit can be seen. Clicking on the DyeList button, a

new window with a list of available filter sets opens. The required filter set can be chosen and additionally adjusted.

Due to the complexity of the described software, only functions and features required for this thesis were explained.

3.3.2 Cell imaging procedure

The measurements and the corresponding imaging can be divided into three parts. The first part deals with the **determination of suitable staining parameters** of used fluorochromes for every cell line. In this part, simple 2D imaging was made. In the second part the **morphology of the cell lines** and observed cell organelles was investigated. To get the 3D visualisation of the cells, z-stacks were made. The third and the most complex part deals with **irradiation of the cells with acoustic waves** exhibiting frequencies from 0.5 kHz to 10.0 kHz. For this purpose time-laps imaging was made. Due to the different microscope setup and imaging method, the method used in the third part will be explained in Section 3.4 which deals with the acoustic wave irradiation setup, measurement realisation and data analysis.

Determination of suitable staining parameters

The problems which occur during live cell imaging (see Section 2.3.4) can be substantially reduced using suitable staining parameters, i.e. duration of the staining (staining time) and the concentration of the fluorochrome (staining concentration). To determine suitable staining parameters of every fluorochrome for the observed cell lines, the cells were first stained with three to five different staining concentrations keeping the staining time constant. When a suitable staining concentration was determined, a variation of the staining time was made. The imaging procedure for finding suitable staining concentration and staining time was the same.

The cells were stained as explained in Subsection 3.2.2 and set into the sample heater at the Olympus Fluoview 1000 microscope. The sample heater was closed and set to keep the cell temperature constant at 37°C. The laser and the filter set suitable for the used fluorochrome was chosen as well as the image parameters and objective. Images were made using objectives of 10, 20 and 40 times magnification. The image and scanning parameters were kept constant for each objective. The images of 512 Px x 512 Px were taken at a scanning speed of 20 $\frac{\mu s}{Px}$ without additional zoom or rotation. Three different laser powers were used and the detector settings HV, Gain and Offset were kept constant.

After all parameters had been set, the focal plane of interest had to be determined. By looking through the z-axis of the cells, the most suitable x-y-plane, i.e. where the biggest part of the cell organelle was clearly visible, was chosen. For example, the middle of the cell nuclei or the bottom of the cell membrane where the filopodia can be seen. It was always taken care that the number of cells in the images for each fluorochrome was similar.

When the image plane of interest had been found the images were made with three different laser powers. Then the objective was exchanged, the image plane was adjusted and the images were taken with the same three laser powers. This

was repeated for the three objectives of interest. The same procedure was then repeated for the other staining concentrations/staining times of the observed fluorochrome and cell line. To ensure comparable results between different staining concentrations and staining times, the same three values of laser power were used. The collected images were then analysed to find suitable staining parameters.

Cell morphology measurements

Cell morphology measurements were made to calculate the volume of the organelles of interest for every cell line used. This enabled a detailed characterisation of the cells and a comparison of the cell lines. The main objective is to investigate the differences between cancer, dysplastic and healthy cells as well as the differences between cancer cell lines of different origin. For this purpose, z-stack image sets were made which can later be visualized as 3D images of the cells.

The cells were prepared as described and imaged using the Olympus Fluoview 1000 microscope. When the proper laser and filter set was chosen the image size of 512 Px x 512 Px and scanning speed of 20 $\frac{\mu s}{Px}$ was set. The cell line DOK was, due to the size of its cells, imaged using the objective with 40 times magnification. All the other cell lines were imaged with the 60 times magnification objective and water as an immersion medium.

Only the x-y-plane is shown in an image of the cells. To get 3D visualisation of the cells, several images must be taken along the z-axis. The top of the cells was found and the plane above was marked as start position. Moving the focal plane, the bottom of the cells was found as well as the glass dish. The glass dish was marked as the end point to ensure that every cell plane was imaged. The Olympus Fluoview 1000 microscope allows the user to set the distance between two images, the step size. During this measurements, the step size was exactly the size of one in-plane pixel, which yields an identical resolution in x, y, and z-direction. For the imaging with the 40 times magnification objective the step size was 0.621 µm and for the objective with 60 time magnification 0.414 µm. When start and end imaging positions and the step size had been determined, the z-stack was made. Data analysis was made using the software described in the following subsection.

3.3.3 Data analysis

The analysis of the images collected to determine suitable staining parameters was made using ImageJ, a Java based image processing software. After the image of the cells was imported into ImageJ, it was transferred into High-Low mode. This mode marks the pixel with 4096 counts of the 12-bit image as red and the pixel with 0 counts as blue. All the other pixels are shown in grey scale. In this way the amount of oversaturated (red) and undersaturated (blue) pixels can be determined. The histograms of the pixel brightness distribution were made to simplify the determination of suitable staining parameters. Figure 3.3 shows the example of the image in High-Low mode and corresponding pixel brightness distribution histogram.

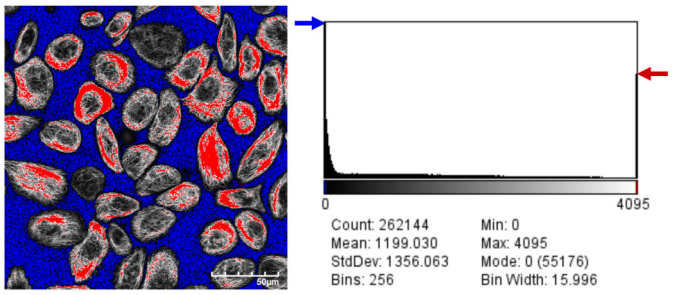

Figure 3.3: High-Low image of the cells with oversaturated pixel marked red, undersaturated pixel marked blue and other pixel in grey scale (left) as well as histogram of pixel brightness distribution (right)

The images with a lot of oversaturated pixels and a pixel brightness distribution shifted to the right part of the histogram were not taken into consideration for further analysis. In the a second step, the dark images, where the cell structure cannot be distinguished clearly, were sorted out. The suitable staining concentration or staining time was determined based on the images of the cells with a low concentration or even without oversaturated pixels where the cell structure could be observed in detail.

For the morphology investigation, a software able to make a 3D image from several z-stack images, recognize the individual cells and calculate their volume was required. Dedicated image processing software like Amira [82] and Voloom [83] include features for cell segmentation and volume calculation but require commercial licenses. Another disadvantage of Voloom is the lack of support of some file types used in confocal microscopy [83]. One of the most common open source image analysis software platforms, ImageJ, has a Volumes plugin enabling volume calculation [84]. The main disadvantage of this software is the need for manual segmentation of every cell on every slide of the image sequence. Additionally, because every area that should be taken into the calculation must be marked manually, the results are strongly influenced by user's precision. The benefits and disadvantages of the different software available prompt the author to search for a more suitable solution. In cooperation with Mr. Niklas Ullrich a MATLAB-based script for 3D visualization of the cells and volume calculation was developed. The developed script enables 3D visualization of the image stacks, recognizes and numbers the individual organelles and calculates their volumes.

After the image stack has been imported, the script generates a binary image using a brightness threshold. The cells in contact with the image edge, whose whole volume is not shown in the image sequence, can be sorted out, as well as overlaying cells. In case of the whole cell volume investigation, made by cell membrane staining, hollow areas can be filled out to ensure that the whole cell volume was taken into calculation. In case of cytoskeleton filaments, which have a network structure, this step can be skipped.

The script recognizes individual cells in 2D images, numbers them and automatically matches sections of the same cell over multiple images. When the cells due to cell-cell contact could not be recognized as individual a manual segmentation was made using ImageJ. The segmentation image was imported and the separation of

the cells was made by the software. For *one z-stack* only *one segmentation image* is *required*. Figure 3.4 shows the numbered cells and the segmentation mask for the cell line DOK.

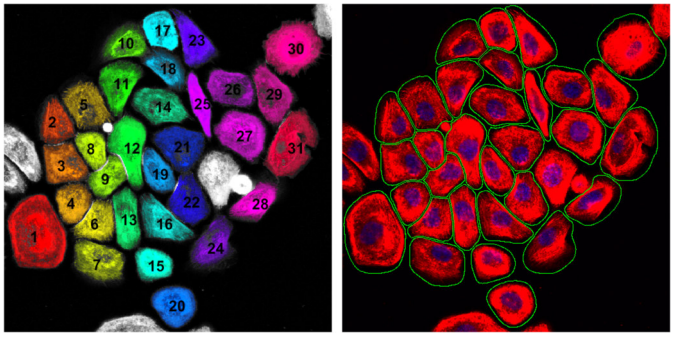

Figure 3.4: Evaluation of actin filaments for DOK cell line: numbered cells taken into calculation (left) and segmentation mask (right)

Afterwards, the script generates an image stack with highlighted areas considered for volume calculation. If the highlighted area does not match the volume to be calculated, this can be adjusted by customising the brightness threshold. As output, the script generates an Excel document containing, among other, the name of the image stack, the threshold value used, image resolution, cell number and volume in pixel. A detailed description of the MATLAB-script can be found in Strugacevac et al.: *Development of a new software for (semi-) automatic segmentation of 3D-objects*.

To enable a comparison between cell organelles of different cell lines, all cell organelle volumes had to be scaled with respect to the volume of a whole cell. In the best case, each organelle volume should be scaled to the overall cell volume of the same cell. Here, the following problems occur. As the cell membranes of the cells in a cell layer are more in contact to each other compared to the cell organelles like mitochondria, or even cytoskeleton filaments, it is hard, sometimes impossible, to distinguish between two cells. Therefore, this would substantially reduce the number of investigated cells. Problems during simultaneous staining of some of the investigated organelles and cell membrane arise as well. Due to cross-talk and bleed-through effects some fluorochromes cannot be combined with the fluorochrome for cell membrane staining. As there are not many fluorochromes available for live cell imaging of some organelles, replacing the fluorochromes was not an option. To avoid the mentioned problems, but still be able to compare cell organelles of different cell lines, the cell organelle volumes were scaled to the average of the overall cell volume of the same cell line.

As a first step of data analysis, the volume values were converted into SI units and the inaccuracy for each cell organelles was calculated. The pixel on the edge of the organelles cannot be clearly assigned, thus the inaccuracy of one pixel at the border between volume taken into consideration and background occurs. To calculate this inaccuracy, the cells were assumed to be oblate spheroids with semi-axis a as equatorial radius and semi-axis c as half of the cell organelle's height. The height of the cell organelle ($2\,c$) can be determined by multiplying the number of slices on which cell organelle appears and the step size used. The second semi-axis,

a can be determined from experimental data using

$$a = \sqrt{\frac{3}{4}\frac{V}{\pi c}} \tag{3.1}$$

where V is the volume of the cell organelle. The inaccuracy, due to imaging, can be calculated by multiplication of the half of the pixel size with the surface of the imaged cells. This surface can be determined using

$$A = 2\pi a\,(a + \frac{c^2}{\sqrt{a^2 - c^2}}\,\mathrm{arsinh}\,(\frac{\sqrt{a^2 - c^2}}{c})). \tag{3.2}$$

If a segmentation mask is used, the inaccuracy of one additional pixel has to be included for the slices of the z-stack with overlaying cells.

When the inaccuracy is calculated for each cell organelle, the ratios of cell organelle to whole cell volume were calculated for every cell line used. Histograms of volume distributions were made and corresponding statistics like maximal and minimal volume ratio, average value and median was calculated. 3D visualisation images of the cell membrane were used to observe the way the cells grew and the visualisation of other observed cell organelles was used for their better characterization.

3.4 Acoustic wave irradiation

Acoustic waves exhibiting frequencies from 0.5 kHz to 10.0 kHz were used to irradiate cancer and dysplastic cells and their response was observed. It was investigated whether the described acoustic waves could induce a resonance catastrophe in cancer cells leading to cell death. The following subsections describe the experimental setup, the method of irradiation and the software for data analysis.

3.4.1 Experimental setup

For the irradiation of cells using acoustic waves, the microscope setup described in 3.3.1 had to be adjusted. The conventional light illumination part was replaced with a piezoelectric actuator and its corresponding stand so that the a tip mounted on a piezoelectric actuator can reach the cells in a Petri dish from above. The changed microscope setup is shown in Figure 3.5.

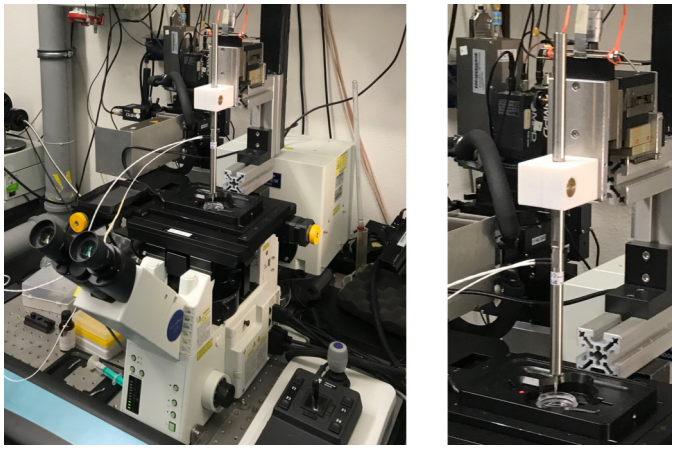

Figure 3.5: Adjusted Olympus Fluoview 1000 microscope setup (left) with piezoelectric actuator P-840.60 (right)

The experimental setup used to observe the reaction of the cells on acoustic wave irradiation consists of three main parts: piezoelectric actuator with a sharp tip used to exhibit the acoustic waves, function generator and amplifier generating voltages to drive the piezo actuator and confocal laser scanning microscope used for cell imaging. Figure 3.6 shows the illustration of the experimental setup.

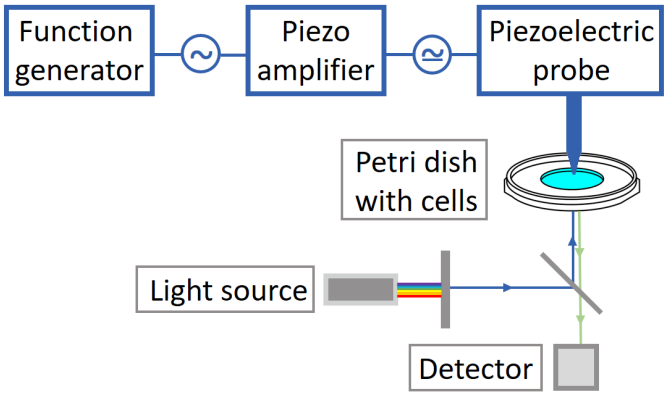

Figure 3.6: Experimental setup used for acoustic wave irradiation of cells

A piezoelectric actuator P-840.60 produced by Physik Instrumente (PI) GmbH & Co. KG was used to exhibit acoustic waves. This is a preloaded longitudinal piezo actuator containing 6 piezo stacks with a maximal travel range of 90 µm at 0 V to 100 V. The mass of the actuator without cable is 62 g with a tolerance of ±5 %.

The actuator is equipped with a temperature sensor. If the temperature of the actuator is out of the operating temperature range (from −20°C to 80°C) the amplifier does not supply any voltage and the actuator is switched off. Further details on the piezo actuator can be found in [85].

On the top of the piezo actuator, a sharp tip shown in Figure 3.7 was mounted. The tip was made of stainless steel 1.4301 (X5CrNi18-10), in this case composed of $70.87\% \pm 0,473\%$ iron, $18.88\% \pm 0,450\%$ chromium and $10.25\% \pm 0.411\%$ nickel in the central workshop of physics at the Heinrich-Heine-University. The sharp tip

has the form of a pencil with about 80 µm diameter at the end.

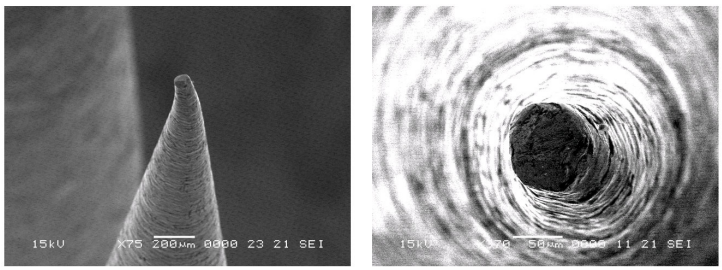

Figure 3.7: Scanning electron microscope (SEM) image of the tip used to exhibit acoustic waves

The voltages required to drive the piezoelectric actuator were generated using a function generator and a piezo amplifier. The frequency and voltage of interest were set on the function generator which generated an according AC voltage. This voltage was then 10 times amplified by a high-power piezo amplifier (E-618.10G) produced by Physik Instrumente (PI) GmbH & Co. KG. Additionally, the piezo amplifier added 20 V DC voltage. This offset voltage deflected the piezo stacks into a start position to allow the motion in positive and negative direction. The AC voltage induces expansion and contraction of the piezo stacks which causes the oscillation of the probe tip.

3.4.2 Irradiation of the cells

To observe the reaction of the cells on acoustic wave irradiation, they were stained with CellMask Green. Staining the cell membrane enables observation of the cell-cell contacts and possible membrane rupture in the case that acoustic waves induce oscillation of the cells with their resonance frequency leading to the cell collapse.

After the cell staining, the cells were put into the sample heater which in this case could not be closed as the tip of the probe (piezo actuator with the sharp tip) had to reach into the Petri dish. Using the microscope software, the laser with 515 nm wavelength and filter setup EYFP was set as well as the desired objective.

When the cells and the microscope had been prepared, the probe had to be set into the right position. Using a micrometer screw the probe was driven into the Petri dish until it reached the medium. The microscope was used to precisely adjust the distance between cells and the probe's tip. First of all, the position of the cells was found. The focal plane in which the cell bottom with the filopodia could be clearly seen was selected and set as $z = 0$. The focal plane was then shifted for the desired distance between the cells and the probe tip, live scanning was started and the probe was driven down until it appeared in the selected focal plane. When the z-plane was determined, the position of the probe in x-y-plane was set, using micrometer screws, in the way that the probe always appeared in the middle of the image. Afterwards, the focal plane was shifted to zero, showing the image of the cells.

In the end, the image and time-lapse imaging parameters were set. As the user cannot set the time duration of imaging, but the amount of the images, this had

to be precalculated. Before the irradiation three images were made, irradiation of 5, 10 or 15 minutes was made, equivalent to 51, 102 or 152 images with a size of 512 Px x 512 Px and scanning speed of $20\frac{\mu s}{Px}$. After the irradiation additional 5 images were taken. In this way the number of required images was determined and set in the microscope software.

After all parameters were set, the irradiation of the cells was done. In one Petri dish maximum 6 measurements were made to avoid the irradiation of the same area two or more times and to influence the measurement results.

3.4.3 Data analysis software

To quantify the reaction of the cells on the acoustic wave irradiation, a suitable analysis method had to be found. As the images were made before, during and after the irradiation, the image before the irradiation (image 3) and image right after the irradiation (image 54, 105 or 155, depending on irradiation time) were compared. The comparison of the images was complex due to several problems. For instance, longer exposure of cells to laser light leads to a photobleaching effect which results in a low, but for data analysis substantial difference in brightness of the two observed images. Furthermore, as some cells in an image appear brighter, the image has to be preprocessed to equalize the brightness of the cells and later on avoid false pixel classifying. Another problem is cells growing over each other, which have to be distinguished as individual. Those issues, occurring during some of the measurements, can be seen in Figure 3.8.

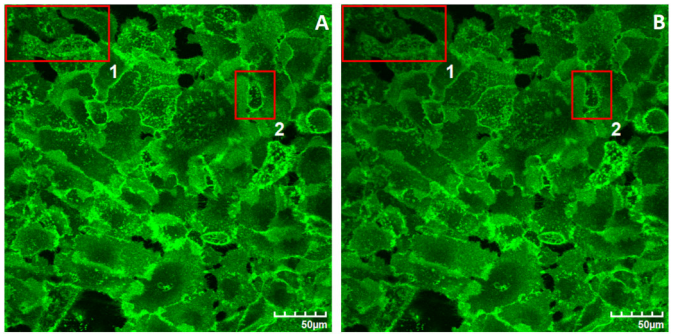

Figure 3.8: Problems encountered during evaluation; image before (A) and after (B) 5 minutes of irradiation

Image A is made before irradiation of the cells and image B after 5 of minutes irradiation. The red rectangle marked with number one highlights two problems. By comparison of the images, it can be seen that the image after irradiation (B) appears darker. The reason for this is photobleaching. Additionally, the same rectangle in image B shows that some cells are markedly darker in comparison to the other cell in the image. The risk of false recognition of cell edge and false pixel classification is very high. The second red rectangle points out the cell growing over the cell layer. This is also challenging for the evaluation as most of software base their evaluation on the increase of the background and do not recognize contraction of those cells.

Different available software have been tested for the comparison of the images, but an open source software able to answer all the challenges has not been found. For instance, ImageJ was used to subtract the last image from the first image and calculate the differences. Its great benefit is the easy handling and quickness. Nevertheless, in the cases when the last image was darker than the first image, pixel, which changed through brightness, and not by the reaction of the cells on the acoustic waves, were taken into the calculation as well. The cell reaction calculated in this way seems to be higher than it really is. When binary images were compared using ImageJ, the cells which appear darker in the image were often recognized as background and their changes have not been taken into calculation leading again to false results.

The image classification and segmentation tool ilastik was tested as well [86]. ilastik is a machine learning tool, which allows the user to mark the cell membrane with one label, cell content with a second and background with a third label. The user can decide which pixel will be marked using which label and by more and more pixels marked, the software learns to recognize which pixel brightness belongs to which label and in the end matches the pixels to the labels automatically. The process of teaching the software to recognize the pixel brightness for each label is very time consuming. If cells with similar pixel brightness are growing over each other or overlay, they cannot be distinguished as individual and the change of the cells cannot be recognized which influences results.

The advantages of the tested software were used to develop a software which can deal with the challenges of this measurement evaluation. A MATLAB-based software for image comparison and calculation of the cell reaction on the acoustic wave irradiation was developed in cooperation with Mr. Niklas Ullrich. The work principle of the software will be explained in the following.

The user can set the path to the folder in which the images to be compared are and the name of the first and the last image. The software then imports the images. The images used during this thesis are declared as unsigned integer number stored with 16 bit (uint16 variables). The highest count that can be stored as uint16 is 65 536. The brightest pixel value in the image is increased to this value, all others are adjusted linearly. In this way, the brightness difference between two images can be reduced.

In the next step binary images are created. All pixels with a brightness value higher than a threshold are defined as white, representing cells, the other pixels are defined as black, representing the background. The threshold value is calculated for every image individually as the average of the pixel brightness. Using this threshold value not just the edge of the cell, but the cell interior as well as overlapping cells can be observed. When the binary images are created, the total number of pixels, the number of white and black pixels and the ratio of white/black pixels to a total the number of pixels are determined.

Following, the binary images were compared pixel by pixel. The number and the ratio of pixels that changed from white in the first image to the black in the second image and vice versa were determined. Figure 3.9 shows the pixel changed from white to black in red, from black to white in green and the pixel which have not changed in blue. In the last step the software calculated the sum and the difference of the changed pixels. The sum of the changed pixels represents a

dimensionless index of the cell reaction on the irradiation using acoustic waves. The difference represents the change of the visible background.

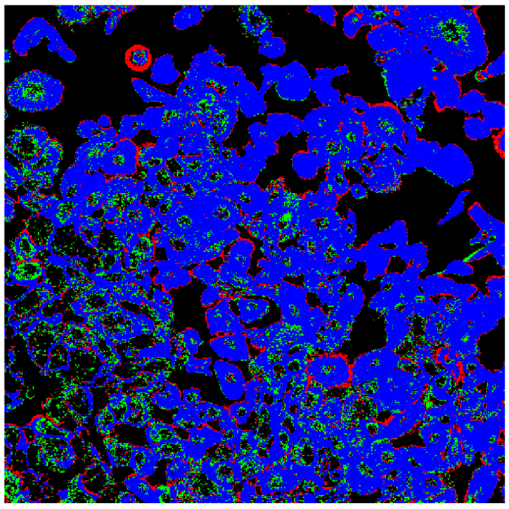

Figure 3.9: Evaluation of the images before and after 5 minutes of irradiation: pixel changed from white in the first image to black in the second image marked as red, pixel changed from black in the first image to white in the second image marked as green, pixel which have not changed as blue.

As an output, the software generates an Excel document containing, among others, the names of the images used for the evaluation, the threshold used for both images, number of overall pixel, number and the ratio of the white pixels on the first and the last image, number and ratio of the white pixels that became black in the last image and vice versa as well as sum and difference as number and ratio.

The software is able to compare a high amount of image pairs successively and write the results in one Excel document what makes data evaluation fast and easy. Nevertheless, the reaction of the cells calculated in this way refers to the reaction of all cells shown in the image and not to the individual ones. Additionally, the software was tested to prove that the number of the cells in the image does not influence the results.

4. Results and discussion

In this chapter the measurement results gained during this thesis will be presented and discussed. The first part deals with staining parameters which had to be determined to ensure a high image quality and to reduce the influence of the observation method on the cells. In the second part, these suitable staining parameters were used to stain the cells to observe their morphology using fluorescence microscopy. Those observations enabled a characterisation of the cells and the comparison between cancerous and healthy cells as well as between cancerous cells of different origin. In the last part the reaction of cells on acoustic wave irradiation was observed. The cells were irradiated in order to examine whether the acoustic waves exhibiting frequencies between 0.5 kHz and 10.0 kHz may induce a resonance catastrophe and destroy cancer cells.

4.1 Suitable staining parameters

To minimize the problems, which occur during fluorescence microscopy (see Subsection 2.3.4), suitable staining parameters must be specified. In this way, better image quality is achieved and the influence on the cells, their morphology and mechanic is reduced. During this thesis, the suitable staining concentration and staining time were determined for the cells of all observed cell lines and used fluorochromes.

4.1.1 Determination of suitable staining parameters

The specification of suitable staining parameters will be explained using the staining of UD-SCC-02 cells with CellMask Green fluorochrome as a typical example. Suitable staining parameters for all other staining kits and cell lines used were determined in the same way and will be given as well. As a first step a suitable staining concentration was ascertained and used for the determination of a suitable staining time. These recommended parameters are generally applicable for the corresponding cell line. The variation of cells' density in-between the Petri dishes differs causing slightly different staining. Therefore, the laser power can be adjusted on demand to equalize those differences. All measurements were made together with students[1] as a part of their Bachelor or Master theses. The author took part in every measurement and made the data analysis independently.

[1] A. Almaci, N. Bartels, L. Hentschel, J. Lietz, M. Plettenberg, L. Rohde, Z. Seghaoui

Staining solution concentration

As a first step, a suitable staining solution concentration was determined. Five different concentrations of CellMask Green staining solution were tested: 0.2 µM, 0.5 µM, 0.8 µM, 1.0 µM and 1.6 µM while keeping the staining time of 15 minutes and the laser power of 10 µW constant. Figure 4.1 shows High-Low mode images in the upper row and the corresponding histograms of the pixel brightness distributions below.

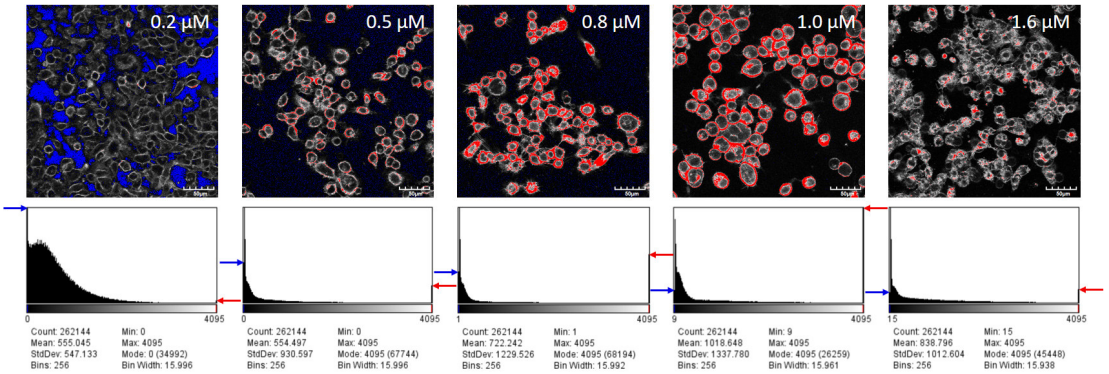

Figure 4.1: Concentration variation of CellMask Green for UD-SCC-02 cells. (Staining time: 15 minutes; magnification: 40 times; laser power: 10 µW)

As can be seen in Figure 4.1, cell staining using 0.2 µM of CellMask Green results in rather dark images and the structure of the cells cannot be clearly distinguished. For that reason, the concentration of 0.2 µM is not taken into further analysis.

Cells stained using 0.8 µM and 1.0 µM concentrations show many oversaturated pixels marked in red. On the corresponding histogram, it can be seen that the number of oversaturated pixels increased markedly compared to the histograms of the cells stained using 0.2 µM or 0.5 µM CellMask Green. The mean value of the pixel brightness distribution for the 0.8 µM concentration is 722 and for 1.0 µM concentration 1019, which are both substantially higher than the mean for the 0.5 µM concentration (555). Therefore, these concentrations are not recommended.

Cells stained using 1.6 µM do not exhibit many oversaturated pixels, even though the concentration of the staining solution was increased. They undergo quenching and should therefore not be taken into consideration.

The histogram of the cells stained using 0.5 µM of CellMask Green shows very few oversaturated pixels with a mean value of 555. Because of the lower number of oversaturated pixels and clearly discernible membrane structures, this is the recommended concentration.

Staining time

The influence of the staining time on the cells was investigated using a constant concentration of 0.5 µM and a laser power of 10 µW. The staining time was varied for 5, 15, 30 and 45 minutes. High-Low images and the corresponding histograms are shown in Figure 4.2.

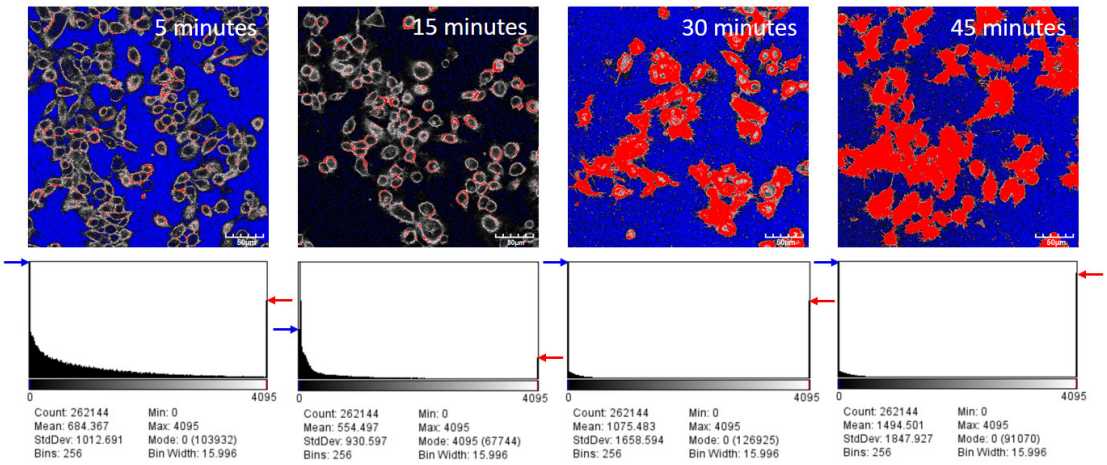

Figure 4.2: Staining time variation of CellMask Green for cell line UD-SCC-02. (Staining concentration: 0.5 µM; magnification: 40 times; laser power: 10 µW)

By observing the images and the pixel brightness distribution histograms for the staining times of 30 and 45 minutes, many oversaturated pixels can be seen. The cell structure cannot be recognized and the mean value for both staining times is particularly high, 1075 for 30 minutes staining and 1494 for 45 minutes. These staining times are too long and not recommended as suitable for cell line UD-SCC-02.

In the images made after a staining time of 5 and 15 minutes individual cells can be distinguished and the cell structure is shown clearly. The mean values of pixel brightness distributions are with 684 for 5 minutes and 555 for 15 minutes notedly lower compared to the mean values for 30 and 45 minutes staining time. As shown, the images of the cells stained for 5 and 15 minutes are very similar what is confirmed by the pixel brightness distribution and its mean value. For that reason, the interval between 5 and 15 minutes is recommended for further staining of the cell line UD-SCC-02 using CellMask Green. This time interval is beneficial when simultaneous staining is made. If the staining time of a second fluorochrome lays in this interval, the staining time of CellMask Green can be adjusted that both fluorochromes are given at the same time, what reduces the probability of operator mistakes during staining.

For all other cell lines and fluorochromes, suitable staining parameters were determined in the same way. Tested staining concentrations and staining times were selected according to recommendations of the fluorochrome's manufacturer.

4.1.2 CellMask Green

Suitable staining parameters of CellMask Green for all cell lines can be seen in Table 4.1.

Cell line	Staining time (minutes)	Staining concentration (µM)
DOK	10	0.8
UD-SCC-01	10	0.8
UD-SCC-02	5 - 15	0.5
UD-SCC-04	10	0.8
UD-SCC-06	10	0.8

Table 4.1: Suitable staining parameters of CellMask Green for all cell lines

As shown, the suitable parameters are identical for all cell lines except UD-SCC-02. CellMask Green binds on the membrane and does not have to diffuse into the cells, what may be a reason for the short staining time and low concentrations.

4.1.3 Cytoskeleton staining kits SiR-actin and SiR-tubulin

The results of the determination of suitable staining parameters for cytoskeleton filament staining are shown in Table 4.2. Images of staining parameter variation for SiR-tubulin and SiR-actin are shown in Appendix A and Appendix B on the example of UD-SCC-01 cells.

Cell line	SiR-actin		SiR-tubulin	
	Staining time (minutes)	Staining concentration (µM)	Staining time (minutes)	Staining concentration (µM)
DOK	45 - 60	0.75 - 1.00	45 - 60	0.75
UD-SCC-01	45 - 60	0.75	60	0.75 - 1.00
UD-SCC-02	45	0.75	30 - 45	0.75 - 1.00
UD-SCC-04	60	1.00	60	1.00
UD-SCC-06	60	1.00	60	1.00

Table 4.2: Suitable staining parameters of SiR-actin and SiR-tubulin for all cell lines

The recommended staining parameters for SiR-actin differ between cell lines. For optimal staining of cell line UD-SCC-02 the lowest concentration and the shortest staining time is required. A reason for this could be that these cells are the smallest of all observed cell lines what would indicate that they have the smallest amount of actin filaments to be stained.

Cell lines UD-SCC-04 and UD-SCC-06 require the highest staining concentration and staining time. A reason for this could be the way the cells grow. As those cells intend to grow in islands and overlap, the fluorochrome has to pass between the cells on top of the island to reach the cells in the middle or at the bottom. In

order to achieve that, a sufficient time interval is required for the fluorochromes to reach the cells in the middle. As some fluorochrome molecules bind on the actin filaments of the cells on the top of the island, the fluorochrome concentration has to be high enough to enable staining of the cells in the middle of the island.

Cell lines UD-SCC-01 and DOK grow in a monolayer and show similarities in cell culture. The suitable staining parameters for these cell lines are similar as well. When the concentration of the cells is higher, it is recommended to increase the staining time to 60 minutes. In case of the DOK cell line it is also possible to increase the concentration of SiR-actin to 1.00 µM.

Suitable staining parameters for SiR-tubulin can be discussed similarly to the ones of SiR-actin. The cell line UD-SCC-02 requires again the lowest staining time, with a suggested increase of the staining concentration for higher cell concentrations. The cell lines UD-SCC-04 and UD-SCC-06 require again the highest parameter values.

In case of SiR-tubulin, cell lines DOK and UD-SCC-01 show similarities as well. If the concentration of DOK cells is higher, an increase of the staining time to 60 minutes is recommended. In case of higher concentration of UD-SCC-01 cells the staining concentration should be increased to 1.00 µM.

4.1.4 Hoechst 33342

Cell nucleus staining was made using Hoechst 33342. The suitable staining parameters are shown in Table 4.3. Images showing the influence of staining time and concentration variation on the cell line UD-SCC-01 can be found in Appendix C.

Cell line	Staining time (minutes)	Staining concentration (µM)
DOK	10	4.05
UD-SCC-01	10 - 15	4.05
UD-SCC-02	5 - 15	3.24
UD-SCC-04	10	0.40
UD-SCC-06	10	0.40

Table 4.3: Suitable staining parameters of Hoechst 33342 for all cell lines

Even though all cell lines require a similar staining time for optimal imaging of their cell nuclei, the staining concentration varies markedly. Cell lines DOK and UD-SCC-01 require the highest staining concentration of 4.05 µM, while cell lines UD-SCC-04 and UD-SCC-06 require only 0.40 µM. As Hoechst 33342 fluoresces only by binding with double-stranded DNA, the amount of DNA in the cell nuclei could be a reason for the different concentrations.

4.1.5 MitoTracker Orange

For adequate staining of the mitochondria the parameters shown in Table 4.4 are recommended. Staining time and concentration variation images for the UD-SCC-01 cells are shown in Appendix D.

Cell line	Staining time (minutes)	Staining concentration (µM)
DOK	10	0.1
UD-SCC-01	5 - 10	0.1
UD-SCC-02	10	0.1
UD-SCC-04	10	0.1
UD-SCC-06	10	0.1

Table 4.4: Suitable staining parameters of MitoTracker Orange for all cell lines

To determine a suitable staining concentration of MitoTracker Orange, concentrations of 0.1 µM, 0.2 µM and 0.3 µM were tested. The lowest concentration of 0.1 µM was shown to be the most suitable one. As the images of cells stained with 0.1 µM showed clearly stained structures of mitochondria and less oversaturated pixel, and a lower concentration could not be tested due to laboratory equipment limits, a concentration of 0.1 µM is recommended for all cell lines with a staining time of 10 minutes.

4.2 Morphology of the cells

Investigating the morphology of cells may lead to new findings on differences between cancerous and healthy cells. Observing the morphology of different cancer cells from the head and neck area can reveal whether the sample origin within the same area has an influence on the cells. This section deals with the volume calculation of whole cells, cytoskeleton filaments, cell nuclei and mitochondria. The measurements were made together with Ms. Nina Bartels as a part of her Master thesis. Data analysis and evaluation was made by the author.

4.2.1 Overall cell volume

Staining the cell membrane allows the calculation of the overall cell volume, which is important to scale other cell organelles of interest, to be able to compare different cell lines. In addition, using images of cell membrane the way the cells grew, their shape and their size can be investigated.

Due to its size, the DOK cell line was imaged using a 40 times magnification objective. Even though a 60 times magnification objective ensures more detailed images with higher resolution, a 40 times magnification objective was chosen to increase the number of cells per image. As the DOK cells are larger compared to the other cell lines used, their cell organelles are large enough to collect detailed images even with 40 times magnification objectives. The other cell lines were imaged using a 60 times magnification objective and water as immersion medium. Figure 4.3 shows 3D-visualisations of all cell lines used.

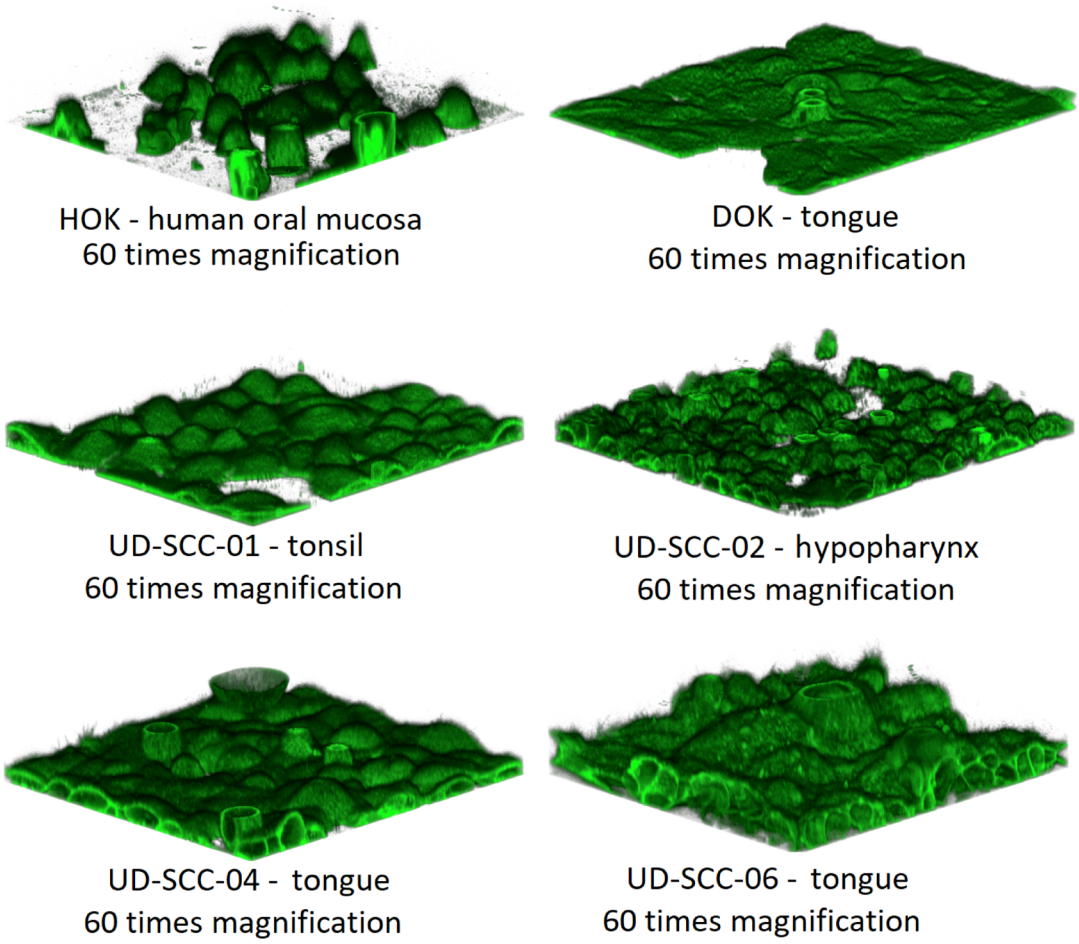

Figure 4.3: 3D-visualisation of the cells stained with CellMask Green

3D-visualisation of the cells shows notable differences between healthy (HOK), dysplastic (DOK) and cancer cells (UD-SCC). HOK cells are markedly higher compared to all other cells, unlike the DOK cells which appear to be the lowest ones. DOK cells have the largest cross section area, while the cancer cell line UD-SCC-02 appears to be the smallest in all three dimensions.

DOK cells seem to have a similar height profile and shape. All of the other cell lines are characterised by irregular shapes combined with different heights of the individual cells. DOK and UD-SCC-01 cells grow in a monolayer and more homogeneously, while the other cell lines overlap and build epithelial multi-layers.

Healthy and dysplastic cells differ in their height, shape and the way they grew. To observe whether those differences are characteristic for these two cell types, further cell lines have to be investigated. Compared to cancer cell lines, DOK cells have a more regular shape, are markedly lower and have a greater cross section area.

Comparing the cancer cell lines, similarities between cell lines UD-SCC-04 and UD-SCC-06 can be noticed. Both cell lines have a similar shape and way of growth. A reason for that may be the same origin, as both cell lines were isolated from

tongue cancers.

To quantify the differences in the size of the cells, the volumes of all cells were calculated using the software described in Subsection 3.3.3. As the cells had cell-cell contact, segmentation masks had to be made. To ensure that the whole cell volume was calculated, the function fill hollow areas was used. Due to the overlap of the cells and a lot of cell-cell contacts, the number of evaluated cells was reduced compared to other investigated cell organelles. The calculated volumes and corresponding statistics are shown in Table 4.5.

	HOK	DOK	UD-SCC 01	UD-SCC 02	UD-SCC 04	UD-SCC 06
Number of cells	81	72	74	86	65	47
Average (μm^3)	5184	5923	4384	2466	4295	5454
Median (μm^3)	5193	5402	3721	2350	4124	4826
Maximum (μm^3)	10055	18530	10765	6724	11183	12029
Minimum (μm^3)	1850	2858	1809	336	1772	2357
Inaccuracy	±12%	±16%	±11%	±12%	±11%	±11%

Table 4.5: Average values of overall volume of all investigated cell lines and corresponding statistics

The analysis of the 3D-visualisation images is in agreement with the volume calculation. The DOK cell line has the largest overall cell volume with an average value of $5923\,\mu m^3 \pm 948\,\mu m^3$. Here should be noted that the inaccuracy of the DOK measurements is the largest as well, due to the 40 times magnification objective. The UD-SCC-02 cell line has clearly the smallest cells with an average cell volume of $2466\,\mu m^3 \pm 296\,\mu m^3$.

The cell line HOK shows the largest height profile, but due to their smaller cross section area they have the third largest volume of all compared cell lines with an average value of $5184\,\mu m^3 \pm 622\,\mu m^3$.

Even though cell lines UD-SCC-04 and UD-SCC-06 show similarities in shape and growth, the calculated volumes differ markedly. The UD-SCC-04 cells, with an average value of $4295\,\mu m^3 \pm 472\,\mu m^3$, are smaller than UD-SCC-06 cells ($5454\,\mu m^3 \pm 600\,\mu m^3$). A comparison of the volumes reveals that cell line UD-SCC-04 has a similar average value to cell line UD-SCC-01 ($4295\,\mu m^3 \pm 472\,\mu m^3$ and $4384\,\mu m^3 \pm 482\,\mu m^3$). From this can be concluded that sample origin does not play a significant role regarding the size of the observed cancer cells.

To enable a comparison between the cell lines, the calculated average values of the overall cell volume were used to scale the other cell organelle volumes. For further analysis of overall cell volumes, histograms of volume distribution were made and are shown in Figure 4.4.

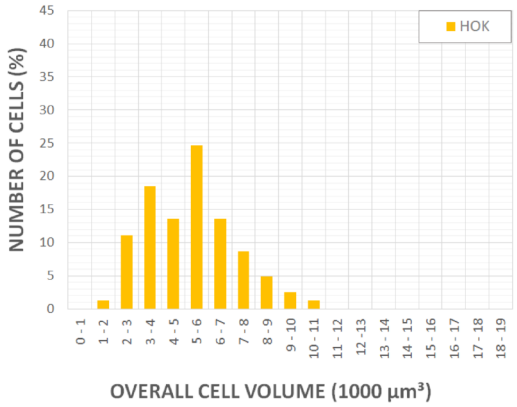

HOK - human oral mucosa

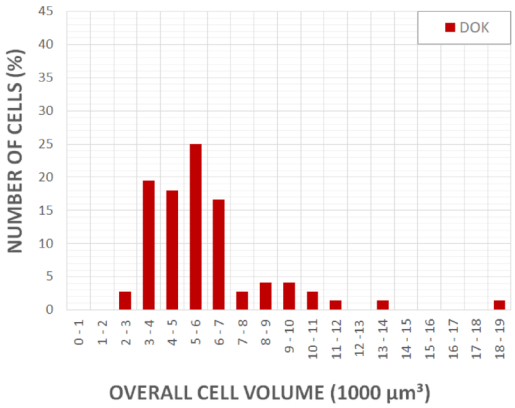

DOK - tongue

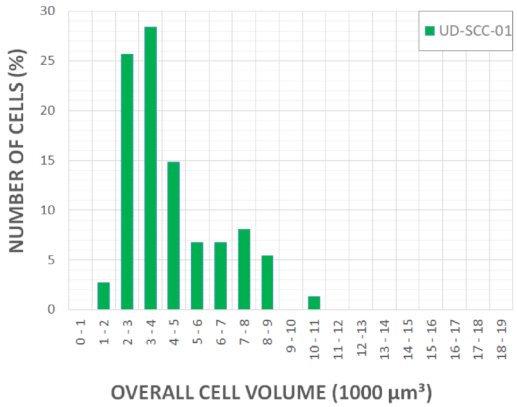

UD-SCC-01 - tonsil

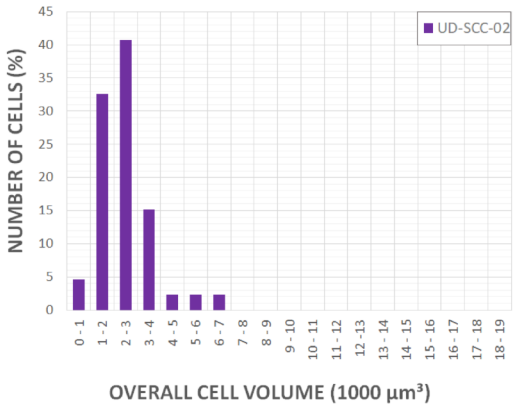

UD-SCC-02 - hypopharynx

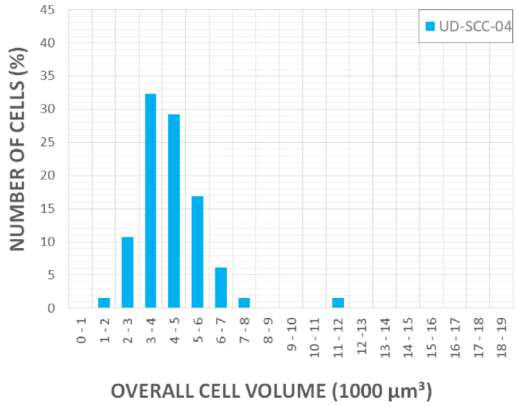

UD-SCC-04 - tongue

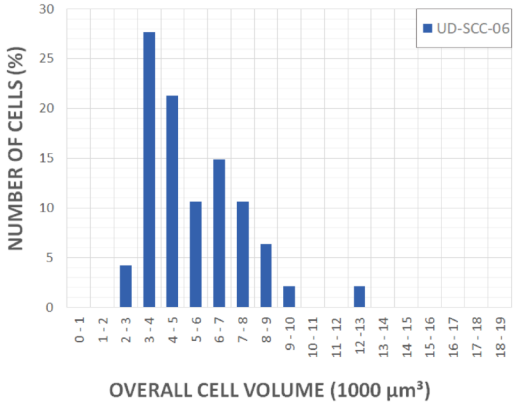

UD-SCC-06 - tongue

Figure 4.4: Distribution of overall cell volume for all cell lines

All the observed cell lines show narrow distributions with a clear maximum value range. DOK cell line has the broadest overall cell volume distribution. The cancer cell line UD-SCC-02 has the narrowest distribution with the clearest maximum area.

The healthy cell line shows the broadest distribution of the area where over two thirds of the cells belong to. This means that the cells within HOK cell line differ the most in shape and volume. Even though the volume distribution of the DOK cell line is dispersed, by observing the area where the most cells belong to, it is clear that the differences between the cells are not substantial.

Comparing the cancer cell lines it can be noticed that the cell lines UD-SCC-02 and UD-SCC-04 have a narrower distribution unlike the cell lines UD-SCC-01 and UD-SCC-06. Cells within UD-SCC-06 differ the most in their volume compared to other cancer cell lines.

4.2.2 Cytoskeleton filaments

The cytoskeleton filaments characterisation of the observed cell lines is of interest as the cytoskeleton has a great influence on the cell elasticity. Microtubules and actin filaments were observed to investigate differences between healthy, dysplastic and cancerous cell lines.

Microtubules

As microtubules have a network structure, 2D images are presented while the 3D-visualisation shows just the outside shape of the network and less microtubules structure. Microtubules of the observed cell lines are shown in Figure 4.5.

Analysing the images of the microtubules filaments it can be seen that all of the cell lines have a very well developed microtubules network spreading from the cell nucleus to the membrane. The DOK cell line has the most structured and homogeneous network, unlike the cell line UD-SCC-02 whose network is most chaotic and inhomogeneous. In comparison to all other cell lines, a differentiation between the microtubules of different cells can be made for the cell lines DOK and UD-SCC-01.

Comparing healthy and dysplastic cells it is noticeable that dysplastic cells have a more structured and homogeneous network in comparison to healthy cells which have more cell-cell contact. This makes it not easy to distinguish which fibers originate from which cell. Besides that, it appears that dysplastic cells contain more microtubules compared to the healthy cells.

Cell line UD-SCC-01 has the most structured network of all cancer cell lines with clear borders to other cells which is not the case for cell lines UD-SCC-04 and UD-SCC-06. These cell lines have interwoven networks extending from the nucleus to the membrane. Again, these two cell lines appear to have the most similarities. UD-SCC-02 cell line has the most unstructured network with the highest density around the cell nucleus decreasing towards the cell membrane.

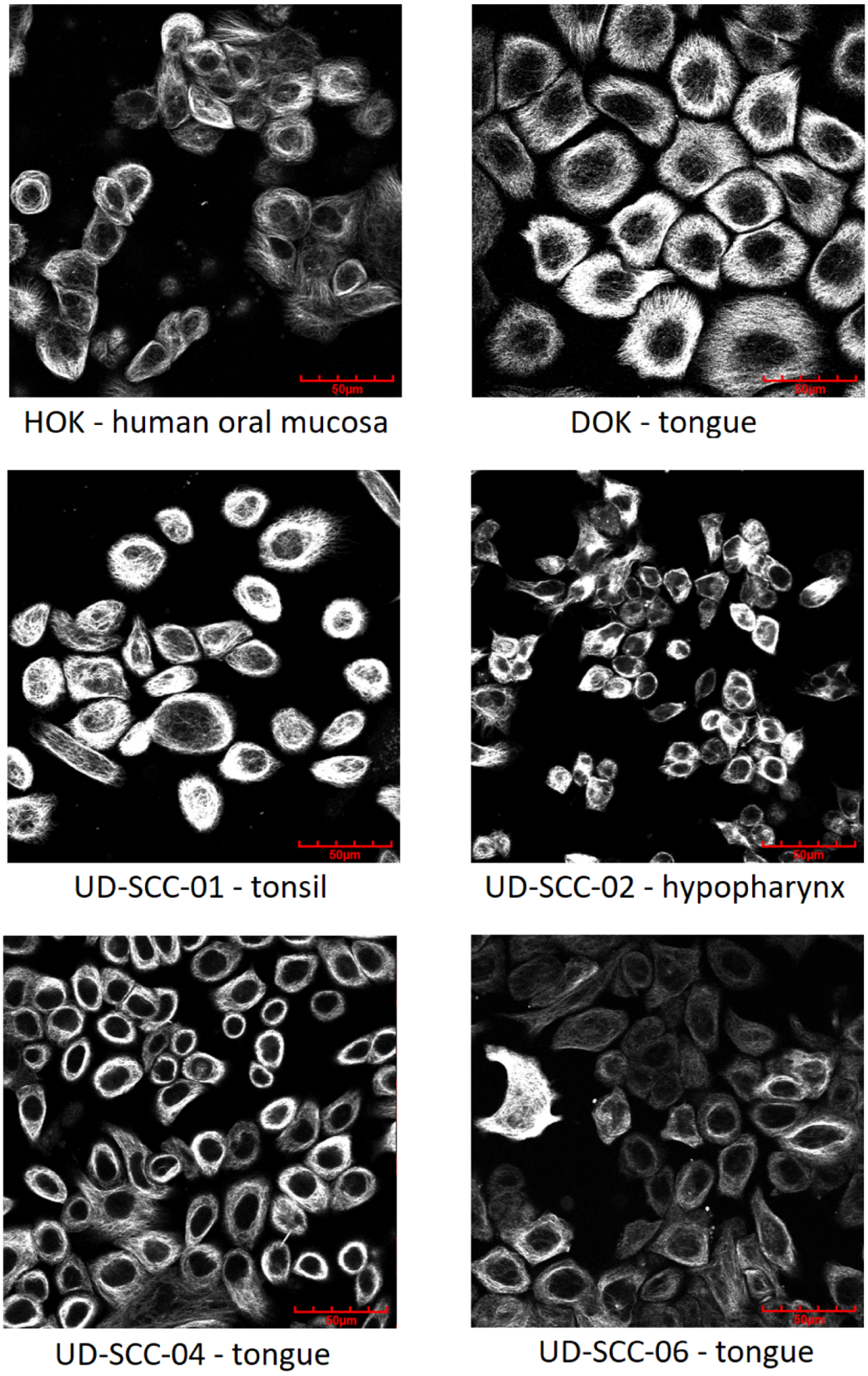

Figure 4.5: The microtubules of observed cells

The volumes of microtubules filaments were calculated for every cell line and will be presented as ratios of microtubules volume to overall cell volume to enable a comparison between the cell lines. As microtubules have a network structure, during volume calculation the function to fill hollow areas was not used. The average values of microtubules to overall cell volume ratios and corresponding statistics are shown in Table 4.6.

	HOK	DOK	UD-SCC 01	UD-SCC 02	UD-SCC 04	UD-SCC 06
Number of cells	90	270	228	101	207	109
Average (%)	44 ± 10	50 ± 21	55 ± 12	43 ± 10	44 ± 10	37 ± 8
Median (%)	42 ± 10	49 ± 20	52 ± 11	41 ± 10	42 ± 9	37 ± 8
Maximum (%)	86 ± 20	94 ± 39	98 ± 21	99 ± 23	93 ± 20	71 ± 15
Minimum (%)	14 ± 3	22 ± 9	18 ± 4	16 ± 4	6 ± 1	7 ± 2

Table 4.6: Average values of microtubules to overall cell volume ratios of all investigated cell lines and corresponding statistics

Even though the image analysis indicates that DOK cell line has the greatest microtubules to a overall cell volume ratio, this is not the case. Cell line UD-SCC-01 has, with an average value of $55\,\% \pm 12\,\%$, the greatest microtubules network. That may be explained with the fact that the DOK cell line has a markedly lower height profile and despite the largest cross section area, a lower volume. Cell line UD-SCC-06 has, with an average value of $37\,\% \pm 8\,\%$, the lowest microtubules to overall volume ratio.

The cell lines HOK, UD-SC-02 and UD-SCC-04 have similar average values. Despite the differences which were observed during image analysis, substantial differences between those cell lines cannot be confirmed. To better analyse the differences between the cell lines, histograms of the volume distribution were made. Figure 4.6 shows the histograms of all cell lines. The ratios of microtubules to overall cell volume are shown on the x-axis and number of cells on the y-axis.

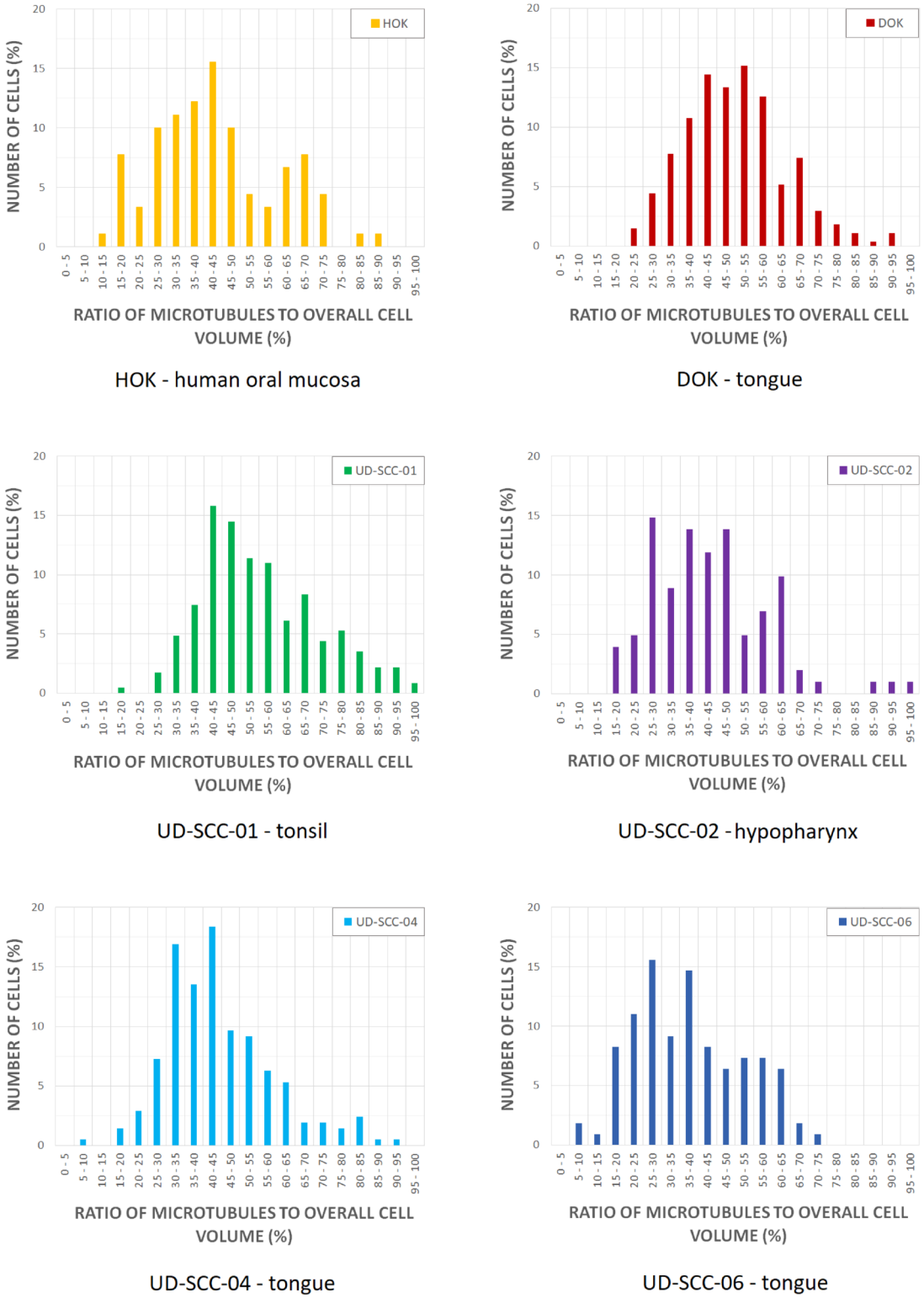

Figure 4.6: Distribution of the microtubules to overall cell volume ratios for all cell line used

The distributions of microtubules to overall cell volume ratios, shown in Figure 4.6, are quite dispersed. Cell line UD-SCC-04 has the broadest distribution unlike cell line UD-SCC-06 which has the narrowest distribution of all cell lines. The distribution of cell line UD-SCC-04 has with 18% the highest maximal value and the cell lines DOK and UD-SCC-02 the lowest (15%).

In comparison to the DOK cell line, where two thirds of the cells have a microtubules ratio between 35% and 60%, the distribution of the HOK cell line is broader. Two thirds of the HOK cells have a microtubules ratio between 25% and 60%. This confirms the image analysis where the DOK cells appeared to be more alike and to contain more homogeneous networks unlike the HOK cells whose microtubules networks differ in homogeneity, density and shape.

Comparing the distributions of the cancer cell lines, it can be noticed that cell lines UD-SCC-01 and UD-SCC-04 have a clear maximal value range unlike the other two cancer cell lines. This means that the microtubules network within the cells of the cell lines UD-SCC-01 and UD-SCC-04 are more alike which is not the case for cells of cell lines UD-SCC-02 and UD-SCC-06. A further comparison of cell lines UD-SCC-01 and UD-SCC-04 shows that the distribution of UD-SCC-01 is shifted to the right, which means that this cells contain greater microtubules networks.

Observing the distributions of microtubules to overall cell volume ratios of healthy, dysplastic and cancer cell lines, substantial differences could not be found. Comparing the distributions of cancer cell lines of the same origin notable similarities were not observed. Thus, the microtubules network of the compared cell lines depends on the specific cell line observed.

Actin filaments

Actin filaments have, like microtubules, a network structure. Therefore Figure 4.7 shows 2D images of the actin filaments to present the structure of the cells. To compare the cells better, images from the stack were chosen to present the plane slightly above the bottom of the cells.

Analysing the images of actin filaments, first what can be noticed is that HOK and UD-SCC-02 cell lines have a markedly smaller cross section area in comparison to the other cell lines. HOK and DOK cell lines have more developed actin networks which is not concentrated just under the cell membrane. Observing cancer cells, the actin filament network is mostly developed under the cell membrane and does not extend deeply to the center of the cell. Actin networks of HOK, DOK and UD-SCC-01 are structured and well-defined what is not case for the other cell lines. Their actin network is inhomogeneous, chaotic and interwoven that makes it not easy to distinguish between the single cells.

The difference between HOK and DOK cell lines is clearly noticeable. The HOK cells have a smaller actin filament cross section area which was already noticed during the analysis of the whole cells. The main difference is that the actin network of HOK cells is more dense and concentrated unlike the one of the DOK cells which is thinner but further spread out.

The actin networks of the cancer cell lines differ as well. UD-SCC-01 cells have the most structured and homogeneous network of all cancer cell lines. It is the only cell line for which a clear distinction between the cells can be made. Cell lines UD-SCC-02 and UD-SCC-04 both show thin networks concentrated under the cell membrane with a lot of contact between the cells. UD-SCC-06 cells have inhomogeneous, but well developed networks with the most cell-cell contact which makes a distinction between the cells complex. The differences between UD-SCC-01 and UD-SCC-02 have been observed. It is questionable whether these differences can be attributed to the different sample origin as the cancer cell lines UD-SCC-04 and UD-SCC-06, both originating from tongue cancer, do not show major similarities.

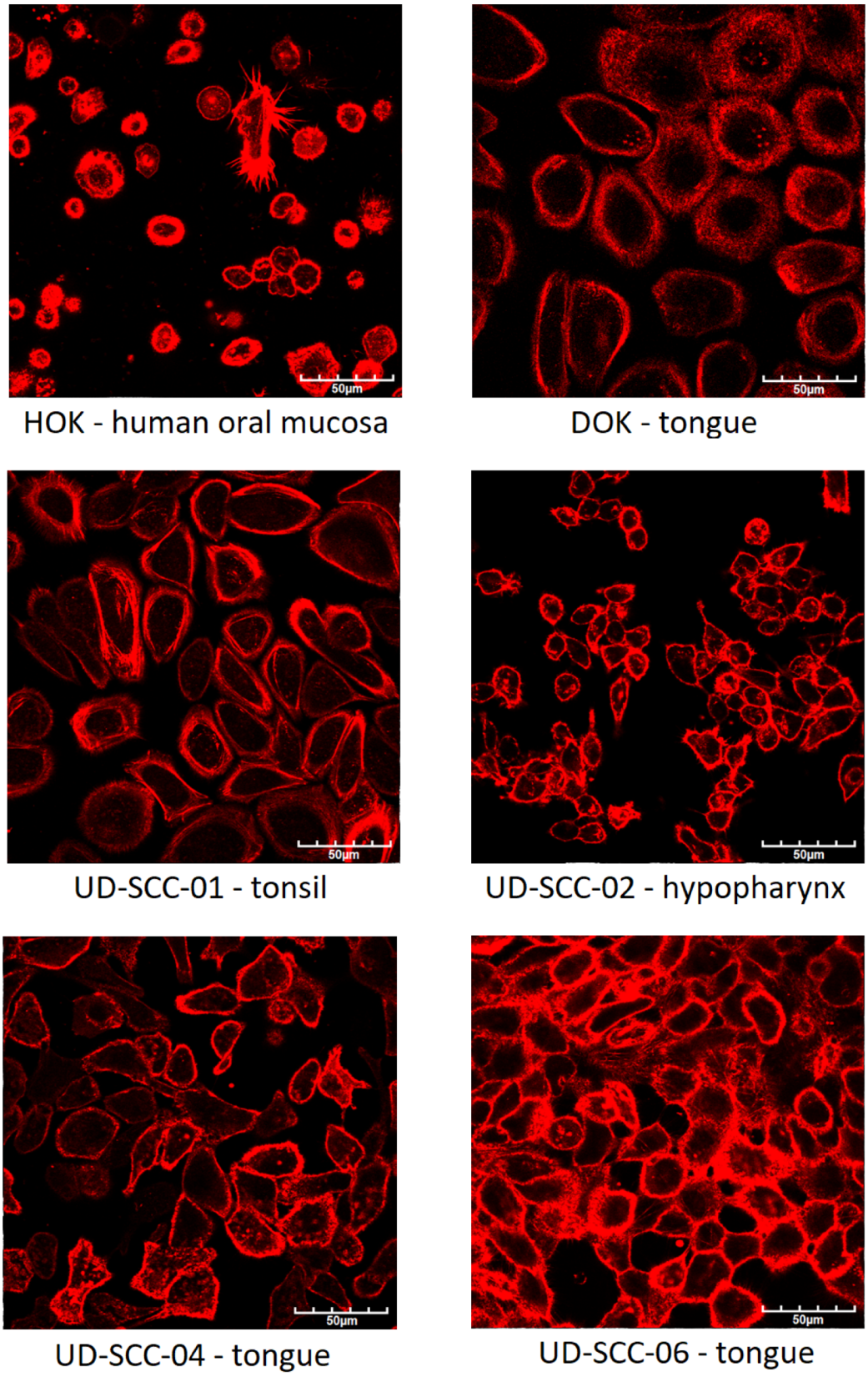

Figure 4.7: Actin filaments network of observed cell lines

The volumes of the actin filaments were calculated to characterize the observed cell lines better. As actin filaments build network structures, like in the case of microtubules, the hollow areas were not filled out. The calculated average values of actin filaments to whole cell volume ratios are given in Table 4.7.

	HOK	DOK	UD-SCC 01	UD-SCC 02	UD-SCC 04	UD-SCC 06
Number of cells	59	104	99	93	125	104
Average (%)	49 ± 12	58 ± 20	48 ± 10	23 ± 5	31 ± 7	52 ± 11
Median (%)	45 ± 11	56 ± 19	49 ± 11	20 ± 5	29 ± 6	49 ± 10
Maximum (%)	90 ± 21	96 ± 34	95 ± 21	54 ± 13	87 ± 19	98 ± 20
Minimum (%)	15 ± 4	27 ± 9	8 ± 2	11 ± 3	5 ± 1	12 ± 3

Table 4.7: Average values of actin filaments to overall cell volume ratios of all investigated cell lines and corresponding statistics

Image analysis showed that DOK cells have the most developed actin network what is confirmed by the volume calculation. With an average value of $58\% \pm 20\%$, the DOK cell line has the highest actin filament to overall cell volume ratio. The UD-SCC-02 cell line has the lowest average value of all cell lines with $23\% \pm 5\%$, what can be seen in the images as a thin and less developed actin filament network.

Dysplastic cells have a higher average value of actin filaments to total cell volume ($58\% \pm 20\%$) compared to healthy ones ($49\% \pm 12\%$). Nevertheless, healthy cells have more compact and dense actin networks what leads to conclusion that even if the actin network volume is lower, healthy cells could contain more individual actin filaments.

Cancer cell lines UD-SCC-01, with an average value of $48\% \pm 10\%$, and UD-SCC-06, with $52\% \pm 11\%$, have markedly higher actin network volumes compared to cell lines UD-SCC-02 ($23\% \pm 5\%$) and UD-SCC-04 ($31\% \pm 7\%$). This was observed in the images as well. Cell line UD-SCC-02 has a thin network located under the cell membrane. The actin network of cell line UD-SCC-04 is more developed, but again concentrated under the cell membrane, unlike the networks of UD-SCC-01 and UD-SCC-06 which are more widespread. Cell line UD-SCC-06 has more cell-cell contact and builds more filopodia and lamellipodia which also contain actin structures. Comparing all cancer cell lines it can be seen that the average volumes differ and are cell-line related. A connection between sample origin and actin filaments volume cannot be confirmed.

To better explore the differences between healthy, dysplastic and cancer cells, the histograms of actin filaments to overall cell volumes were made. Figure 4.8 shows those histograms for all observed cell lines.

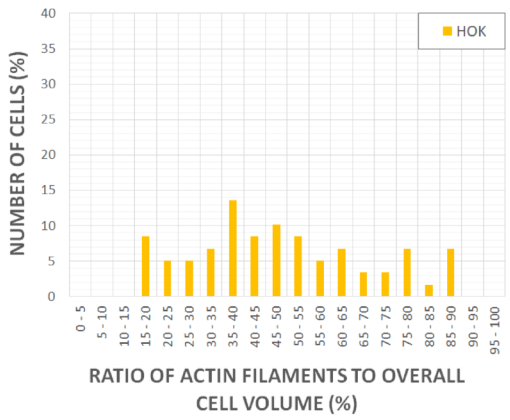

HOK - human oral mucosa

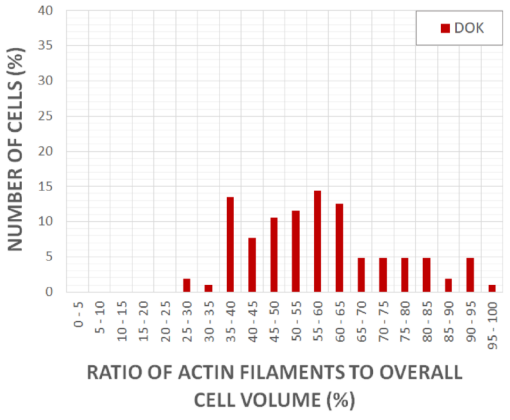

DOK - tongue

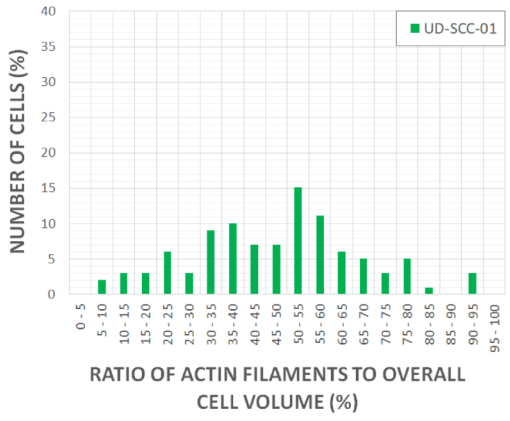

UD-SCC-01 - tonsil

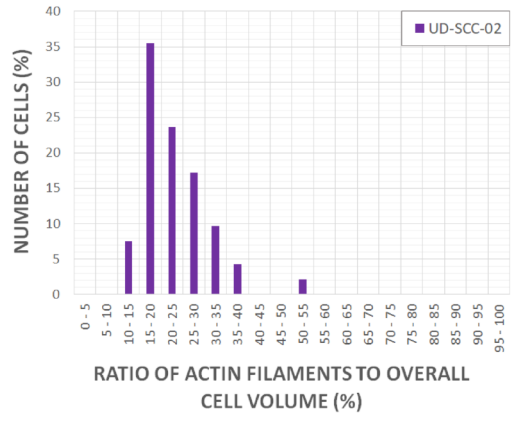

UD-SCC-02 - hypopharynx

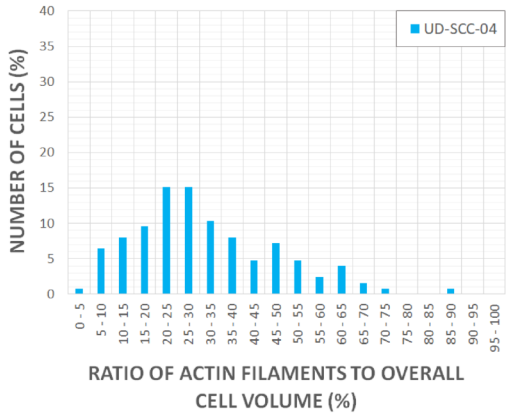

UD-SCC-04 - tongue

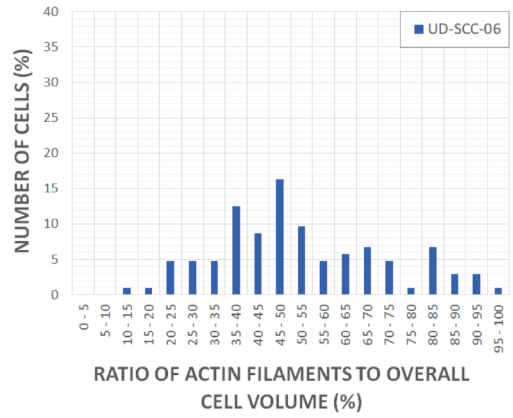

UD-SCC-06 - tongue

Figure 4.8: Distribution of the actin filaments to overall cell volume ratios for all cell line used

The distributions of actin filaments to overall cell volume ratios are very dispersed for all observed cell lines, except for the UD-SCC-02 cell line. Those cells have a narrow distribution with a clear maximum value what leads to the conclusion that their actin filament networks are more alike compared to other cell lines.

Even though the distribution of DOK cells' actin filaments to overall cell volume ratios is dispersed, the area in which the most cells belong to is clearly defined which is not the case for healthy cells. This confirms the image analysis of those cells, where the actin filament networks of dysplastic cells are more alike than the ones of healthy cells.

The distribution of cell line UD-SCC-02 deviates from other cancer cell lines as the most narrow one with the highest maximum value of 35%, while the maximal value of other cancer cell lines is around 15%. However, the maximum value and the region where most cells belong to can be defined. Observing the region where more than two thirds of the cells belong to, cell line UD-SCC-04 has a narrower distribution compared to cell lines UD-SCC-01 and UD-SCC-06 whose distributions are alike. This means that the actin networks of UD-SCC-04 are more similar.

Comparing the distributions of actin filaments to overall cell volume ratios between healthy, dysplastic and cancer cells, it can be seen that cancer cells have clearly defined maximum values. Observing the DOK volume distribution, at least the area where most cells belong to can be easily defined which is not the case for healthy cells. Thus, it can be concluded that the cancer cell lines have a more similar actin structure within the cells compared to dysplastic and healthy cells. This can be connected to the distribution of the overall cell volume which is also narrower for cancer cell lines. As actin filaments are mainly concentrated under the cell membrane, the different size of the cells within the cell line may lead to a different volume of the actin filament network. This could explain why cancer cells have a narrower distribution of actin filaments.

Summary of cytoskeleton filaments observation

Microtubules and actin filaments networks of healthy, dysplastic and cancer cell lines were observed to investigate the differences between those three types of cells, as well as to examine whether the sample origin could play an important role in cytoskeleton properties. All cell lines observed have a very well developed microtubules network compared to the actin filaments network, where some cells have just a thin network located under the cell membrane. The distributions of microtubules to overall cell volume ratios are narrower compared to the actin filaments to overall cell volume ratio distributions. This indicates that the microtubules network of the cells are more alike than actin filament networks. Only cell line UD-SCC-02 is an exception to this rule.

Comparing average ratios of actin filaments to the ones of the microtubules, it can be seen that healthy and dysplastic cells have a greater actin filaments volume then microtubules. Cancer cell lines UD-SCC-01, UD-SCC-02 and UD-SCC-04 have more microtubules than actin filaments unlike the cancer cell line UD-SCC-06 which has larger actin network.

The healthy and dysplastic cell lines have more actin filaments compared to cancer cell lines UD-SCC-01, UD-SCC-02 and UD-SCC-04. Knowing the fact that actin filaments contribute to cell elasticity more than microtubules [39], the question arises whether the observed cancer cells are more elastic than dysplastic and healthy ones. Observing actin filaments and microtubules of cancer cells, no clear statement about the influence of the sample origin on the cytoskeleton filament properties could be made.

4.2.3 Cell nuclei

The image stacks of the cell nuclei were used to test the automatic segmentation of the cells. As there is almost no overlap between cell nuclei, those stacks could be segmented without using segmentation masks. Cell nuclei were also stained in combination with microtubules, actin filaments and mitochondria. This enabled subtraction of the cell nucleus volume from the volume of the observed organelle. Even though an overlap of the cell organelle of interest and the cell nucleus within the cell is not possible, this can sometimes be monitored on the image stacks, e.g., due to florescence light from the planes below the focal plane. In this way a higher accuracy is achieved.

The fluorochrome Hoechst 33342, used for cell nuclei staining, fluoresces by binding with double-stranded DNA. This means that the cells are stained regardless of the cell cycle phase. As the size of the cell nucleus depends on the phase which the cell is in (see Subsection 2.1.3), the analysis of the cell nuclei volume without knowing the phase in which the cell is does not yield biologically relevant results. Using this staining, it is not possible to know how many cells of the observed cell line have, e.g., just divided from the mother cell and started the first growing phase (G_1 phase), and how many cells are already at the end of the second growing phase (G_2 phase) and prepare for nuclear division where the volume of the nucleus is the largest. A comparison of the cell nuclei of different cell lines stained in this way could lead to false conclusions and is not meaningful.

Despite the described problems and for the completeness of the results, images of the nuclei central cross section for all cell lines used were made, as well as the histograms of the nuclei to overall cell volume ratios. Both can be found in Appendix E.1 and Appendix E.2. The average value of cell nuclei to overall cell volume ratios and corresponding statistics were made as well and are shown in Table 4.8.

	HOK	DOK	UD-SCC 01	UD-SCC 02	UD-SCC 04	UD-SCC 06
Number of cells	177	483	335	275	253	221
Average (%)	22 ± 5	33 ± 15	43 ± 9	29 ± 7	17 ± 4	23 ± 5
Median (%)	20 ± 5	30 ± 13	41 ± 8	27 ± 7	16 ± 4	22 ± 5
Maximum (%)	51 ± 12	94 ± 41	88 ± 18	78 ± 19	36 ± 9	92 ± 21
Minimum (%)	6 ± 1	9 ± 4	13 ± 3	14 ± 3	5 ± 1	5 ± 1

Table 4.8: Average values of cell nuclei to overall cell volume ratios of all investigated cell lines and corresponding statistics

As it can be seen, the average value of HOK, UD-SCC-04 and UD-SCC-06 cell line's nuclei volumes are alike. Nevertheless, it is important to mention that one of the cancer cells' characteristics is more frequent division of the cells and passing through the cell cycle faster than healthy cells. As the cells of one cell line do not divide simultaneously and the length of the cycles of cancer and healthy cells differs, it is impossible to make a statement on similarities or differences between the cell lines without knowing the phase in which the cell was.

4.2.4 Mitochondria

Using MitoTracker Orange, active mitochondria were highlighted to investigate the differences between the observed cell lines. According to the Warburg effect [26], the metabolism of cancer cells is modified and they gain energy through lactic acid fermentation out of the mitochondria. One more characteristic of cancer cells is that they do not undergo apoptosis, by which mitochondria play an important role as well. Thus, the question arises, whether cancer cells contain less active mitochondria compared to healthy or dysplastic cells. Therefore the comparison of healthy, dysplastic and cancer cell lines was made. Images of stained active mitochondria are shown in Figure 4.9.

Analysing the images of active mitochondria it is noticeable that DOK, UD-SCC-04 and UD-SCC-06 cell lines have more active mitochondria compared to the other cell lines. Unexpectedly, the healthy cell line appears to have the least active mitochondria. Cancer cell lines have a higher density of mitochondria, which are more compact, unlike the ones of healthy or dysplastic cells.

Healthy cells have less mitochondria, which are mostly located around the cell nuclei, compared to dysplastic cells whose mitochondria are spread throughout the entire cells. The mitochondria compactness of both cell lines is similar.

Cell lines UD-SCC-01 and UD-SCC-02 appear to have less active mitochondria in contrast to cell lines UD-SCC-04 and UD-SCC-06. In addition, their mitochondria are mostly localized close to the cell nuclei whereas the mitochondria of cell lines UD-SCC-04 and UD-SCC-06 spread across the entire cells. Both cell lines originating from tongue cancers show similar mitochondrial structures, density and compactness.

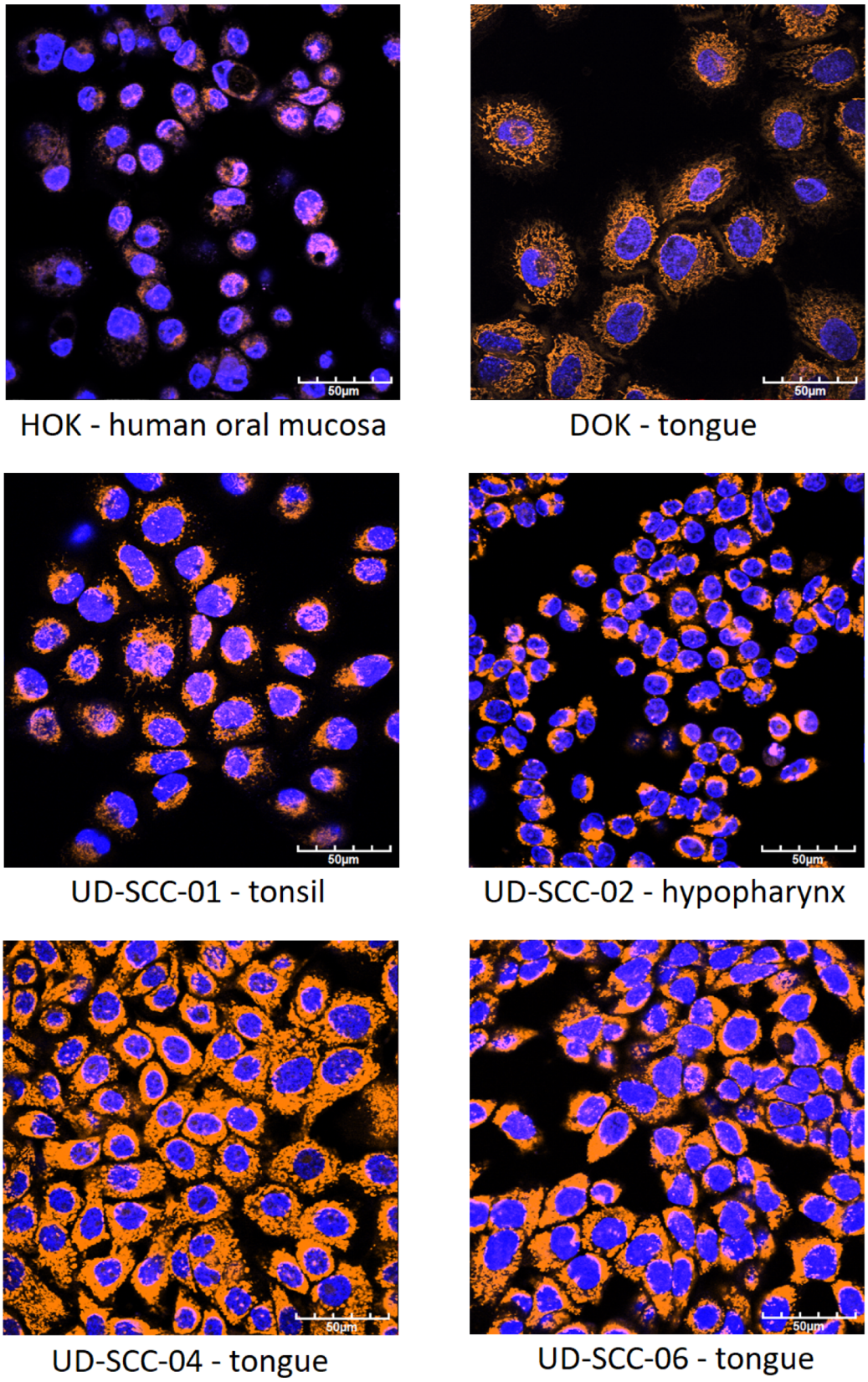

Figure 4.9: Active mitochondria (orange) and cell nuclei (blue) of used cell lines

Comparing healthy, dysplastic and cancer cell lines, the differences between their cells were observed. To better analyse these differences, average values of mitochondria to overall cell volume ratios were calculated and are presented in Table 4.9.

	HOK	DOK	UD-SCC 01	UD-SCC 02	UD-SCC 04	UD-SCC 06
Number of cells	82	261	179	166	127	107
Average (%)	7 ± 2	53 ± 24	11 ± 2	19 ± 4	27 ± 6	21 ± 5
Median (%)	6 ± 1	52 ± 23	10 ± 2	18 ± 4	25 ± 6	19 ± 4
Maximum (%)	37 ± 9	96 ± 43	41 ± 9	60 ± 14	62 ± 13	60 ± 13
Minimum (%)	0 ± 0	14 ± 6	0 ± 0	1 ± 0	6 ± 1	2 ± 1

Table 4.9: Average values of mitochondria to overall cell volume ratios of all investigated cell lines and corresponding statistics

Volume calculation confirmed the image analysis. The HOK cell line has the least active mitochondria with an average value of $7\% \pm 2\%$, followed by UD-SCC-01 ($11\% \pm 2\%$) and UD-SCC-02 ($19\% \pm 4\%$) cell lines. The DOK cell line has the highest average value of mitochondria to overall cell volume ratios of all investigated cell lines with $53\% \pm 24\%$. Even though cell line UD-SCC-04 has a markedly lower average value compared to DOK ($27\% \pm 6\%$ to $53\% \pm 24\%$), the compactness of its mitochondria is notably higher. Thus, it could be that this cell line contains more single mitochondria. UD-SCC-06 cell line has, as it can be seen in the images as well, a similar mitochondrial structure to UD-SCC-04 cell line, with an average value of $21\% \pm 5\%$.

The histograms of mitochondria to overall cell volume ratio distributions were made for further analysis of active mitochondria. Those are shown in Figure 4.10.

The HOK cell line shows the narrowest distribution of the mitochondria to overall cell volume ratios with the highest maximal value of 41%. This was expected, due to less mitochondria seen in the images and the lowest average value of their volume. The DOK cell line has the most dispersed distribution, unlike the cancer cell lines which have a narrow distribution with a clear maximal value area.

The distributions of healthy and dysplastic cell lines are totally different. The healthy cell line has a narrow distribution with a clear area where the most of the cells belong to, what is not case for DOK cells. Their distribution is very broad and the area where two thirds of the cells belong to extends from 35% to 70% of active mitochondria to overall cell volume ratio.

Cancer cell lines show similar distributions which are narrow and differ in the shift on the x-axis due to the volume of the mitochondria. Comparing the areas where two thirds of the cells belong, to cancer cell line UD-SCC-01 has the narrowest distribution from 0% to 15%, unlike the cell line UD-SCC-04 whose distribution extends from 15% to 40% which means that mitochondria volumes of UD-SCC-01 cells are more alike compared to other cancer cell lines.

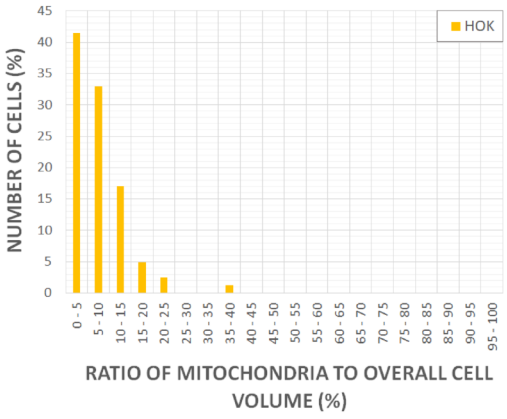

HOK - human oral mucosa

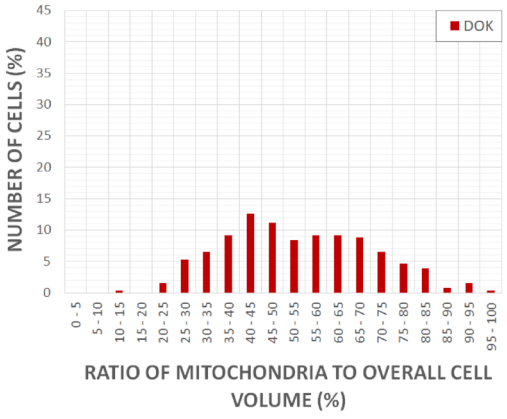

DOK - tongue

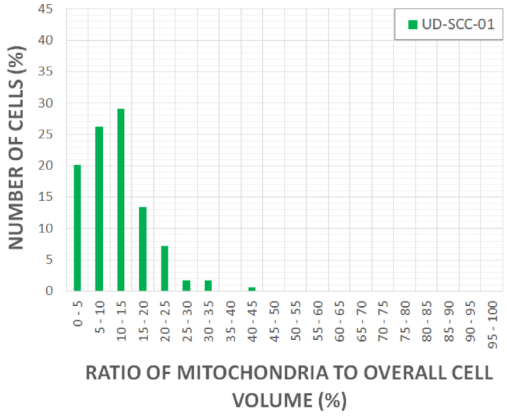

UD-SCC-01 - tonsil

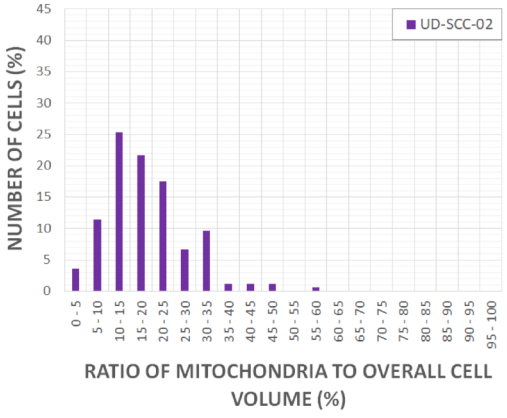

UD-SCC-02 - hypopharynx

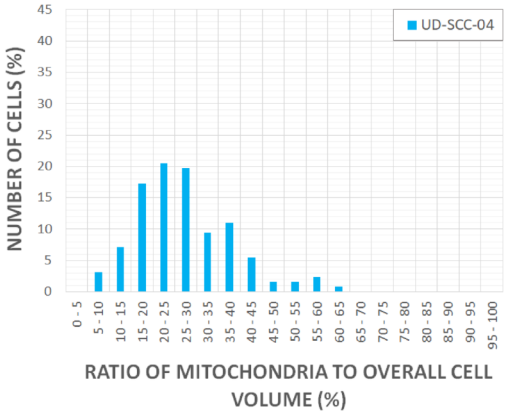

UD-SCC-04 - tongue

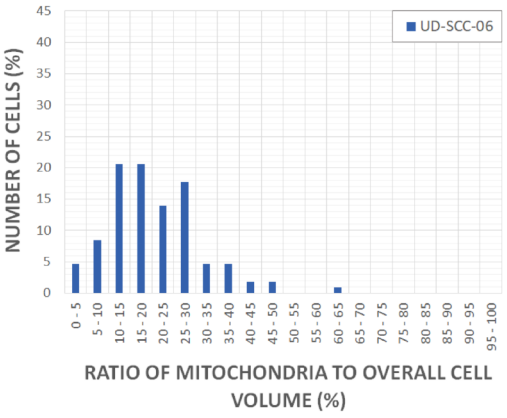

UD-SCC-06 - tongue

Figure 4.10: Distribution of the mitochondria to overall cell volume ratios for all cell line used

Observing images of active mitochondria, volume calculation and distribution, it could not be confirmed that healthy cells contain more active mitochondria than dysplastic or cancer cells. Examining different healthy cell lines, originating from the head and neck area, it could be tested whether this is generally not the case or the leak of mitochondria is characteristic for the HOK cell line.

4.2.5 Remarks

The calculation of different cell organelle volumes enabled the characterization of the cells and a comparison of different cell lines. Nevertheless, the absolute values of the calculated volumes have to be taken with caution.

In cases when the cell organelles of interest have a network structure, like microtubules or actin filaments, those can appear larger in the images than they are in reality due to the relatively low resolution of the microscope. The fluorochromes bind on the single microtubules or actin filaments which are close to each other, but there is still a few nanometres gap between them. As this gap is smaller than the microscope resolution, the neighbouring filaments are not imaged as a network, but as solid. Therefore, the imaged network structures appear to be larger and therewith is the calculated volume of the observed organelle also larger.

As the single actin or microtubules filaments do not differ significantly in-between the cell lines and the cells were stained with the same staining kits, the results gained using this method are comparable. Moreover, as the cytoskeleton network and not single filaments were compared between the cell lines, the results presented in this theses are considered to be relevant.

4.3 Acoustic wave irradiation of the cells

Cancer and dysplastic cells were irradiated with acoustic waves exhibiting frequencies between 0.5 kHz and 10.0 kHz. Their reaction was observed under the confocal fluorescence microscope. Different parameters like frequency and amplitude, irradiation duration or the distance between the cells and probe were varied to find a suitable set of parameters which damage cancer cells the most, or in best case induce a resonance catastrophe. After those parameters had been determined for the cell line UD-SCC-01, the other cancer cell lines and DOK were irradiated to observe whether those cell lines would react differently on the same irradiation parameters. The measurements were made together with students[2] as a part of their Bachelor or Master theses. The author took part in every measurement and made an independent data analysis. As the measurements were repeated to test the reproducibility and increase the accuracy, the results presented in this section are median values of all measurements made.

4.3.1 Characterization of the probe

Before the acoustic wave irradiation of the cells can be made, the probe had to be characterized. As the piezo actuator does not oscillate freely, frequency-dependent

[2]N. Bartels, L. Chai, M. Erinski, L. Fastenrath, S. Krüger, T. Löffler

damping arises. Therefore, different excitation frequencies with an identical input voltage lead to different oscillation amplitudes. To enable the comparison of the cell reaction on different frequencies, all other setup parameters must be kept constant. Therefore, the input voltage has to be determined in a way that the oscillation amplitude is constant for every frequency.

The oscillation amplitude was measured using a microphone. Its output voltage was measured by an oscilloscope as a sine signal. In the first step the maximal input voltage, which results in an sinusoidal output voltage signal without noise or additional fluctuations, was measured for every frequency. Table 4.10 shows the maximal output voltages with the corresponding input voltages for every frequency.

Frequency (kHz)	Input voltage (V)	Output voltage (V)
0.5	6.00	-
1.0	5.50	0.100
1.5	4.60	0.120
2.0	3.10	0.100
2.5	2.30	0.150
3.0	1.95	0.110
3.5	1.48	0.060
4.0	0.79	0.060
4.5	0.75	0.065
5.0	1.50	0.120
5.5	1.50	0.120
6.0	1.30	0.100
6.5	0.89	0.065
7.0	1.30	0.100
7.5	1.20	0.085
8.0	1.05	0.085
8.5	0.95	0.080
9.0	0.95	0.100
9.5	0.95	0.100
10.0	0.85	0.100

Table 4.10: Maximal sinusoidal output voltage and corresponding input voltage for every frequency of interest

The measurement results shown in Table 4.10 are comparable. Nevertheless, as the output voltage values depend also on the measurement system, they should be observed as qualitative. From the results presented in Table 4.10 it can be seen that the minimal output voltage is 0.060 V. In the second step the input voltage was determined for every frequency in a way that the output voltage is 0.060 V. The measured input voltages are shown in Table 4.11. To increase the legibility, those input voltages are designated as 100% from here on.

Frequency (kHz)	Input voltage (V)	Output voltage (V)
0.5	3.60	0.060
1.0	2.40	0.060
1.5	1.90	0.060
2.0	1.64	0.060
2.5	1.37	0.060
3.0	1.06	0.060
3.5	1.35	0.060
4.0	0.80	0.060
4.5	0.70	0.060
5.0	0.80	0.060
5.5	0.90	0.060
6.0	0.90	0.060
6.5	0.80	0.060
7.0	0.72	0.060
7.5	0.65	0.060
8.0	0.65	0.060
8.5	0.65	0.060
9.0	0.62	0.060
9.5	0.57	0.060
10.0	0.52	0.060

Table 4.11: Constant output voltage and corresponding input voltage for every frequency of interest

The presented input voltages were used during the measurements, every time the frequency, the irradiation duration or the probe-cells distance was varied. Those input voltages ensure a constant oscillation amplitude what allows a better comparability of the results.

As the cells are sensitive to temperature fluctuations, which could induce their reactions in form of movement or even cell death, the temperature change during the irradiation of the cells was measured for every frequency of interest and an irradiation time of 15 minutes. The results are shown in Table 4.12.

Frequency (kHz)	Temperature change (K)
0.5	0.9
1.0	0.1
1.5	0.2
2.0	0.5
2.5	0.4
3.0	1.4
3.5	0.9
4.0	0.1
4.5	0.1
5.0	0.5
5.5	0.1
6.0	0.0
6.5	0.6
7.0	0.2
7.5	0.5
8.0	0.4
8.5	0.4
9.0	0.3
9.5	0.3
10.0	0.1

Table 4.12: Temperature change during 15 minutes of acoustic wave irradiation for every frequency

The maximal temperature change of 1.4 K was observed after 15 minutes of irradiation with acoustic waves exhibiting a frequency of 3.0 kHz. However, this change, as well as the other observed, is so small that they do not influence the cells markedly.

4.3.2 Frequency variation

The reaction of the cells on acoustic wave irradiation was observed. The frequency of the acoustic waves was varied from 0.5 kHz to 10.0 kHz in 0.5 kHz steps, keeping the oscillation amplitude, the distance between the probe tip and the cells and the irradiation duration constant. The cells were stained using CellMask Green to highlight their membrane. This staining can reveal possible cell-cell contact breaking or membrane rupture induced by acoustic waves. The frequency variation measurements were made for the cell lines UD-SCC-01 and UD-SCC-04.

Acoustic wave irradiation of UD-SCC-01 cell line

Densely (Petri dish covered for more than 95% with cells) and non-densely (Petri dish covered for less than 90% with cells) populated monolayers of the cell line UD-SCC-01 as well as densely populated monolayer of the cell line UD-SCC-01 with BFP were irradiated with acoustic waves. The acoustic wave frequency was varied and the input voltage was adjusted to achieve a constant oscillation amplitude of the probe (see Subsection 4.3.1). The irradiation duration of 15 minutes and the probe-cells distance of 60 µm were kept constant. The images before and directly after the irradiation were analysed using the software described in Subsection 3.4.3. The main aim of these measurements was to investigate whether the cells react differently on different frequencies and whether the three observed monolayer types react in the same way on the acoustic wave irradiation.
Figure 4.11 shows the images before and after the irradiation of three observed monolayer types with acoustic waves exhibiting a frequency of 10.0 kHz. The red rectangles mark some of the areas where a cell reaction was observed.

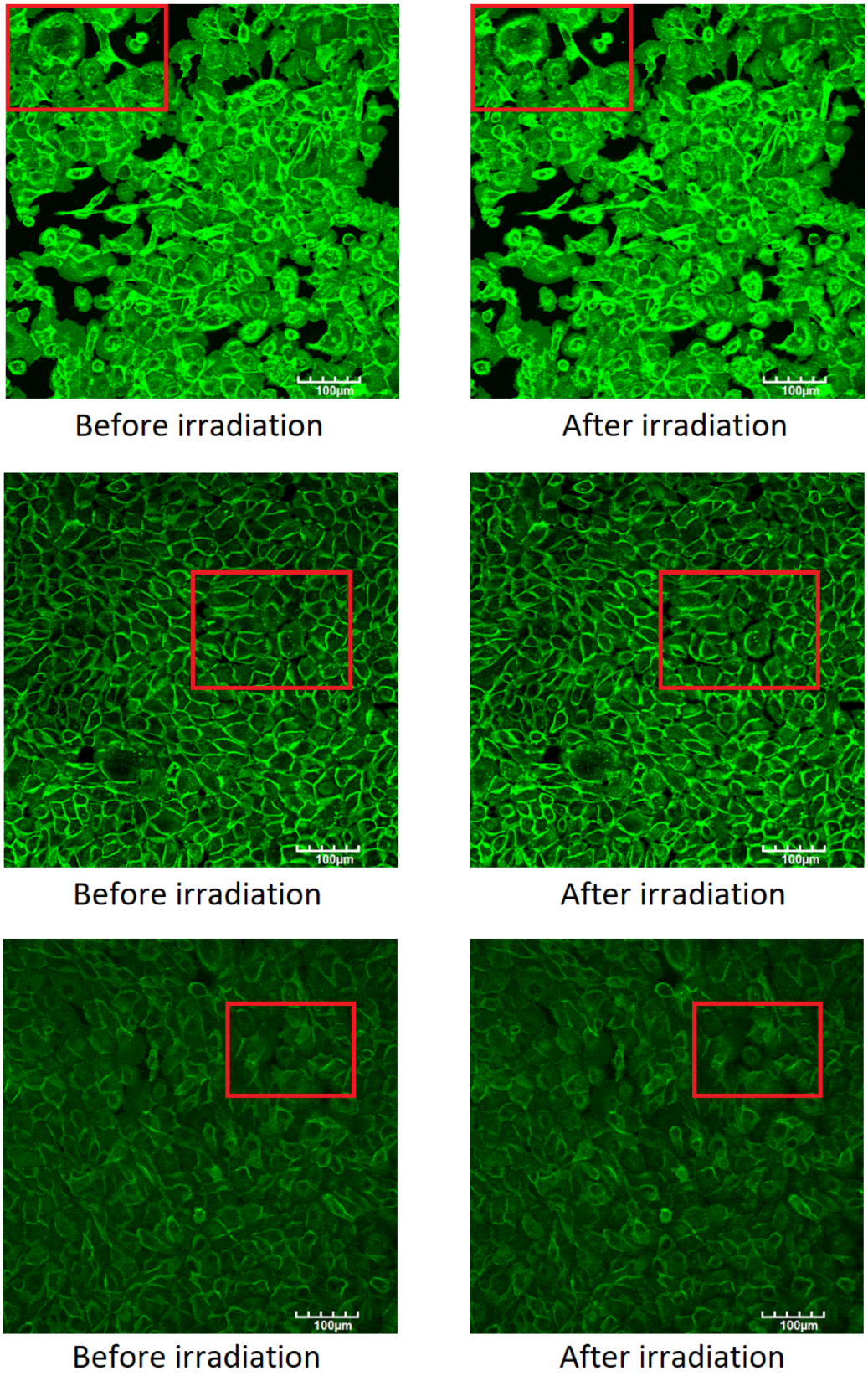

Figure 4.11: Irradiation of the non-densely populated monolayers (up), densely populated monolayers (middle) and cells with BFP (bottom) with acoustic waves exhibiting a frequency of 10.0 kHz

Analysing the images before and after the irradiation of the cells, a great reaction of the cells or cell destruction were not observed. However, it appears that non-densely populated monolayers react stronger than densely populated ones. The reaction of the cells expressing BFP is barely visible.

To better quantify the acoustic wave irradiation induced changes of the cells, the cell reaction, representing the changes of the pixels in the first and the last image, was calculated. Figure 4.12 shows the reaction of the cells for all investigated frequencies. A tabular display of the results is shown in Appendix F.1.

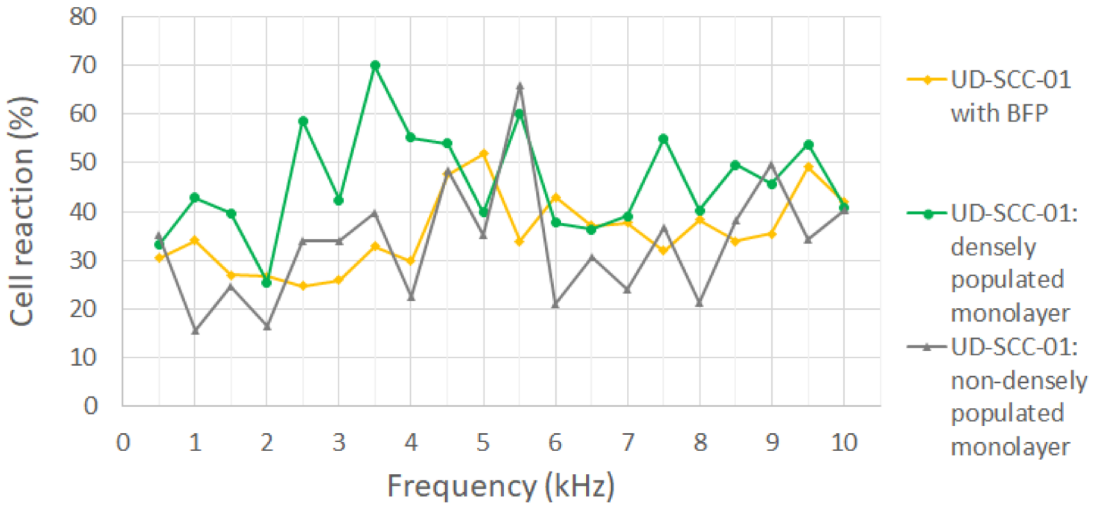

Figure 4.12: Reaction of non-densely and densely populated monolayers as well as densely populated monolayers of cells expressing BFP on acoustic wave irradiation

The three observed monolayer types show different reactions on acoustic wave treatment which is also acoustic wave frequency depended. For example, densely populated monolayers irradiated with a frequency of 2.0 kHz have a reaction of 25% and on 2.5 kHz almost 60%.

Contrary to the image analysis, the calculations prove that the densely populated monolayers show the highest reaction of all monolayer types for about 60% of all observed frequencies whereas the non-densely populated monolayers have a maximal value at 15% of the observed frequencies. The monolayers with cells expressing BFP show the highest reaction on 25% of all observed frequencies. Thus, the densely populated monolayers show markedly more reaction on acoustic wave irradiation compared to other monolayer types.

Cells in a densely populated monolayer have more cell-cell contact than in a non-densely populated monolayer. The reaction of one cell may induce reactions of the neighbouring cells. If on one hand a cell shrinks but the contact to the neighbouring cells does not break, those cells will follow the shrinking cell and their reaction will be observed. On the other hand, if the contact between the cells breaks, this may induce a slight movement of the neighbouring cells from the shrinking cell. This could explain why the densely populated monolayers show more reaction than the non-densely populated ones.

The monolayers of the cells expressing BFP are densely populated, too. The BFP could influence the elasticity of those cells which would explain why two densely populated monolayers of the same cell line react notably different to the same treatment.

The densely populated monolayers show the highest reaction on acoustic waves exhibiting frequencies from 2.5 kHz to 4.5 kHz and 7.5 kHz to 9.5 kHz with one additional peak at a frequency of 5.5 kHz. The reaction on the frequencies below 2.5 kHz is lower than 45% as well as to the frequencies between 6.0 kHz and 7.0 kHz. As there are two frequency ranges where the strongest reaction of the cells was observed, frequencies of those regions should be investigated in the analysis of the influence of other parameters like input voltage or irradiation duration on the reaction of the cells.

Observing the reaction of the non-densely populated monolayer, the cells react the most on the acoustic waves exhibiting frequencies between 4.5 kHz and 5.5 kHz as well as 9.0 kHz. Free regions in these monolayers could have an additional influence as they reveal the glass dish bottom underneath. The waves could reflect on the glass and further influence the measurement results.

The densely populated monolayers expressing BFP have the most distinct regions of maximal reaction on the acoustic waves treatment. The acoustic waves exhibiting frequencies of 4.5 kHz, 5.0 kHz and 9.5 kHz induce the highest reaction of the cells. Even though the reaction of the cells of this monolayer is generally lower compared to the one of the densely populated monolayer without BFP, the regions of maximal reaction are comparable.

After this analysis it can be concluded that the density of the cell monolayer plays an important role. As the densely populated monolayer is more similar to the human body where the density of the cells is high as well and as there is less reflection of the acoustic waves from the bottom, which induces second irradiation of the cells which cannot be measured or influenced, it is recommended to do further experiments with densely populated monolayers. The BFP apparently influences the elasticity of the cells and therefore also the reaction of the cells on the acoustic wave treatment. Nevertheless, the frequencies for which the cells react the most are comparable to the ones of the densely populated monolayer (e.g., 4.5 kHz or 9.5 kHz). Knowing this, and since there are no other viable alternatives, the cells expressing BFP should be used for experiments with co-cultivated cells.

Acoustic wave irradiation of UD-SCC-04 cell line

The reaction of the cell line UD-SCC-04 to acoustic waves exhibiting frequencies between 0.5 kHz and 10.0 kHz was observed as well. Analogously to the experiments with UD-SCC-01 cells, the frequency was varied in steps of 0.5 kHz and the amplitude was kept constant. For all measurements the distance between the probe and the cells was 60 µm and irradiation time 10 minutes. As the analysis of the experiments with the UD-SCC-01 cell line showed that the cell density plays a role in the reaction of the cells, experiments were only made with densely populated monolayers. Figure 4.13 shows the cells before and after the treatment with acoustic waves of 3.5 kHz frequency.

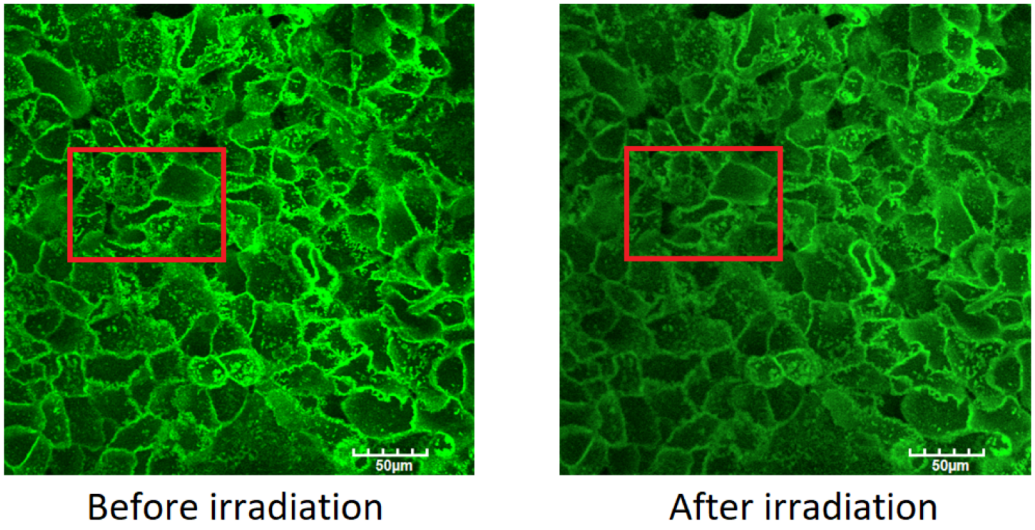

Figure 4.13: Irradiation of cell line UD-SCC-04 with acoustic waves exhibiting a frequency of 3.5 kHz

Comparing the images before and after 10 minutes of acoustic wave irradiation, substantial differences have not been noticed. However, the reaction of some individual cells can be seen. For example, the cell in the middle of the highlighted area shrank during the irradiation and a small reaction of the neighbouring cells occur as well. Nevertheless, the differences before and after the treatment had to be analysed by the software to achieve more precise results. The results of this analysis are shown in Figure 4.14 and in Appendix F.2 in form of a table.

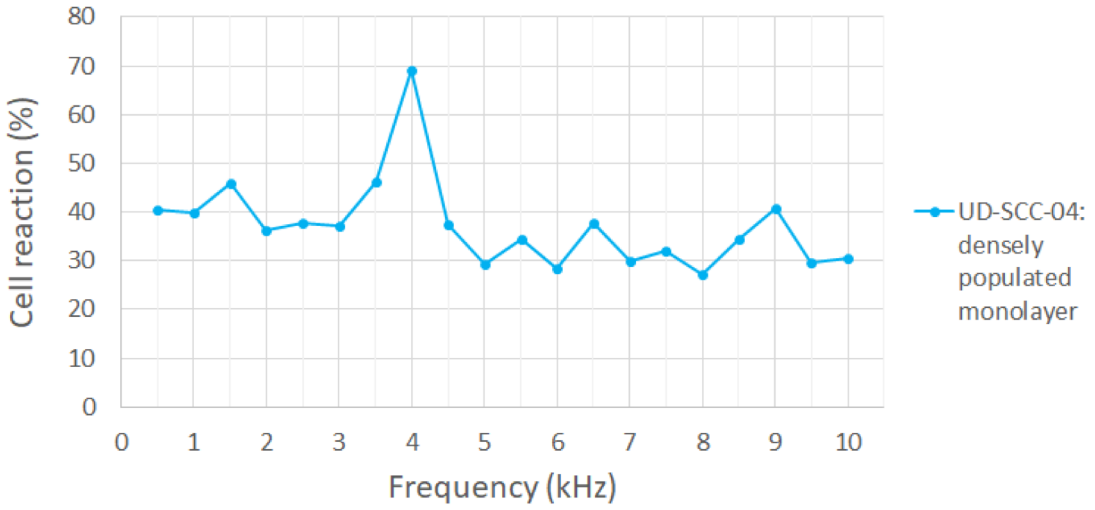

Figure 4.14: Reaction of UD-SCC-04 cell line on the acoustic wave irradiation

The cell line UD-SCC-04 shows a clear maximal value of the cell reaction on

the acoustic wave treatment for acoustic waves exhibiting a frequency of 4.0 kHz. A cell reaction of almost 70% was observed. The reactions on frequencies out of the region between 3.5 kHz and 4.5 kHz are markedly lower with two small peaks at 1.5 kHz and 9.0 kHz. It is clear that the further experiments with the cell line UD-SCC-04 should be made with acoustic waves exhibiting frequencies between 3.5 kHz and 4.5 kHz to observe a maximal reaction of the cells.

Comparison of the cell lines UD-SCC-01 and UD-SCC-04

The last part of the frequency variation deals with the comparison of the reactions of the cell lines UD-SCC-01 and UD-SCC-04 on the acoustic wave treatment. For this purpose the frequency was varied from 0.5 kHz to 10.0 kHz in steps of 0.5 kHz. The amplitude was kept constant as well as the irradiation time of 10 minutes and the probe-cells distance of 60 µm. Figure 4.15 shows the measurement results. The corresponding table can be found in Appendix F.3.

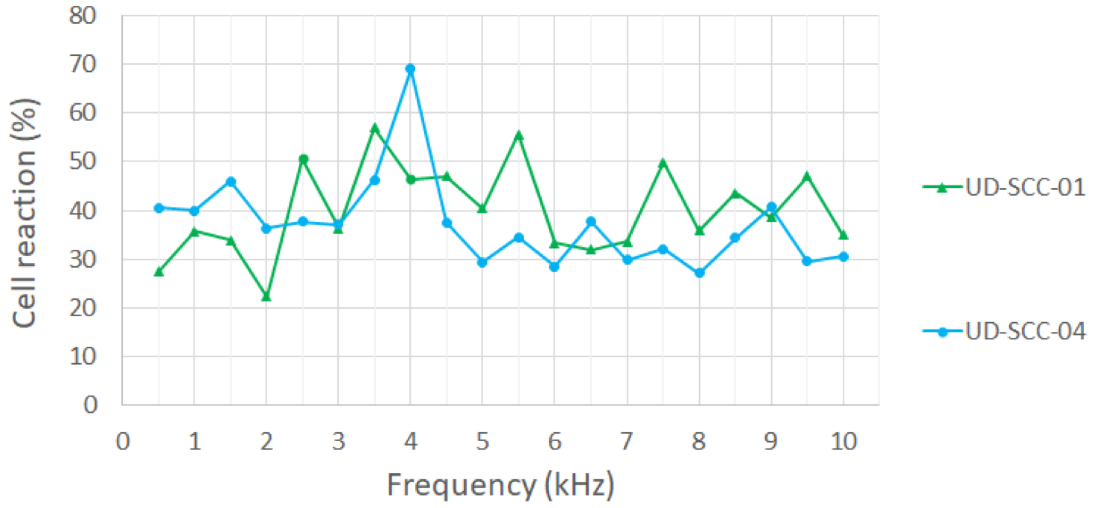

Figure 4.15: Comparison of the cell lines' UD-SCC-01 and UD-SCC-04 reactions on acoustic wave treatment

The cell reaction of UD-SCC-04 has a more pronounced peak compared to the cell line UD-SCC-01 where the determination of the most effective frequency is more complex. Comparing the reactions on acoustic wave irradiation, it is noticeable that the cell line UD-SCC-04 reacts stronger to the frequencies up to 4.0 kHz and the cell line UD-SCC-01 to the frequencies above 4.0 kHz. This can be connected to the cells' elasticity since there is a proportionality between the elastic modulus and the resonance frequency of the cells.

The analysis of the cytoskeleton filaments performed in Subsection 4.2.2 shows that the cell line UD-SCC-01, with an average actin filament volume of 48% ± 10% and 55% ± 12% average of microtubules, contain more cytoskeleton filaments compared to the cell line UD-SCC-04 (44% ± 10% microtubules and 31% ± 7% actin filaments). The increased cytoskeleton volumes of the cell line UD-SCC-01

may lead to an increased elastic modulus of its cells. As the elasticity of the cells is mainly determined by the cytoskeleton and the elastic modulus is proportional to the resonance frequency, differences in cytoskeleton filament volumes could be a reason for the different reactions of these two cell lines on the acoustic wave treatment.

4.3.3 Variation of irradiation duration

To observe whether the irradiation duration influences the cells' changes, the reaction of the cell line UD-SCC-01 on the acoustic wave treatment was observed after 5, 10 and 15 minutes of irradiation for the waves exhibiting frequencies from 0.5 kHz to 10.0 kHz. The cell line UD-SCC-04 was irradiated with acoustic waves exhibiting the same frequencies. The reaction of this cell line was observed after 5 and 10 minutes of treatment. As the cells are living organisms which move, grow and change during the cell cycle, imaging of the cells without irradiation was made to monitor natural changes of the cells. This enables a better analysis and evaluation of the measurements of acoustic wave irradiation.

Variation of irradiation duration for the UD-SCC-01 cell line

The reaction of the densely populated monolayer on acoustic wave irradiation was observed after 5, 10 and 15 minutes. The distance between probe and cells was kept constant at 60 µm. Figure 4.16 shows the comparison of the observed irradiation times for the different frequencies. Results in form of a table can be found in Appendix G.1.

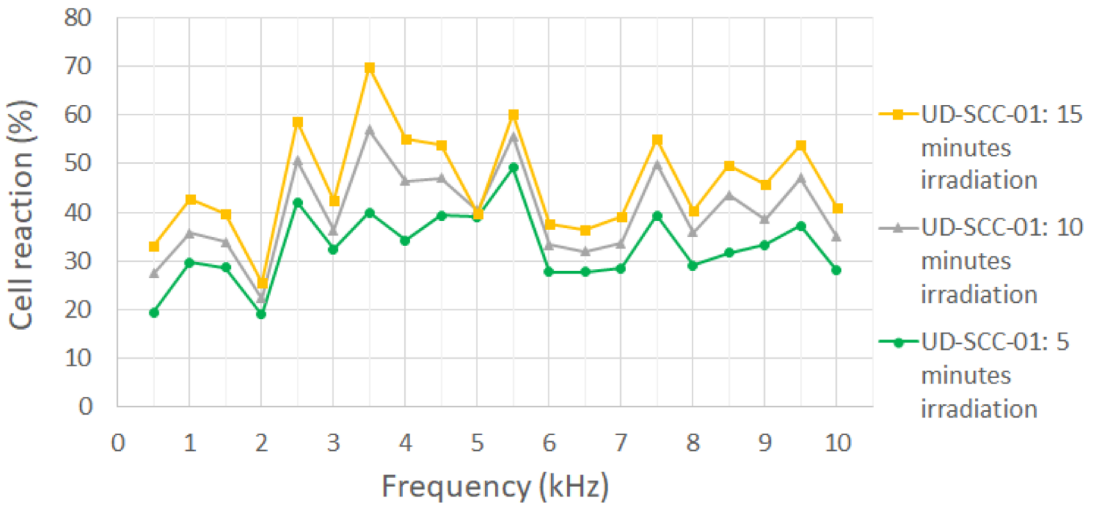

Figure 4.16: Variation of irradiation duration for 5, 10 and 15 minutes

Considering the curves of the different irradiation times, a clear correlation between the irradiation time and the cell reaction can be seen. The reaction of the cells was, as expected, highest for 15 minutes irradiation time and lowest for the

5 minutes treatment. The cell reaction during the first 5 minutes of irradiation is the largest one. When the irradiation was extended for further 5 minutes the change rate decreased. Increasing the irradiation time to 15 minutes, a further decrease of the rate of change was observed. This leads to the conclusion that the cells show a qualitative reaction on the frequency and quantitative reaction on the time.

The cell behaviour during 15 minutes without radiation was observed. A linear correlation between the observation time and the cell change was found. Thus, the ratio of irradiation induced change to natural change is maximal for shorter time periods. Therefore, the irradiation time of 5 minutes was chosen for further investigations. Another benefit of a shorter irradiation duration is the reduction of outside influences on the cells during the time-laps imaging (see Subsection 2.3.4).

Variation of irradiation duration for the UD-SCC-04 cell line

Densely populated monolayers of the cell line UD-SCC-04 were irradiated for 5 and 10 minutes. The reaction of the cells on the irradiation using acoustic waves exhibiting frequencies between 0.5 kHz to 10.0 kHz was observed. The input voltage of 100% and the distance between probe tip and cells (60 µm) were kept constant. The measurement results are shown in Figure 4.17. A tabular display of the results can be found in Appendix G.2.

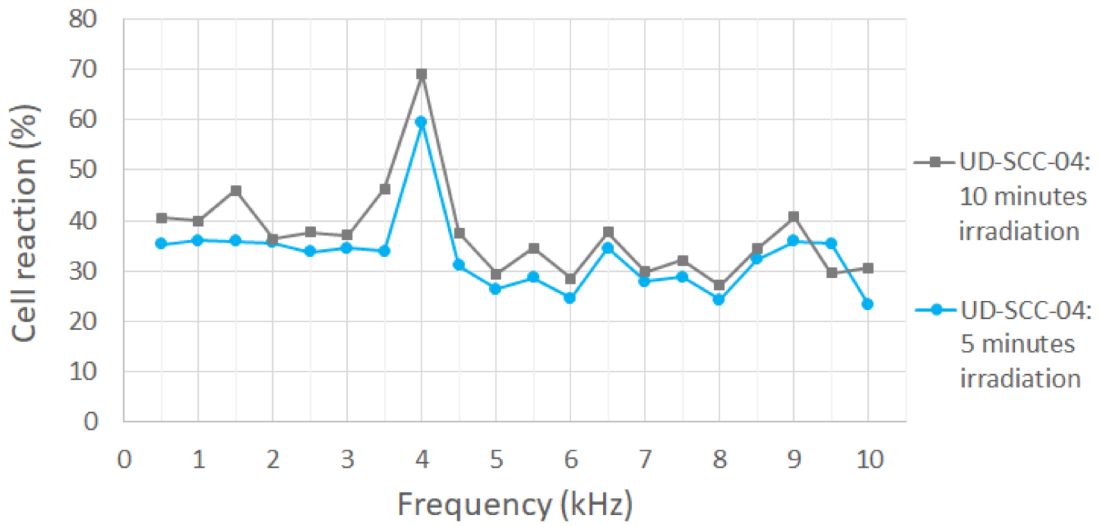

Figure 4.17: Variation of irradiation duration for 5 and 10 minutes

A correlation between the irradiation duration and the cell reaction is noticeable for the cell line UD-SCC-04, too. The cells reacted stronger on the acoustic wave treatment of 10 minutes than on 5 minutes irradiation. Nevertheless, after 5 minutes of irradiation with acoustic waves exhibiting a frequency of 9.5 kHz, the reaction of the cells was greater compared to the reaction on 10 minutes irradiation using the same parameter.

Time-laps imaging of the UD-SCC-04 cells was made without irradiation to observe their natural behaviour. Again, a linear proportionality between the increase of the cell change and the increase of the observation time was found. Thus, the irradiation time of 5 minutes is recommended for further analysis of the cell line UD-SCC-04 as well.

4.3.4 Input voltage variation

After the reaction of the cells on different frequencies and irradiation times was observed and analysed, the measurements of input voltage variation were made. The variation of input voltage, output voltage, and the probe's oscillation amplitude could affect the cell's response. The output voltage used during the measurements with frequency variation was set as 100%. To keep the output voltage constant for the measurements with different frequencies, the input voltage had to be adjusted for every frequency anew. Mr. Tobias Löffler measured which input voltage had to be used for every frequency step. As a result, the output voltage could be adjusted from 0% to maximal 150% in steps of 25%. Those measurement results are used for input voltage variation and are shown in Appendix H.1.

The measurement results of frequency variation showed at which frequencies or frequency ranges the cells reacted the most. Those were used to observe the influence of different input voltages on the cells. For irradiation of the cell line UD-SCC-01 the acoustic waves exhibiting frequencies of 2.5 kHz, 7.5 kHz and 9.0 kHz were used. Those frequencies were chosen from the region where the cell reaction was the greatest and at which the input voltage could be increased for at least 25%.

As for the cell line UD-SCC-04 the markedly higher reaction was observed at 4.0 kHz comparing to the reactions on other frequencies, the frequencies of 3.5 kHz, 4.0 kHz and 4.5 kHz were chosen for further investigation. Due to the technical limits of the experimental setup, the input voltage for those frequencies could only be decreased. The input voltages used are shown in Appendix H.2.

Because the measurements of the irradiation duration variation had shown that the ratio of the cell reaction induced by acoustic waves to natural reaction decreases with increased irradiation time, an irradiation time of 5 minutes was chosen for the input voltage variation measurements.

Input voltage variation for the UD-SCC-01 cell line

As already discussed, the input voltage was varied for the frequencies of 2.5 kHz, 7.5 kHz and 9.0 kHz. For the frequency of 2.5 kHz the input voltage was varied from 25% to 150% in steps of 25%. Due to limitations of the experimental setup, the input voltage for the frequencies of 7.5 kHz and 9.0 kHz was increased up to 125%. The cell reaction on the input voltage variation for the frequencies of interest is shown in Figure 4.18 with corresponding table in Appendix H.3.

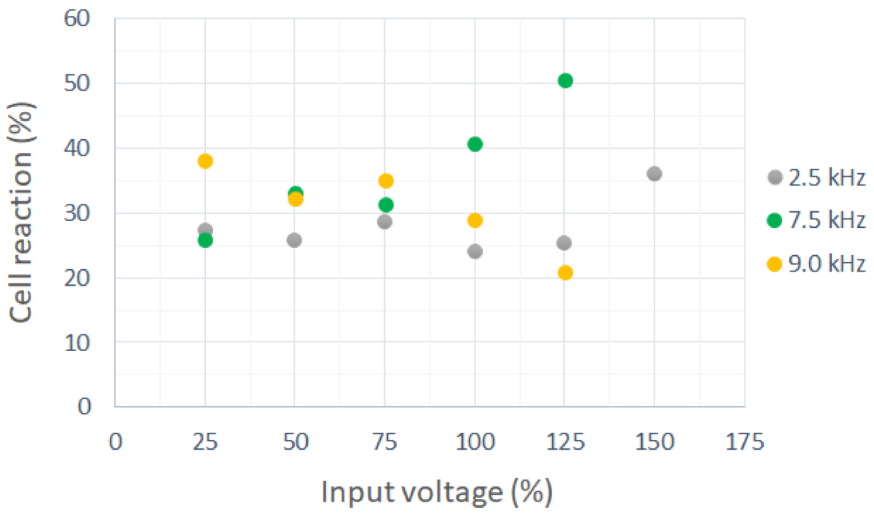

Figure 4.18: Influence of the input voltage variation on the cell reaction for cell line UD-SCC-01

Analysing the cell reaction on the input voltage variation, it is noticeable that the reaction of the cells increases with the increase of the input voltage for the frequency of 7.5 kHz. For the frequency of 9.0 kHz the reaction of the cells decreases with increased input voltage. This result implies that the input voltage, and thereby the oscillation amplitude, is too high and the cell deformation is not anymore linear-elastic, but linear-viscoelastic. Observing the variation of the input voltage for the frequency of 2.5 kHz, the reaction of the cells increases with increased input voltage. Even though the input voltage maximum is the highest for the frequency of 2.5 kHz, the maximal cell reaction is achieved for the frequency of 7.5 kHz and input voltage of 125% with a value of 51%. As the reaction of the cells is substantially higher for the frequency of 7.5 kHz and 125% of input voltage, this parameter combination is recommended for the further analysis of the cell reaction on acoustic wave treatment.

Input voltage variation for the UD-SCC-04 cell line

Observing the reaction of UD-SCC-04 cells on the irradiation with acoustic waves exhibiting frequencies from 0.5 kHz to 10.0 kHz, the cells showed the strongest reaction at 4.0 kHz. Therefore, the frequency range from 3.5 kHz to 4.5 kHz was used to investigate the influence of the input voltage on the cells. Due to restrictions in the experimental setup, the input voltage for the frequencies of interest were varied in a range from 25% to 100% in steps of 25%. The measurement results are shown in Figure 4.19 and in form of a table in Appendix H.4.

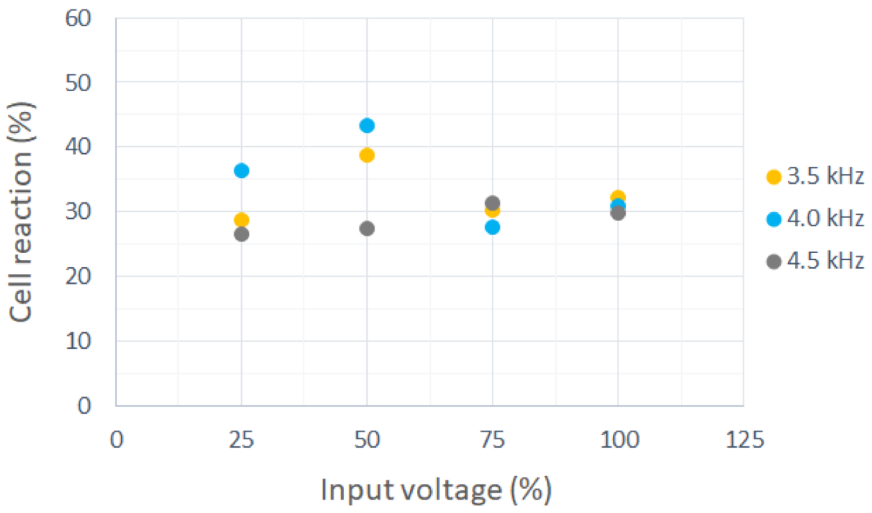

Figure 4.19: Influence of the input voltage variation on the cell reaction for cell line UD-SCC-04

Increasing the input voltage from 25% to 50% for the frequencies of 3.5 kHz and 4.0 kHz results in a notable increase of the cell reaction. At a further increase of the input voltage the cell reaction decreased markedly. A reason for this could be, as discussed during the UD-SCC-01 cell line observation, that the input power induces linear-viscoelastic deformation of the cells instead of linear elastic deformation. The change of the cell reaction on the input voltage variation for the frequency of 4.5 kHz is within 5%. Thus, the input voltage variation for the frequency of 4.5 kHz induces just a slight change of the cell reaction. Notable is that the reaction of the cells on the input voltages of 75% and 100% does not differ substantially for all the observed frequencies.

The frequency of 4.0 kHz is close to the resonance frequency of parts of the experimental setup, what occasionally caused a vibration of the system and was noticeable in the images as vertical lines. In cases when the vibrations occurred, the measurements were interrupted and not taken into analysis. To avoid issues with the experimental setup, the frequency of 3.5 kHz with an input voltage of 50% is recommended for further analysis of UD-SCC-04 cell line. In case of a setup change, the frequency of 4.0 kHz with input voltage of 50% can be used as well.

4.3.5 Probe-cells distance variation

The distance between the probe tip and the cells was varied to investigate whether this parameter influences the cell reaction during acoustic wave irradiation. The intensity of the waves decreases with the distance. Therefore, it would be expected that the shortest distance between the probe and the cells induces the greatest reaction of the cells.

As discussed in Subsection 4.2.1 UD-SCC-04 tends to grow more chaotic and in islands. Moreover, cells are overlapping at random which cannot be influenced. Therefore, the distance the between probe's tip and the cells differs markedly, depending on the height of the island. Thus, investigating the influence of the

distance between the probe and the cells on the cell reaction is not meaningful for cell line UD-SCC-04. This parameter was tested using the cell line UD-SCC-01 as those cells grow more homogeneously and have a more uniform height profile.

To test the influence of the distance between the probe and the cells on the cell reaction, the tip of the probe was set 40 µm, 60 µm, 80 µm and 100 µm above the cell bottom. For this investigation acoustic frequencies of 2.5 kHz, 7.5 kHz and 9.0 kHz were used with an input voltage of 100% for every frequency. The reaction of the cells was observed before and after 5 minutes of irradiation. Measurement results are shown in Figure 4.20. A tabular display of measurement results is given in Appendix I.1.

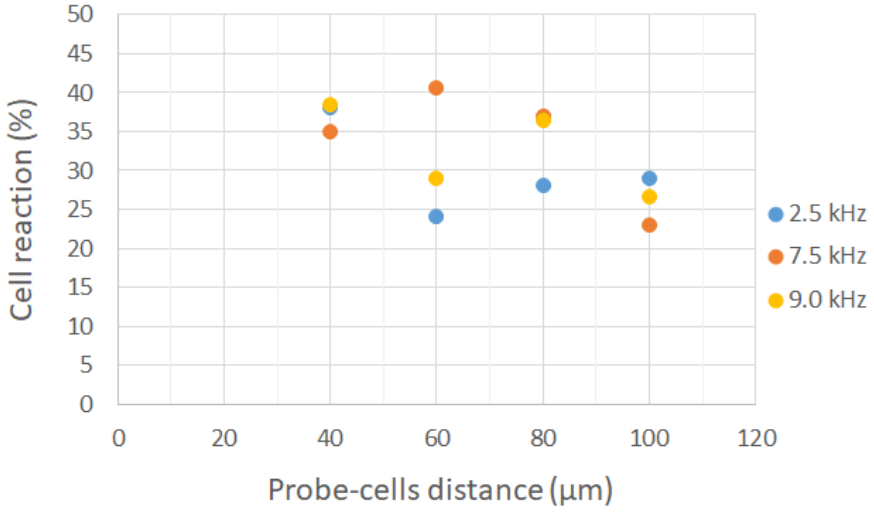

Figure 4.20: Influence of the probe-cells distance on the cell reaction for cell line UD-SCC-01

The reaction of the cells on the acoustic wave treatment when the probe-cell distance was set to 100 µm is under 30% for all observed frequencies. Furthermore, the reaction of the cells on a treatment with acoustic waves exhibiting frequencies of 7.5 kHz and 9.0 kHz was the lowest observed for this probe-cells distance. The minimal reaction on the frequency of 2.5 kHz was observed at the probe-cells distance of 60 µm. For this distance as well as for 80 µm the reaction of the cells differs markedly for different frequencies. This is less notable for the distance of 100 µm, and the least at 40 µm.

When the probe was set to 40 µm above the cell bottom, the cell reaction was over 35% for all observed frequencies and maximal for all distances for the frequencies of 2.5 kHz and 9.0 kHz. The highest reaction of the cells for the shortest distance between the probe and the cells may be explained with the fact that the intensity of the acoustic waves decreases with the distance. When the probe-cells distance is larger than 40 µm, e.g., 100 µm, the intensity of the acoustic waves is lower when the waves reach the cells and therefore they can influence the cells less than when the distance is 40 µm. This is also shown by experimental data, i.e., the reaction of the cells is above 35% for the distance of 40 µm and below 30% for the distance of 100 µm.

Even though the cell reaction for the distance of 40 µm and the frequency of 7.5 kHz was not maximal as it was the case for 2.5 kHz and 9.0 kHz, this distance was chosen for further analysis due to constant and high cell reactions for all observed frequencies.

4.3.6 Irradiation of cancer and dysplastic cells

Acoustic wave irradiation of the cells has not induced a resonance catastrophe and destroyed the cells. Nevertheless, the cells reacted differently on the acoustic waves exhibiting different frequencies. The other parameters like input voltage or radiation duration had an influence on the cell reaction as well. Based on the measurement results, a set of parameters with a frequency of 7.5 kHz, 5 minutes irradiation time, input voltage of 125% and probe-cells distance of 40 µm was found, for which the cell line UD-SCC-01 showed the strongest reaction. This parameter set was therefore used for acoustic wave irradiation of the dysplastic and all cancer cell lines to investigate whether different cell lines react differently on the same irradiation parameters. If this would be the case, the acoustic wave treatment would have to be personalized for each patient.

The HOK cells do not adhere to the culture dish as much as other cells do and can be easily detached, e.g., during medium pipetting. When the acoustic wave are applied, the cells are detaching and are not shown on the images anymore. The analysis software recognizes this as cell reaction what leads to false results. Thus, this cell line was not used during this investigation.

Densely and non-densely populated monolayers of the observed cell lines were irradiated with acoustic waves exhibiting a frequency of 7.5 kHz for 5 minutes with an input voltage of 125% and a probe-cells distance of 40 µm.

Irradiation of a densely populated monolayer

For the completeness of the results densely populated monolayers of all cancer cell lines and DOK were exposed to acoustic waves. However, the results gained through irradiation of the cell lines UD-SCC-04 and UD-SCC-06 have to be taken with caution. As already discussed in Subsection 4.2.1, those cell lines tend to overlap and grow in islands what leads to an increased height profile compared to the other cell lines. The measured height profiles of the cell lines UD-SCC-01 and UD-SCC-04 differed up to 60% from each other. As the probe-cells distance was measured from the bottom of the cells, large differences in the height profile cause notably different distances between the probe and the cells. As discussed in Subsection 4.3.5, the probe-cells distance is an important parameter of the setup and influences the measurement results. Therefore, substantially different height profiles of the cells cause a variation in the probe-cells distance what leads to incomparable results.

Additionally, when the overlapping cells are irradiated, the movement of one cell induces the movement of the neighbouring cells in all three dimensions. During irradiation of the cells growing in a monolayer, a movement of one cell does not have to induce the motion of neighbouring cells, and if it happens, the cells' motion is just in x-y-direction. Therefore, the reaction of the cells on neighbouring cells is considerably lower compared to cells growing in islands.

Due to the observed problems, the comparison of the cell reaction on acoustic wave irradiation was made just for DOK, UD-SCC-01 and UD-SCC-02. Images before and after the irradiation of those three cell lines are shown in Figure 4.21.

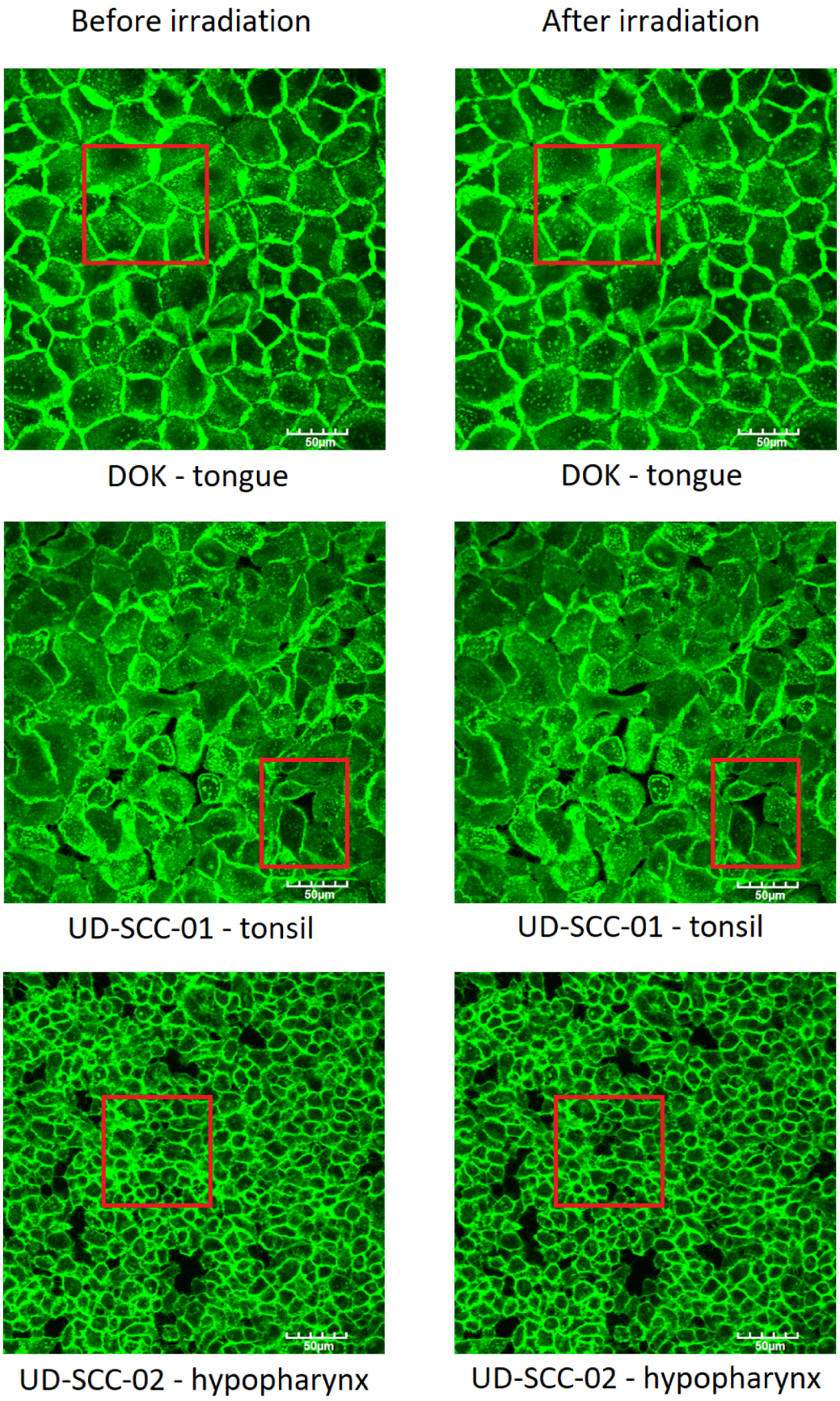

Figure 4.21: Images before and after irradiation of dysplastic and cancer cell lines

Analysing the images before and after the acoustic wave irradiation, notable cell changes have not been observed. Nonetheless, reactions of individual cells were noticed and some are highlighted in Figure 4.21. The changes of the DOK cells appear to be the smallest while the cell line UD-SCC-02 shows the strongest reaction after 5 minutes treatment. For a more accurate comparison of the cell lines, the images before and after the treatment were analysed using the software.

The results, including all cancer and dysplastic cell lines, are shown in Figure 4.22. A corresponding table presenting the results can be found in Appendix J.1.

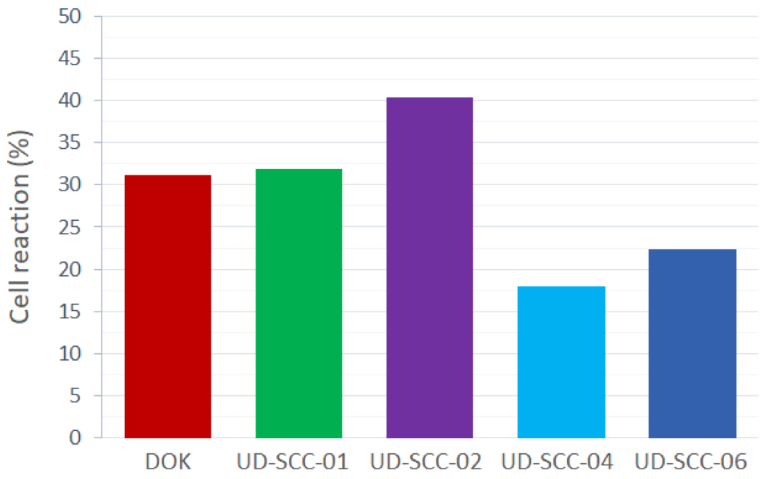

Figure 4.22: Cell reaction of dysplastic and cancer cell lines on acoustic wave irradiation

As the image analysis indicates, the cell line UD-SCC-02 shows the most reaction on the acoustic wave irradiation. The cell lines DOK and UD-SCC-01 show a similar reaction on the irradiation using the same parameters. Observing the volumes of the cytoskeleton filaments discussed in Subsection 4.2.2, it can be noticed that DOK and UD-SCC-01 cells have more similar cytoskeleton filament volumes which are also higher compared to UD-SCC-02 cells. This is particularly evident in actin filament volumes where the cell lines DOK and UD-SCC-01 have an over 50% greater actin filament volume. As the cytoskeleton, especially actin filaments, influence the elasticity of the cells the most, a lack of actin filaments could lead to a lower elastic modulus of the cell line UD-SCC-02. Considering the proportionality between the elastic modulus and the resonance frequency, a lower elastic modulus means a lower resonance frequency of the cells.

When the cells are irradiated with acoustic frequencies close to their resonance frequency they oscillate more and their reaction is stronger than to other frequencies. Thus, the difference in the amount of cytoskeleton filaments between the cell lines could explain the different reaction of their cells. As the cell line UD-SCC-02 contains less cytoskeleton filaments and if it is to be assumed that its elasticity is therefore lower, the higher reaction on the acoustic wave irradiation would indicate that the resonance frequency of the cell line UD-SCC-02 is closer to 7.5 kHz than the ones of the cell lines DOK and UD-SCC-01.

The differences in the reaction of the cell lines to the acoustic waves treatment indicates that the acoustic wave therapy will have to be personalized and the irradiation parameters will have to be adjusted for every patient individually.

Irradiation of a non-densely populated monolayer

Non-densely populated monolayers, where less than 50% of the Petri dish was covered with cells, were irradiated with acoustic waves. DOK and all cancer cell lines were irradiated using the parameter set with a frequency of 7.5 kHz, 5 minutes irradiation time, input voltage of 125% and probe-cells distance of 40 µm.

During the acoustic wave irradiation a problem of cells detaching from the bottom occurred. As shown in Figure 4.23, the cells on the marked position detached from the bottom and cannot be seen in the image after the irradiation. The UD-SCC-02 cells with less contact to neighbouring cells obviously adhere less to the bottom and can be easily detached by acoustic waves. In case of UD-SCC-04 and UD-SCC-06 cell lines, whose cells grow in islands this problem occurred as the whole island is attached to the bottom with just a few cells. There are much more cells in the island above the adherent cells which are then moved by the acoustic waves. Due to a greater mass and the low attachment surface, acoustic waves can easily detach those cell islands from the bottom.

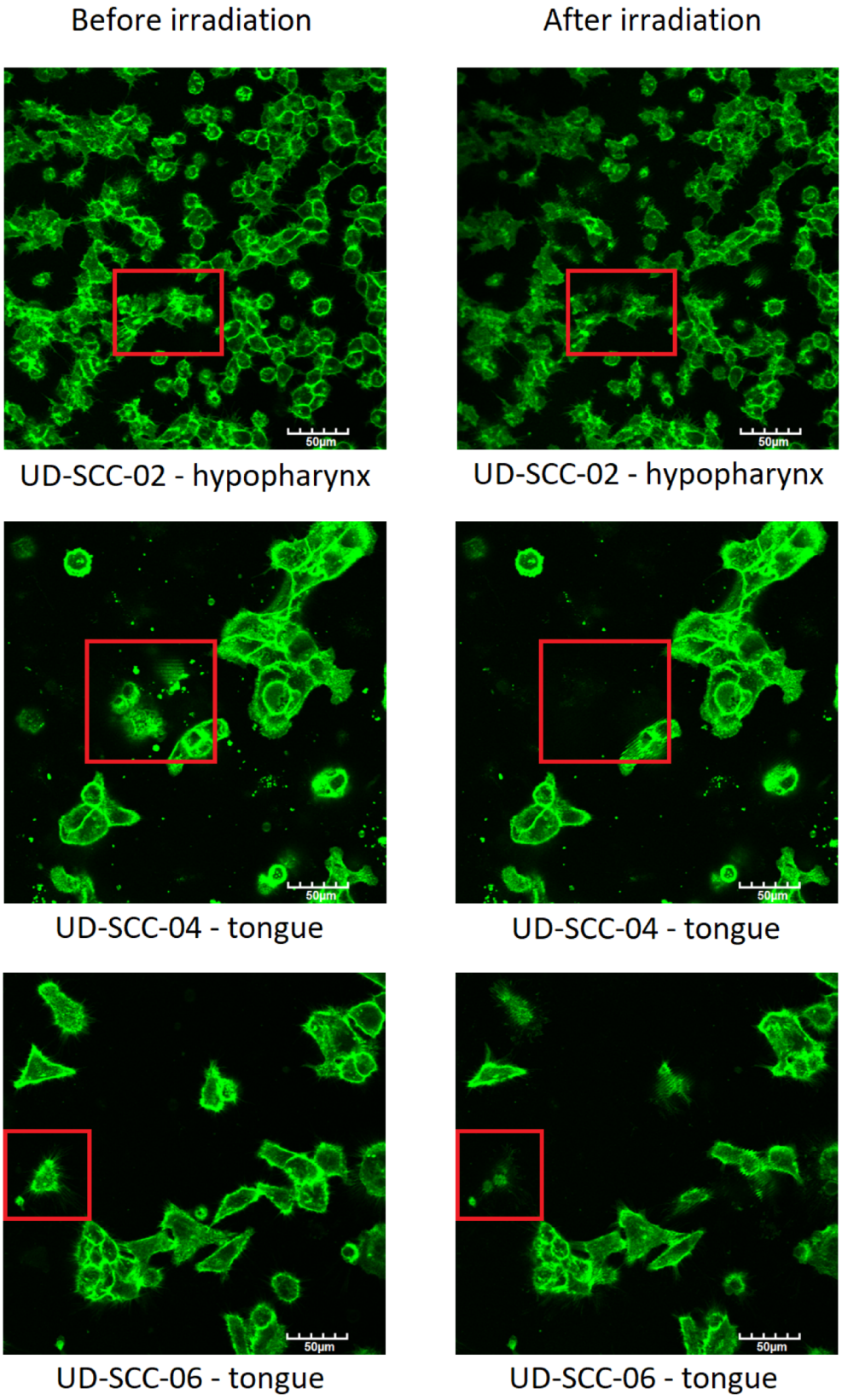

Figure 4.23: Detached cells of cell lines UD-SCC-02, UD-SCC-04 and UD-SCC-06 after acoustic wave irradiation

Because of the described problem, only the cell lines DOK and UD-SCC-01 were compared. However, for the completeness of the results, the reaction of the other cell lines on the acoustic wave irradiation was calculated as well. Those measurement results are shown in Figure 4.24 with a tabular display in Appendix J.2.

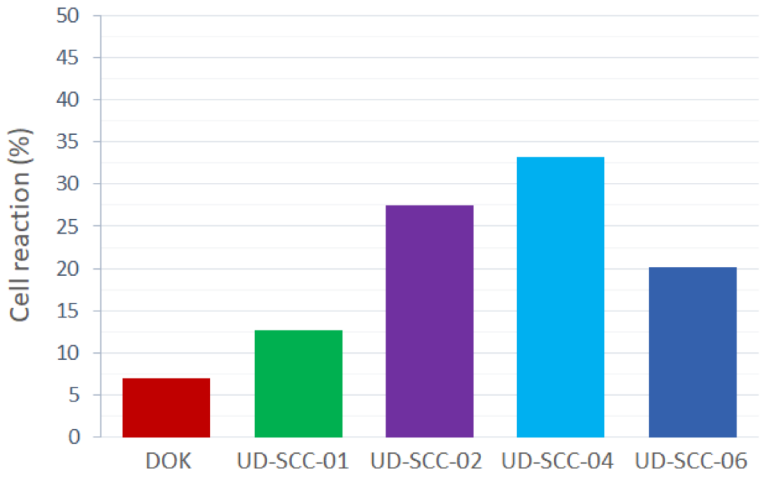

Figure 4.24: Cell reaction of non-densely populated monolayer of dysplastic and cancer cell lines on acoustic wave irradiation

While analysing the cell reaction of non-densely populated monolayers it can be seen that the cell lines UD-SCC-02 and UD-SCC-04 have a substantially stronger reaction on the acoustic wave treatment compared to DOK or UD-SCC-01 cells. The reaction of the cell line UD-SCC-06 is stronger as well. This can be explained with the above mentioned problem that occurred during the irradiation. As the cells were visible in the image before the irradiation and then detached and had vanished in the image after the irradiation (see Figure 4.23), the evaluation software recognized this as a change. Therefore, evaluation results for the cell lines UD-SCC-02, UD-SCC-04 and UD-SCC-06 are not meaningful and should not be taken into comparison with the other observed cell lines.

The reactions of the non-densely populated monolayer of the cell lines DOK and UD-SCC-01 are lower than the densely populated monolayers of both cell lines. As the cells in a densely populated monolayer have more cell-cell contact, the reaction of one cell on the acoustic wave treatment induces the movement of the neighbouring cells which is, later on, observed as a cell reaction. This is not the case when individual or less dense cells with almost no cell-cell contact are observed. As it is not possible to subtract the cell reaction on the neighbouring cells from the cell reaction on acoustic waves, the reaction of the non-densely populated monolayer appears to be lower.

Non-densely populated monolayers of the cell line UD-SCC-01 react more to the acoustic wave treatment than the DOK monolayers. The difference between the non-densely populated monolayers of DOK and UD-SCC-01 cells is higher than the differences between the densely populated monolayers of both cell lines. The reason for this could be that UD-SCC-01 cells, with less cell-cell contact, have a lower elastic modulus than the cells with more cell-cell contact in a densely

populated monolayer. The lower elastic modulus leads to a stronger reaction of the cells on the acoustic wave treatment using the frequency of 7.5 kHz.

Summary of cancer and dysplastic cells irradiation

The irradiation of the densely populated monolayers showed that different cell lines react differently to the same irradiation parameters. This indicates that the elasticity of the observed cell lines differs, what would be in accordance with the morphology analysis and the differences found during the cytoskeleton filament evaluation. The different cell reaction on the same irradiation parameter set leads to the conclusion that a future therapy will have to be adjusted for every patient individually.

Problems occurred during the irradiation of non-densely populated monolayers which could be challenging for the development of a new cancer therapy. The cells which do not adhere well on the bottom of the Petri dish were detached and could freely move through the dish. Inside a human body, detachment has to be avoided under all circumstances.

Comparing the reaction of densely and non-densely populated monolayers it can be seen that the cells react differently when they have more neighbouring cells. This indicates that the elasticity of the individual cells and the cells in a monolayer differ. If that is the case, future experiments have to be made on densely populated monolayers or even on a 3D cell culture to have a better comparison to in vivo tumors.

4.3.7 Irradiation of co-cultivated cells

The co-cultivation of two different cell lines enables simultaneous irradiation of their cells. In this way, a simulation of an in vivo tumor, where different tumor and healthy cells grow next to each other, can be made. To distinguish between the cell lines, the cell line UD-SCC-01 expressing BFP was used (see Subsection 3.1.1). First it was tested whether the UD-SCC-01 cells expressing BFP react on the acoustic wave irradiation in the same way as the UD-SCC-01 cells without BFP. In a second step, UD-SCC-01 cells were co-cultivated with DOK cells. The cells were 5 minutes irradiated with acoustic waves exhibiting a frequency of 7.5 kHz with an input voltage of 125% and a probe-cells distance of 40 µm.

Because the software used for the previous analysis of the images before and after the irradiation cannot distinguish between two cell types or individual cells, the images were analysed using the software developed for the morphology measurement. Segmentation masks were made and the software calculated the area of the single cells in the image before irradiation. The image after irradiation was then analysed and the area of the single cells was calculated. Knowing the area before and after the irradiation, the expansion of the cells caused by acoustic wave irradiation was calculated. As the software numbers all the cells, comparing the numbered image with the fluorescence microscopy images it was easy to determine which cells were expressing BFP and which were not. Because the software has to distinguish between individual cells the non-densely populated monolayer was observed to simplify the segmentation and analysis.

Co-cultivation of UD-SCC-01 cells together with UD-SCC-01 cells expressing BFP

Cells of the cell line UD-SCC-01 with and without BFP were co-cultivated and simultaneously irradiated to observe whether the BFP would influence the cell elasticity or reaction on irradiation. Figure 4.25 shows the image before and after the irradiation of the cells.

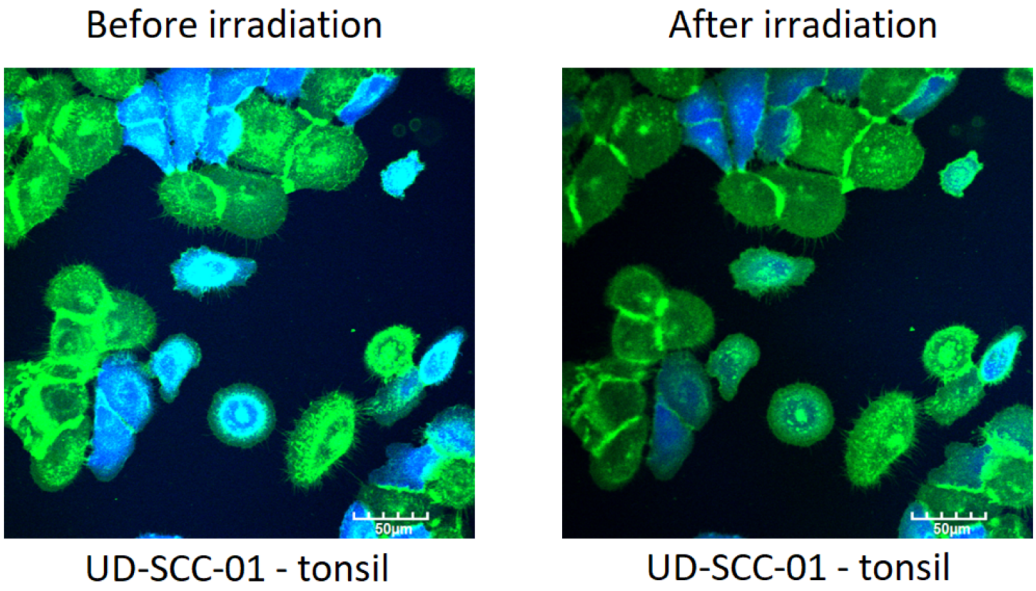

Figure 4.25: Cell reaction of UD-SCC-01 cells with BFP (blue) and without BFP on acoustic wave irradiation

Observing the images before and after the irradiation only minor differences between cells expressing BFP and the cells without BFP were noticeable. Nevertheless, a software evaluation was made to quantify the reaction of both cell types. The results are shown in Table 4.13.

	UD-SCC-01	UD-SCC-01 expressing BFP
Number of cells	19	20
Average (%)	−5	−4
Median (%)	−5	−5
Maximum (%)	5	0
Minimum (%)	−17	−10

Table 4.13: Cell area expansion of the UD-SCC-01 cells with and without BFP caused by acoustic wave irradiation

The average values of the cell area expansion are very similar for the UD-SCC-01 cells with and without BFP. However, the maximum and minimum ranges differ slightly. The cell line UD-SCC-01 without BFP shows a maximal cell expansion

of 5% which could be explained by the fact that the acoustic waves pressed the cell and changed its shape. This may have been recognized as larger cell area at the cell bottom where the images were taken. The minimal expansion of -17% may be the result of cell shrinking as a reaction on the acoustic wave treatment. The range between maximal and minimal cell expansion of the UD-SCC-01 cells expressing BFP is from 0% to -10%. The differences in the range of cell expansion may indicate that the BFP may influence the elasticity of the cells and therefore the reaction on acoustic wave irradiation. Nevertheless, as the measurements were carried out exemplarily and on a small sample, this results must be taken with caution and further measurements are recommended. Due to lack of alternatives, the cells expressing BFP were used during further co-cultivation measurements and analysis.

Co-cultivation of DOK and UD-SCC-01 cells

Co-cultivation of DOK and UD-SCC-01 cells expressing BFP was made exemplarily to simulate the in vivo situation and to observe the reaction of the cells on acoustic wave irradiation. The images before and after the irradiation are shown in Figure 4.26.

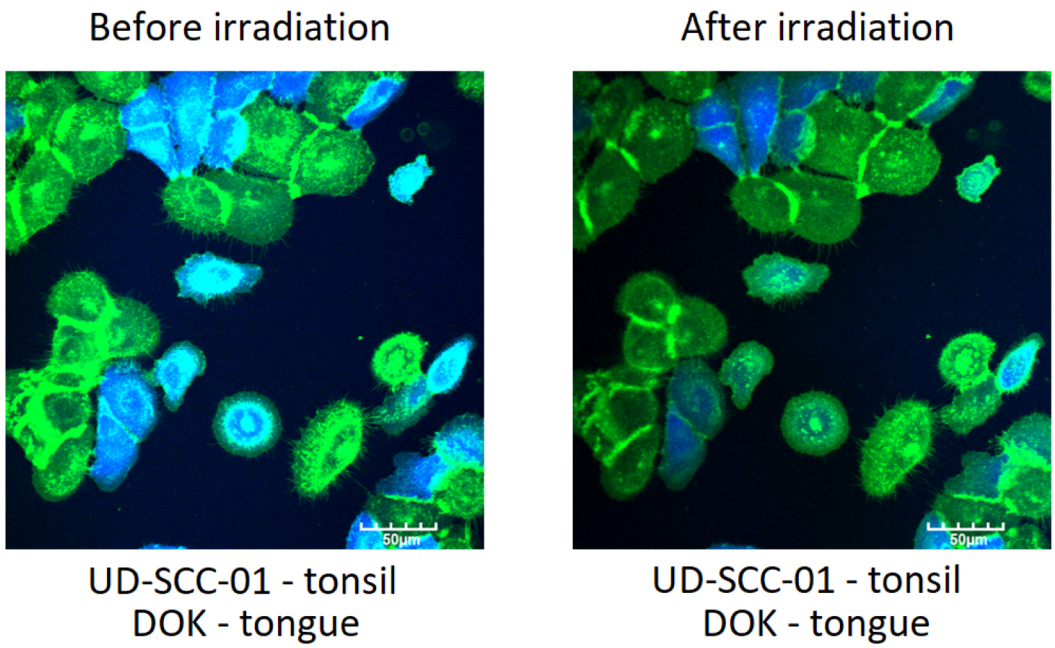

Figure 4.26: Cell reaction of DOK cells and UD-SCC-01 cells expressing BFP (blue) on acoustic wave irradiation

The images before and after the acoustic wave treatment show the reaction of the cells. It is hard to determine which cell line shows more reaction. Therefore, a software analysis is required. Table 4.14 shows the results of the measurement.

	DOK	UD-SCC-01 expressing BFP
Number of cells	13	9
Average (%)	−5	−5
Median (%)	−5	−5
Maximum (%)	6	8
Minimum (%)	−21	−14

Table 4.14: Cell area expansion of the DOK and UD-SCC-01 cells expressing BFP caused by acoustic wave irradiation

The average and median values of the expansion of the cell lines are equal with a value of 5%. The DOK and UD-SCC-01 cells observed in Subsection 4.3.6 displayed a similar reaction to the acoustic wave irradiation, therefore this result is expected. As the evaluation is made on single cells, a more detailed analysis of the results can be done. For instance, it can be noticed that both cell lines have a similar maximal expansion of the cells with 6% for DOK cells and 8% for UD-SCC-01 cells expressing BFP. The minimum expansion, which in this case means the maximal shrinking of the cells, as a reaction on the acoustic wave treatment, is observed at the DOK cell line with an expansion of -21%. The maximal expansion of the UD-SCC-01 cells is -14%. The similarity in the cell reaction of both observed cell lines may be caused by a similar amount of cytoskeleton filaments which mainly determine the elasticity of the cells.

The reactions of the UD-SCC-01 cells expressing BFP on the acoustic wave irradiation, when they are cultivated with UD-SCC-01 and DOK cells are comparable. This indicates that different cell lines, with which they are co-cultivated with, do not influence their elasticity markedly. If this is the case, those results are important for the future development of cancer treatment. In vivo, the tumor cells are surrounded by other healthy or dysplastic cells which may influence their elasticity and therewith their reaction on the acoustic wave treatment. Therefore, a different set of irradiation parameters must be used to destroy the cancer cells surrounded by cancer cells and the ones surrounded by healthy cells. As shown in this results, the reaction of the cells was comparable, no matter which cell line was used for co-cultivation. Thus, the acoustic waves used to destroy the cells can have the same properties for all the cells, regardless of their neighbouring cells.

Nevertheless, as this measurements were made in vitro and on a small sample they should be taken as fundamental research results. Further measurements on more cells combined with elasticity measurements of the co-cultivated cells should be performed.

5. Conclusion and outlook

During this thesis fundamental experiments, important for the development of a cell-selective treatment of squamous cell carcinoma were made. Even though cell death was not induced, the developed investigation methods and gained results are relevant for further research.

Using confocal laser scanning microscopy and a new developed software for (semi-) automatic segmentation of the cells and the calculation of their volume, an investigation of the morphology of healthy, dysplastic and cancer cells was enabled. Observing cell size, shape and the way the cells grew differences between healthy, dysplastic and cancer cells were noticed. Moreover, similarities between the cancer cells of the same origin were observed as well.

An analysis of microtubules and actin filaments was of interest, as the elasticity of the cells is mainly determined by the cytoskeleton. A comparison of three cell types showed that healthy and dysplastic cells have a greater actin to overall cell volume ratio than the ratio of microtubules, unlike the cancer cell lines which have greater microtubules volumes. Cell line UD-SCC-06 is an exception to this rule. The lack of actin filaments within the cancer cells could lead to a reduced elastic modulus of the cells. If that is the case, due to the proportionality of the elastic modulus and the resonance frequency, the cancer cells should react stronger on lower frequencies than healthy and dysplastic cells. Using atomic force microscopy, the elastic modulus of the observed cell lines should be determined and compared to prove this hypothesis.

Cytoskeleton filaments of cancer cell lines originating from tonsil, hypopharynx and tongue were compared. Based on the obtained results no clear statement whether the sample origin influences the cytoskeleton properties could be made. To do so, further research on more cell lines is required.

To better characterize the differences between the cell types, the volume of their active mitochondria was observed. Knowing that the metabolism of cancer cells is modified in comparison to healthy cells the question arises, whether cancer cells contain less active mitochondria. Analysing the mitochondrial structure, the density, the compactness and the volumes it appears, that the cancer cells contain more active mitochondria than healthy cells, despite the fact that cancer cells gain their energy out of mitochondria. Nevertheless, as there was only one healthy cell line observed, it should be examined whether the lack of mitochondria is a characteristic of the HOK cell line or the cancer cells generally contain more active mitochondria than healthy ones.

The main part of this thesis deals with the irradiation of the cells using acoustic waves exhibiting frequencies from 0.5 kHz to 10.0 kHz. The measurements revealed

important results for the development of super-selective ablation of squamous cell carcinoma. Parameters like frequency, oscillation amplitude, irradiation duration and probe-cells distance influence the reaction of the cells. Therefore, it is not important to find just the the right frequency to induce cell death, but a whole parameter set has to be determined.

The variation of irradiation duration has shown, as expected, that the cells react the most on the longest irradiation time. However, the natural movement and change of the cells, which is during the analysis also shown as cell reaction, increased with time. As there is no possibility to distinguish between a natural reaction of the cells and a reaction on the acoustic wave treatment, the irradiation time should be shortened to observe more reaction induced by acoustic waves.

Input voltage variation induces the variation of the probe's oscillation amplitude. The results demonstrated that the maximal reaction of the cells for different input voltages is also frequency dependent. Moreover, the technical limits of the experimental setup used have to be considered. For some frequencies, the trend of the cell reaction indicated that an increase of the input voltage could lead to a stronger reaction of the cells, which could not be tested due to setup limitations. Therefore, the operating range of the used setup has to be suitable for all experiments.

Probe-cells distance variation showed that the cell reaction is the strongest when the probe-cells distance is the lowest. In laboratory conditions, setting the probe-cells distance to 40 µm is not a problem. Nevertheless, in clinical use and in vivo, a precise determination of such a small distance is complex. Thus, all other parameters should be chosen to induce the most reaction in a way that the distance between the probe and the tumor can vary but the irradiation can still achieve a similar effect.

The frequency variation measurements have shown that the cell density influences the reaction of the cells as well. As the cells in a densely populated monolayer build more cell-cell contact, their cytoskeleton network, and thereby their elasticity, differ compared to the ones of the cells in a non-densely populated monolayer. Therefore, further measurements should be made on densely populated monolayers or even 3D cell culture, to achieve a better simulation of in vivo conditions.

The irradiation of non-densely populated monolayers where less than 50% of the Petri dish was covered with cells, pointed out an unwanted side effect. The acoustic waves detached the cells which do not adhere strongly. Further investigations have to be made to understand under which circumstances the cells can detach from the surface and move freely in the surrounding environment. The results can lead to the answer on the question how to stop the detachment of cells, which must be avoided in a human body.

A comparison of the reaction on the irradiation with different frequencies of the cell lines UD-SCC-01 and UD-SCC-04 demonstrated that cell line UD-SCC-04 has shown a stronger reaction on the frequencies up to 4.5 kHz, while the cell line UD-SCC-01 reacted more on the frequencies above 4.5 kHz. A reason for this could be the reduction of the cytoskeleton filament volumes of the cell line UD-SCC-04 compared to the UD-SCC-01. A similar observation was made after the irradiation of the cell lines UD-SCC-01 and UD-SCC-02 with the same parameter set. The cell line UD-SCC-02, which contains markedly less actin filaments, reacted stronger on

the irradiation than cell line UD-SCC-01. These results indicate that the cells with more cytoskeleton filaments react stronger on higher frequencies. Thus, to cause a resonance catastrophe and to induce cell death, the cells should be irradiated with frequencies higher than 10.0 kHz.

When the different cancer cell lines were treated using the same irradiation parameter, they showed different reactions. This leads to the conclusion that the cell-selective ablation will have to be customised for every patient individually.

Exemplarily, a co-cultivation of two different cell lines was made to simulate in vivo conditions. BFP expressed by one of the cell lines enables the distinguishment of the different cell lines and the observation of their reactions on acoustic wave irradiation. The cell line UD-SCC-01 expressing BFP was first co-cultivated with cell line UD-SCC-01 and afterwards with DOK. The cells with BFP showed similar reactions on the acoustic wave treatment, regardless of their neighbouring cells. This leads to the conclusion that the neighbouring cells do not have a strong influence on this cell line. However, as the measurements were performed on non-densely populated monolayers and on a small sample, the influence of the neighbouring cells has to be further investigated.

The presented results brought new findings regarding the development of super-selective ablation of squamous cell carcinoma cells using acoustic waves. Even though many open questions are still left before this kind of therapy can get in clinical use, this thesis sets a few milestones, important for further investigations and the development of a new, cell-selective therapy.

Appendices

A.

A.1 Concentration variation of SiR-tubulin for UD-SCC-01 cells

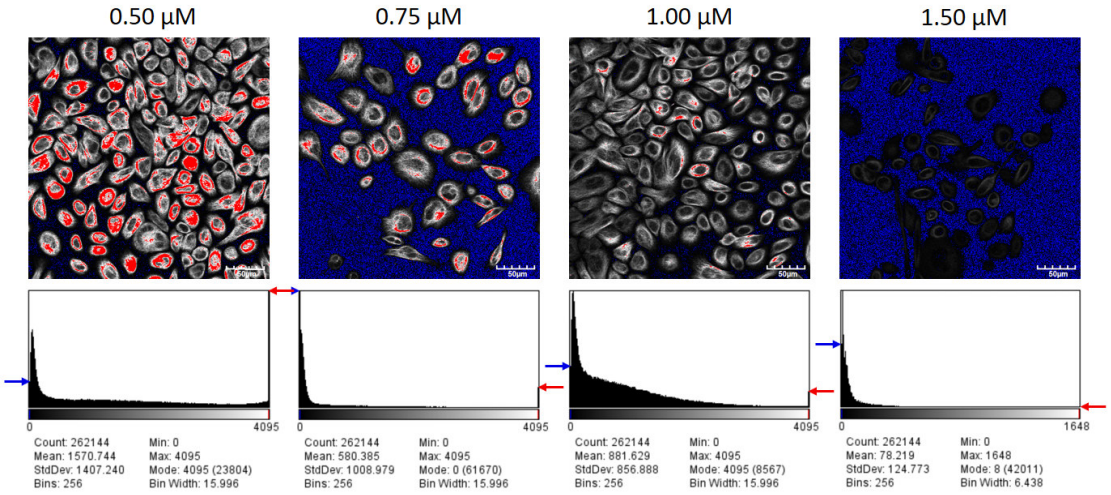

Figure A.1: Concentration variation of SiR-tubulin. (Staining time: 60 minutes; magnification: 40 times; laser power: 7.9 µW)

A.2 Staining time variation of SiR-tubulin for cell line UD-SCC-01

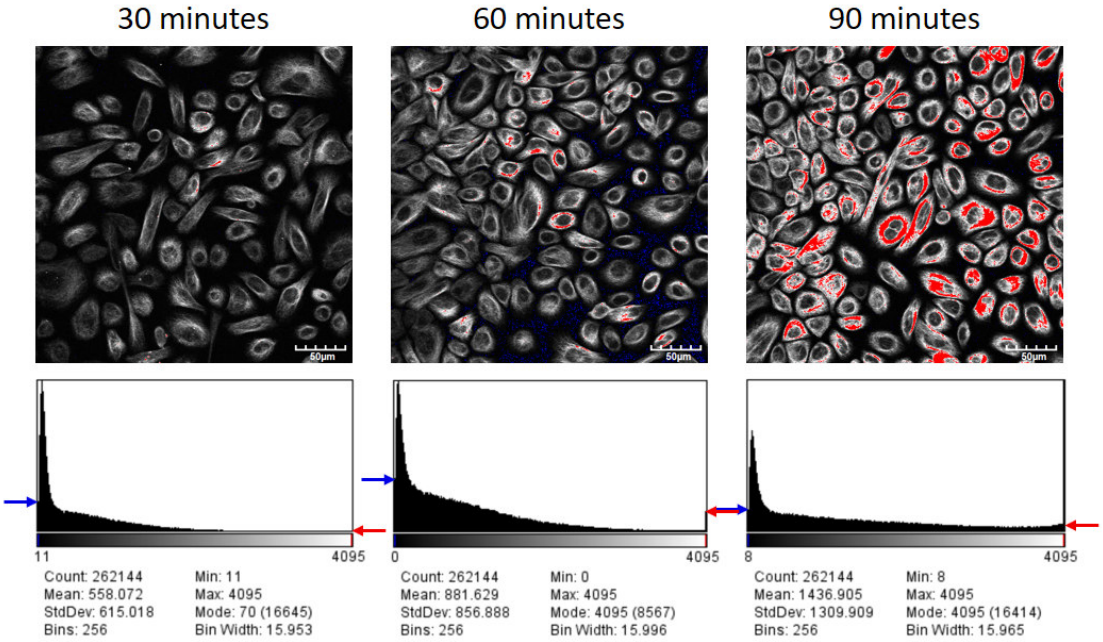

Figure A.2: Staining time variation of SiR-tubulin. (Staining concentration: 1.0 µM; magnification: 40 times; laser power: 7.9 µW)

B.

B.1 Concentration variation of SiR-actin for UD-SCC-01 cells

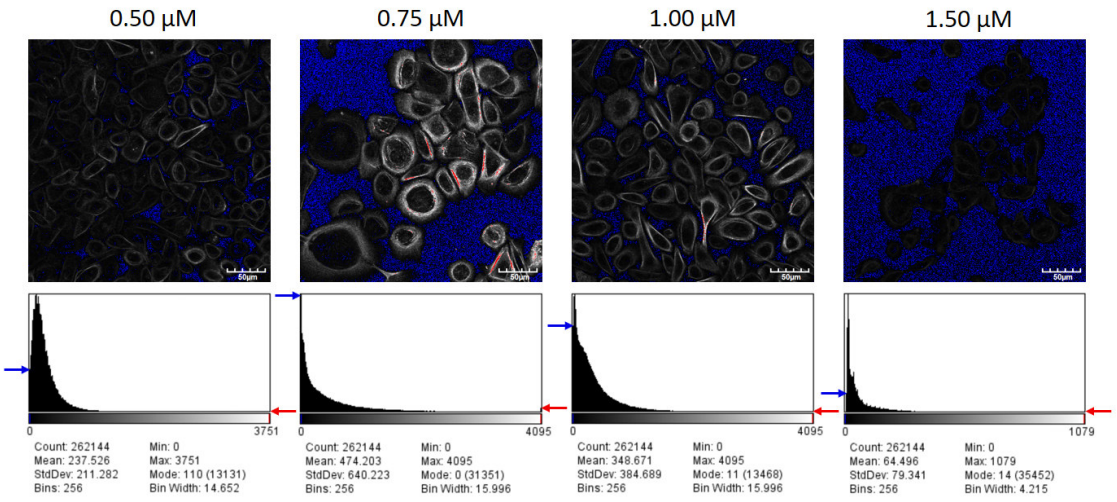

Figure B.1: Concentration variation of SiR-actin. (Staining time: 60 minutes; magnification: 40 times; laser power: 7.9 µW)

B.2 Staining time variation of SiR-actin for cell line UD-SCC-01

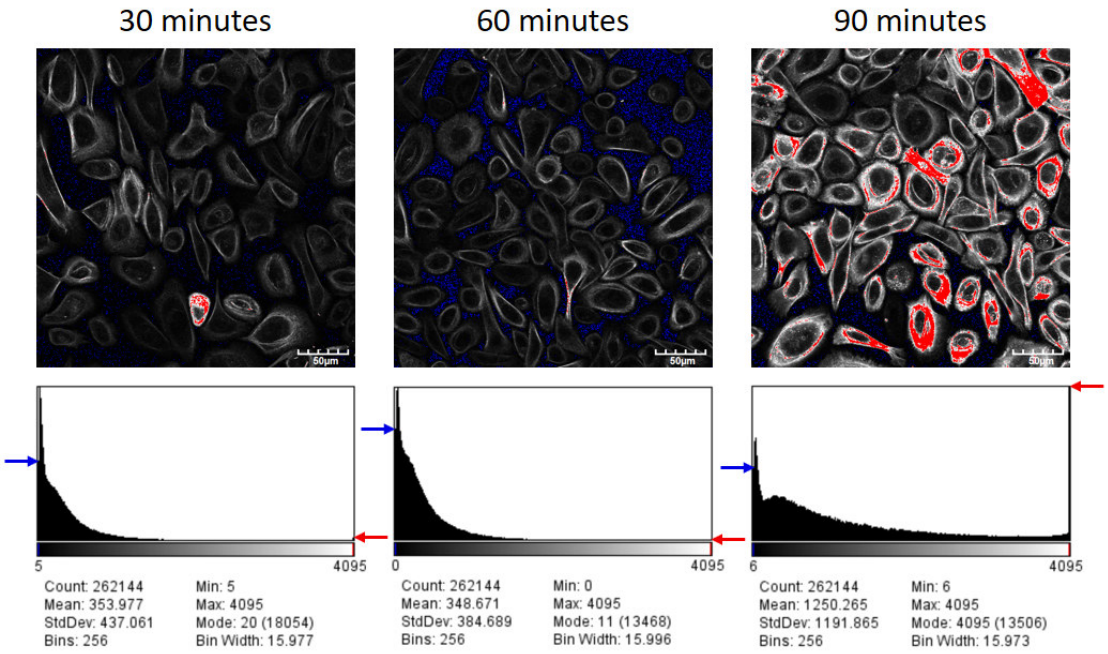

Figure B.2: Staining time variation of SiR-actin. (Staining concentration: 1.0 µM; magnification: 40 times; laser power: 7.9 µW)

C.

C.1 Concentration variation of Hoechst 33342 for UD-SCC-01 cells

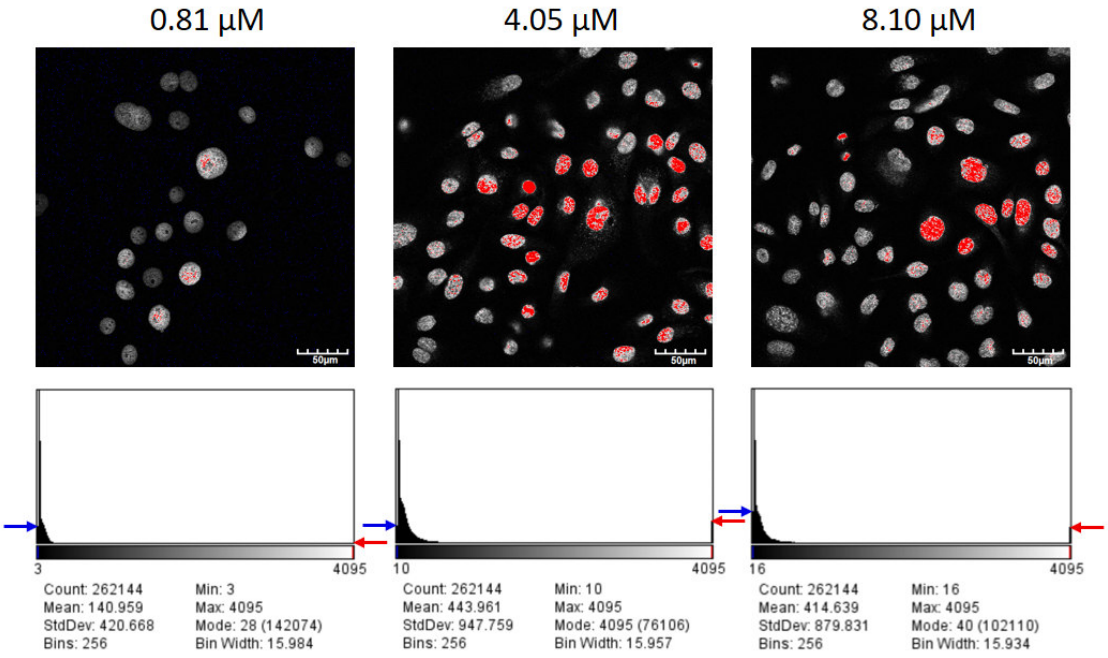

Figure C.1: Concentration variation of Hoechst 33342. (Staining time: 10 minutes; magnification: 40 times; laser power: 9.5 µW)

C.2 Staining time variation of Hoechst 33342 for cell line UD-SCC-01

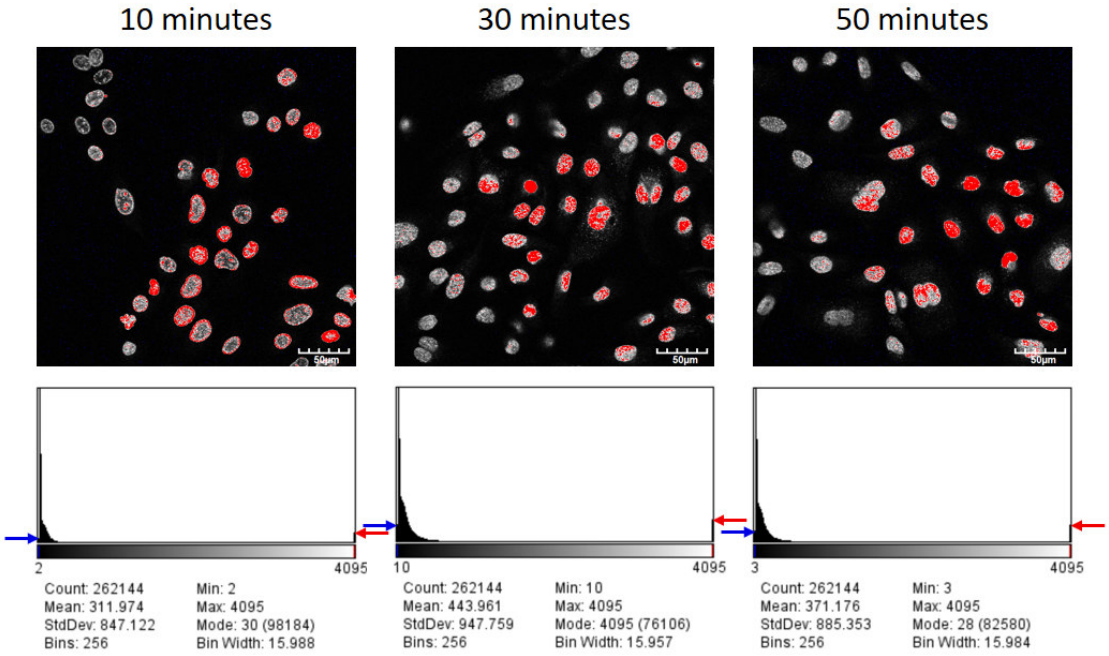

Figure C.2: Staining time variation of Hoechst 33342. (Staining concentration: 0.1 µM; magnification: 40 times; laser power: 9.5 µW)

D.

D.1 Concentration variation of MitoTracker Orange for UD-SCC-01 cells

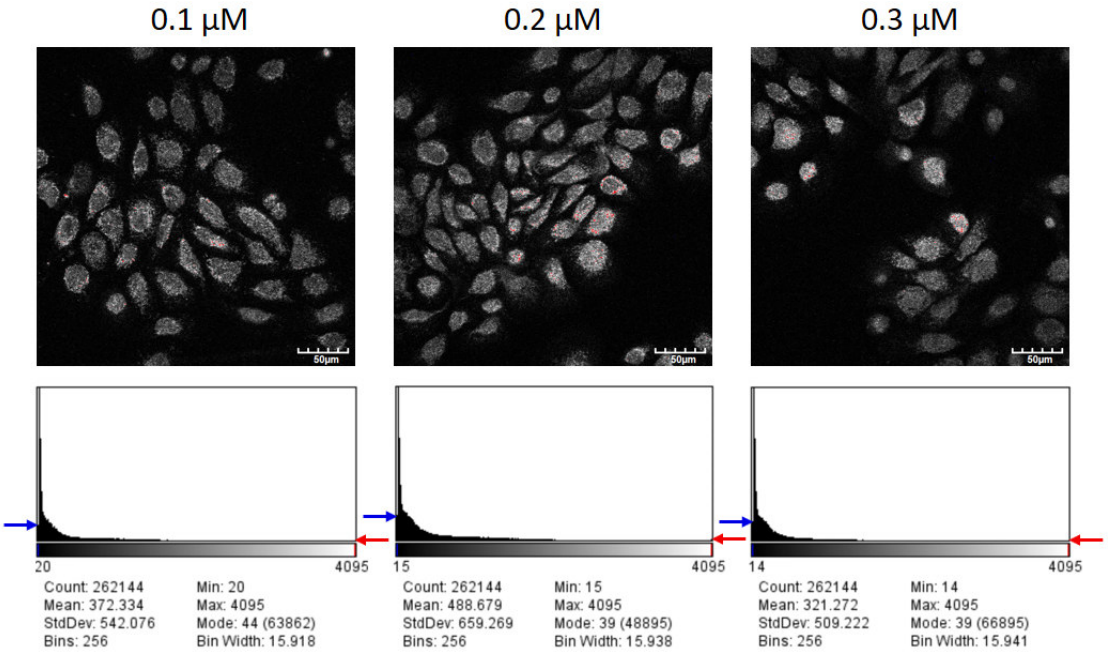

Figure D.1: Concentration variation of MitoTracker Orange. (Staining time: 10 minutes; magnification: 40 times; laser power: 14.2 µW)

D.2 Staining time variation of MitoTracker Orange for cell line UD-SCC-01

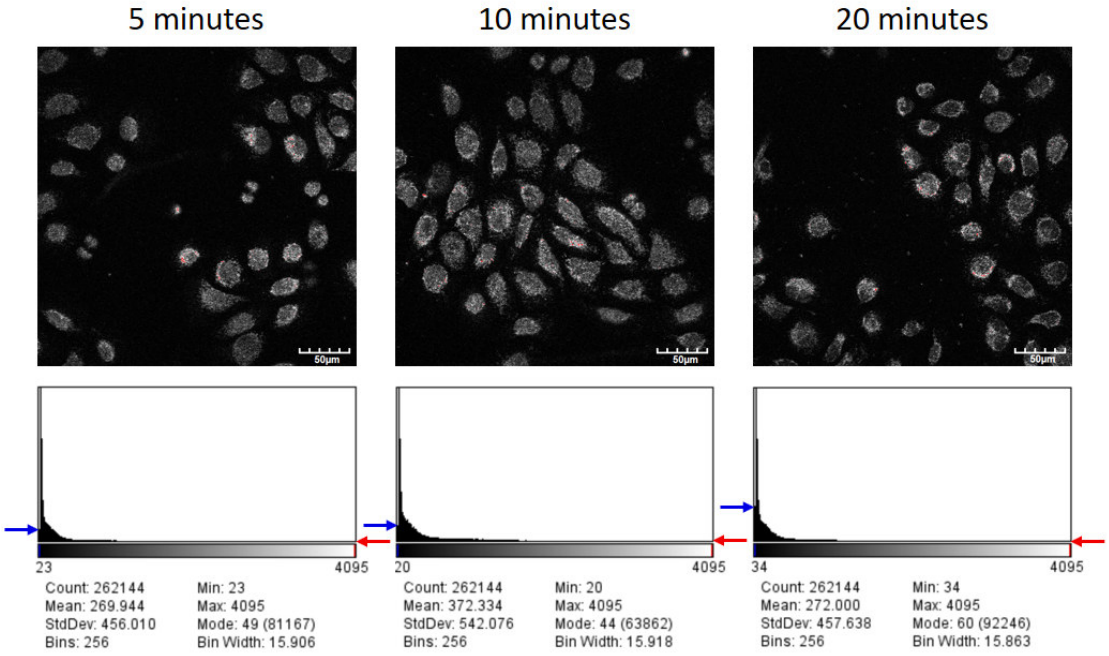

Figure D.2: Staining time variation of MitoTracker Orange. (Staining concentration: 0.1 µM; magnification: 40 times; laser power: 14.2 µW)

E.

E.1 Nuclei cross section of all observed cell lines

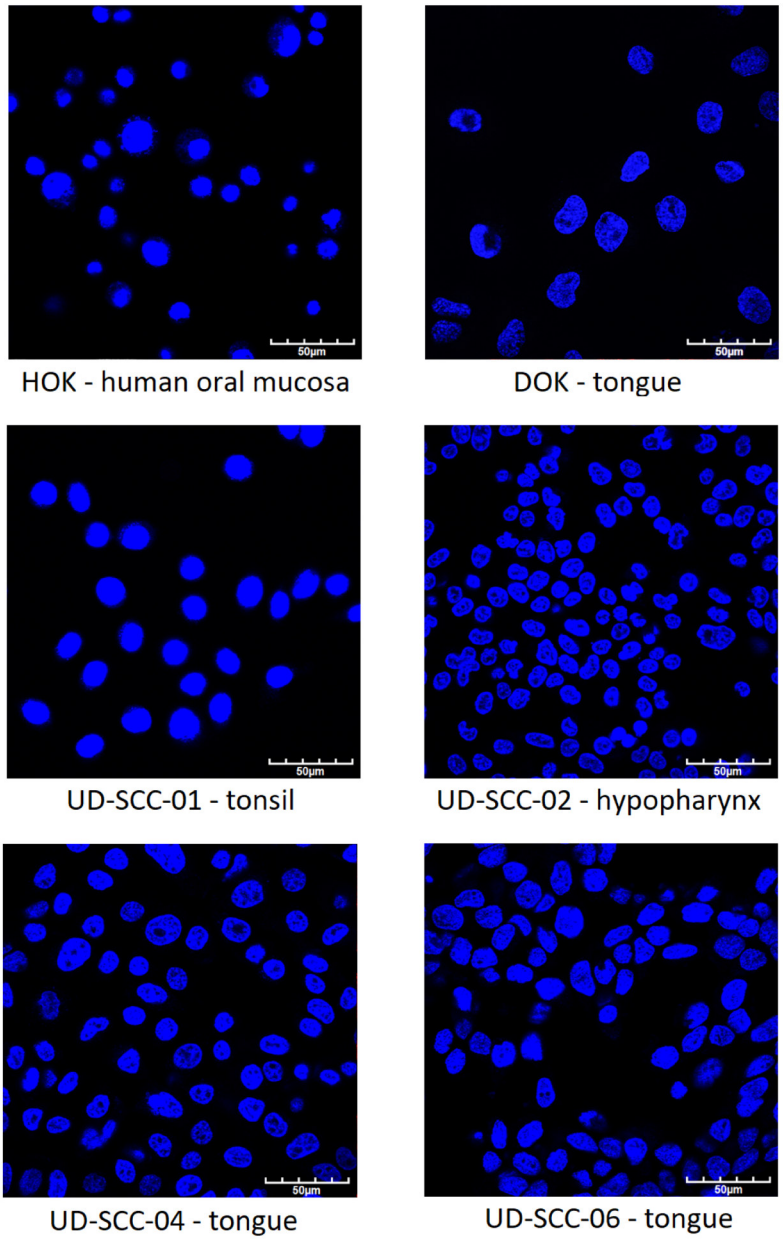

Figure E.1: Cell nuclei of observed cell lines

E.2 Distribution of the cell nuclei to overall cell volume ratios for all cell line used

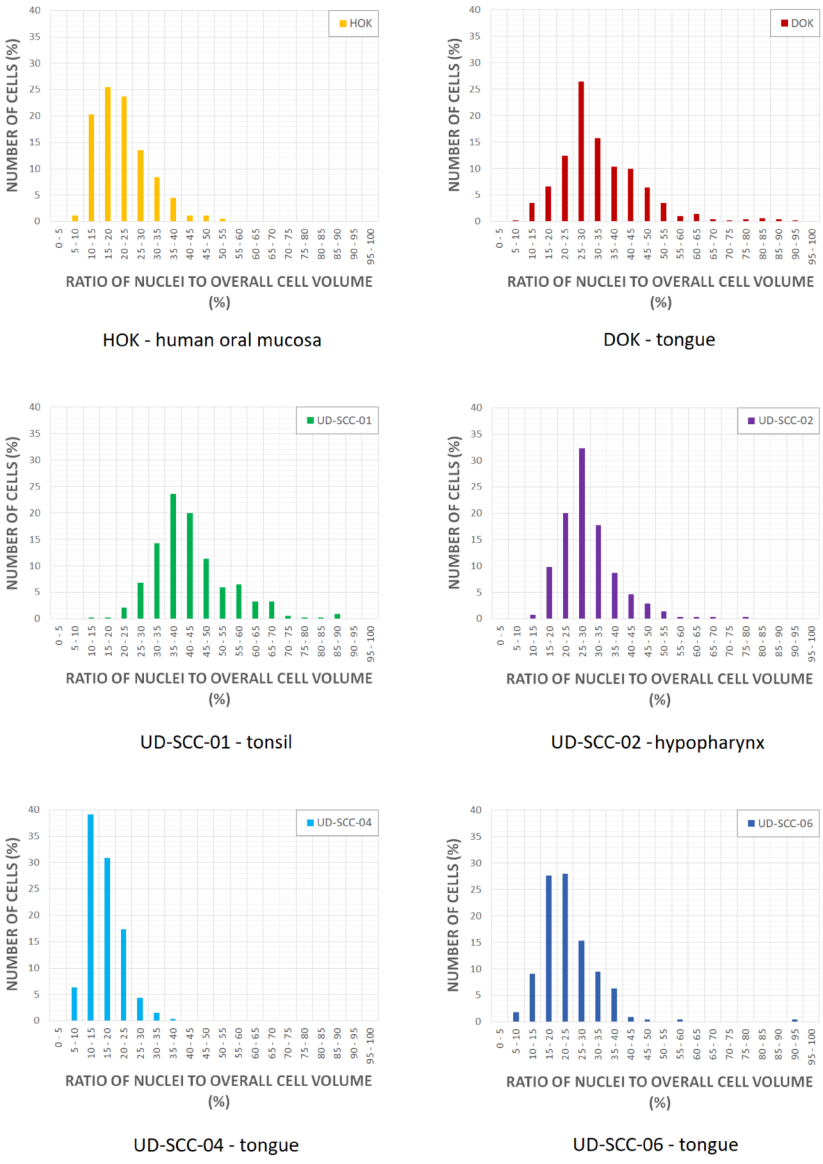

Figure E.2: Distribution of cell nuclei volumes

F.

F.1 Reaction of the UD-SCC-01 cells on irradiation with acoustic waves

Frequency (kHz)	Non-densely populated monolayer (%)	Densely populated monolayer (%)	Monolayer expressing BFP (%)
0.5	35	33	30
1.0	16	43	34
1.5	25	40	27
2.0	16	25	27
2.5	34	59	25
3.0	34	42	26
3.5	40	70	33
4.0	22	55	30
4.5	49	54	48
5.0	35	40	52
5.5	66	60	34
6.0	21	38	43
6.5	31	36	37
7.0	24	39	38
7.5	37	55	32
8.0	21	40	38
8.5	38	50	34
9.0	50	46	35
9.5	34	54	49
10.0	40	41	42

Table F.1: Cell reaction on irradiation with acoustic waves exhibiting frequencies from 0.5 kHz to 10.0 kHz

F.2 Reaction of the UD-SCC-04 cells on irradiation with acoustic waves

Frequency (kHz)	Cell reaction (%)
0.5	40
1.0	40
1.5	46
2.0	36
2.5	38
3.0	37
3.5	46
4.0	69
4.5	38
5.0	29
5.5	34
6.0	28
6.5	38
7.0	30
7.5	32
8.0	27
8.5	34
9.0	41
9.5	30
10.0	31

Table F.2: Cell reaction on irradiation with acoustic waves exhibiting frequencies from 0.5 kHz to 10.0 kHz

F.3 Comparison of the UD-SCC-04 and UD-SCC-01 cells' reaction on acoustic waves treatment

Frequency (kHz)	UD-SCC-01 (%)	UD-SCC-04 (%)
0.5	27	40
1.0	36	40
1.5	34	46
2.0	22	36
2.5	51	38
3.0	36	37
3.5	57	46
4.0	46	69
4.5	47	38
5.0	40	29
5.5	56	34
6.0	33	28
6.5	32	38
7.0	34	30
7.5	50	32
8.0	36	27
8.5	44	34
9.0	39	41
9.5	47	30
10.0	35	31

Table F.3: Cell reaction on irradiation with acoustic waves exhibiting frequencies from 0.5 kHz to 10.0 kHz

G.

G.1 Variation of irradiation duration for cell line UD-SCC-01

Frequency (kHz)	5 minutes (%)	10 minutes (%)	15 minutes (%)
0.5	19	27	33
1.0	30	36	43
1.5	29	34	40
2.0	19	22	25
2.5	42	51	59
3.0	32	36	42
3.5	40	57	70
4.0	34	46	55
4.5	39	47	54
5.0	39	40	40
5.5	49	56	60
6.0	28	33	38
6.5	28	32	36
7.0	28	34	39
7.5	39	50	55
8.0	29	36	40
8.5	32	44	50
9.0	33	39	46
9.5	37	47	54
10.0	28	35	41

Table G.1: Variation of irradiation duration for 5, 10 and 15 minutes

G.2 Variation of irradiation duration for cell line UD-SCC-04

Frequency (kHz)	5 minutes (%)	10 minutes (%)
0.5	35	40
1.0	36	40
1.5	36	46
2.0	36	36
2.5	34	38
3.0	35	37
3.5	34	46
4.0	59	69
4.5	31	38
5.0	26	29
5.5	29	34
6.0	25	28
6.5	35	38
7.0	28	30
7.5	29	32
8.0	24	27
8.5	32	34
9.0	36	41
9.5	35	30
10.0	23	31

Table G.2: Variation of irradiation duration for 5 and 10 minutes

H.

H.1 Variation of input voltages for UD-SCC-01 cells

Input voltage (%)	Input voltage for 2.5 kHz (V)	Input voltage for 7.5 kHz (V)	Input voltage for 9.0 kHz (V)
25	0.16	0.18	0.16
50	0.58	0.32	0.32
75	1.00	0.50	0.45
100	1.37	0.65	0.62
125	1.72	0.75	0.78
150	2.10	-	-

Table H.1: Input voltage for the frequencies of 2.5 kHz, 7.5 kHz and 9.0 kHz

H.2 Variation of input voltages for UD-SCC-04 cells

Input voltage (%)	Input voltage for 3.5 kHz (V)	Input voltage for 4.0 kHz (V)	Input voltage for 4.5 kHz (V)
25	0.37	0.20	0.16
50	0.73	0.39	0.29
75	1.14	0.55	0.54
100	1.35	0.80	0.70

Table H.2: Input voltage for the frequencies of 3.5 kHz, 4.0 kHz and 4.5 kHz

H.3 Cell reaction on input voltage variation for UD-SCC-01 cells

Input voltage (%)	Cell reaction for 2.5 kHz (%)	Cell reaction for 7.5 kHz (%)	Cell reaction for 9.0 kHz (%)
25	27	26	38
50	26	33	32
75	29	31	35
100	24	41	29
125	25	51	21
150	36	-	-

Table H.3: Cell reaction on input voltage variation for the frequencies of 2.5 kHz, 7.5 kHz and 9.0 kHz

H.4 Cell reaction on input voltage variation for UD-SCC-04 cells

Input voltage (%)	Cell reaction for 3.5 kHz (%)	Cell reaction for 4.0 kHz (%)	Cell reaction for 4.5 kHz (%)
25	29	36	26
50	39	43	28
75	30	28	31
100	32	31	30

Table H.4: Cell reaction on input voltage variation for the frequencies of 3.5 kHz, 4.0 kHz and 4.5 kHz

I.

I.1 Cell reaction on probe-cells distance variation for UD-SCC-01 cells

Probe-cells distance µm	Cell reaction for 2.5 kHz (%)	Cell reaction for 7.5 kHz (%)	Cell reaction for 9.0 kHz (%)
40	38	35	38
60	24	41	29
80	28	37	37
100	29	23	27

Table I.1: Cell reaction on probe-cells distance variation for the frequencies of 2.5 kHz, 7.5 kHz and 9.0 kHz

J.

J.1 Reaction of densely populated monolayers on acoustic wave irradiation

	DOK	UD-SCC-01	UD-SCC-02	UD-SCC-04	UD-SCC-06
Cell reaction	31%	32%	40%	18%	22%

Table J.1: Reaction of dysplastic and cancer cell lines on acoustic wave irradiation

J.2 Reaction of non-densely populated monolayers on acoustic wave irradiation

	DOK	UD-SCC-01	UD-SCC-02	UD-SCC-04	UD-SCC-06
Cell reaction	7%	13%	27%	33%	20%

Table J.2: Reaction of dysplastic and cancer cell lines on acoustic wave irradiation

Bibliography

[1] D. M. Parkin, F. Bray, J. Ferlay, and P. Pisani, "Estimating the world cancer burden: Globocan 2000," *International Journal of Cancer*, vol. 94, no. 2, pp. 153–156, 2001.

[2] N. Howlader, A. Noone, M. Krapcho, J. Garshell, D. Miller, S. Altekruse, C. Kosary, M. Yu, J. Ruhl, Z. Tatalovich, A. Mariotto, D. Lewis, H. Chen, E. Feuer, and K. Cronin, *SEER Cancer Statistics Review 1975-2011.*

[3] S. E. Cross, Y. S. Jin, J. Rao, and J. K. Gimzewski, "Nanomechanical analysis of cells from cancer patients," *Nat Nanotechnol*, vol. 2, no. 12, pp. 780–3, 2007.

[4] X. Guo, K. Bonin, K. Scarpinato, and M. Guthold, "The effect of neighboring cells on the stiffness of cancerous and non-cancerous human mammary epithelial cells," *New Journal of Physics*, vol. 16, 2014.

[5] M. Lekka, P. Laidler, D. Gil, J. Lekki, Z. Stachura, and A. Z. Hrynkiewicz, "Elasticity of normal and cancerous human bladder cells studied by scanning force microscopy," *European Biophysics Journal*, vol. 28, pp. 312–316, 1999.

[6] P. Gupta, *Cell and Molecular Biology.* Rastogi Publications, 2005.

[7] D. Sadava, *Cell Biology: Organelle Structure and Function.* Jones and Bartlett Publishers, 1993.

[8] B. Alberts, A. Johnson, J. Lewis, and e. al., *Molecular Biology of the Cell.* New York: Garland Science, 4th ed., 2002.

[9] H. M. McBride, M. Neuspiel, and S. Wasiak, "Mitochondria: more than just a powerhouse," *Curr Biol*, vol. 16, no. 14, pp. R551–60, 2006.

[10] D. A. Fletcher and R. D. Mullins, "Cell mechanics and the cytoskeleton," *Nature*, vol. 463, no. 7280, pp. 485–92, 2010.

[11] C. Rosette and M. Karin, "Cytoskeletal control of gene expression: depolymerization of microtubules activates nf-kappa b," *The Journal of Cell Biology*, vol. 128, p. 1111–1119, 1995.

[12] G. M. Cooper, *The Cell: A Molecular Approach.* Sunderland: Sinauer Associates, 2000.

[13] M. Guo, A. J. Ehrlicher, S. Mahammad, H. Fabich, M. H. Jensen, J. R. Moore, J. J. Fredberg, R. D. Goldman, and D. A. Weitz, "The role of vimentin intermediate filaments in cortical and cytoplasmic mechanics," *Biophys J*, vol. 105, no. 7, pp. 1562–8, 2013.

[14] Y. W. Heng and C. G. Koh, "Actin cytoskeleton dynamics and the cell division cycle," *Int J Biochem Cell Biol*, vol. 42, no. 10, pp. 1622–33, 2010.

[15] L. Wilkins and J. King, *Anatomy and Physiology*. Lippincott Williams & Wilkins, 2002.

[16] A. Van Lommel, *From Cells to Organs: A Histology Textbook and Atlas*. Springer US, 2012.

[17] B. Young, *Wheater's Functional Histology: A Text and Colour Atlas*. Churchill Livingstone/Elsevier, 2006.

[18] D. Morgan and D. Morgan, *The Cell Cycle: Principles of Control*. OUP/New Science Press, 2007.

[19] S. Nagata and H. Nakano, *Apoptotic and Non-apoptotic Cell Death*. Springer International Publishing, 2017.

[20] P. Syntichaki and N. Tavernarakis, "Death by necrosis. uncontrollable catastrophe, or is there order behind the chaos?," *EMBO Rep*, vol. 3, no. 7, pp. 604–9, 2002.

[21] G. Colditz and D. Hunter, *Cancer Prevention: The Causes and Prevention of Cancer — Volume 1: The Causes and Prevention of Cancer*. Springer Netherlands, 2000.

[22] A. Baba and C. Câtoi, *Comparative Oncology*. Bucharest: The Publishing House of the Romanian Academy, 2007.

[23] J. Katsantonis, A. Tosca, S. B. Koukouritaki, P. A. Theodoropoulos, A. Gravanis, and C. Stournaras, "Differences in the g/total actin ratio and microfilament stability between normal and malignant human keratinocytes," *Cell Biochem Funct*, vol. 12, no. 4, pp. 267–74, 1994.

[24] A. L. Parker, M. Kavallaris, and J. A. McCarroll, "Microtubules and their role in cellular stress in cancer," *Front Oncol*, vol. 4, p. 153, 2014.

[25] M. E. Kidd, D. K. Shumaker, and K. M. Ridge, "The role of vimentin intermediate filaments in the progression of lung cancer," *Am J Respir Cell Mol Biol*, vol. 50, no. 1, pp. 1–6, 2014.

[26] O. Warburg, F. Wind, and E. Negelein, "The metabolism of tumors in the body," *The Journal of General Physiology*, p. 519–530, 1927.

[27] A. Singh, *Mechanics of solids*. PHI Learning, 2007.

[28] J. Gere and B. Goodno, *Mechanics of Materials*. Cengage Learning, 2008.

[29] K. Y. Billah and R. H. Scanlan, "Resonance, tacoma narrows bridge failure, and undergraduate physics textbooks," *American Journal of Physics*, vol. 59, no. 2, pp. 118–124, 1991.

[30] Z. Glumac, *Klasicna mehanika kratak uvod*
http : //gama.fizika.unios.hr/ zglumac/utm.pdf 08.08.2018.

[31] ASTM, *Standard Test Method for Dynamic Young's Modulus, Shear Modulus, and Poisson's Ratio by Impulse Excitation of Vibration*. ASTM International, 2006.

[32] M. Fraldi, A. Cugno, L. Deseri, K. Dayal, and N. M. Pugno, "A frequency-based hypothesis for mechanically targeting and selectively attacking cancer cells," *J R Soc Interface*, vol. 12, no. 111, p. 20150656, 2015.

[33] H. Zhang and K. K. Liu, "Optical tweezers for single cells," *J R Soc Interface*, vol. 5, no. 24, pp. 671–90, 2008.

[34] J. Guck, S. Schinkinger, B. Lincoln, F. Wottawah, S. Ebert, M. Romeyke, D. Lenz, H. M. Erickson, R. Ananthakrishnan, D. Mitchell, J. Kas, S. Ulvick, and C. Bilby, "Optical deformability as an inherent cell marker for testing malignant transformation and metastatic competence," *Biophys J*, vol. 88, no. 5, pp. 3689–98, 2005.

[35] N. Wang, J. Butler, and D. Ingber, "Mechanotransduction across the cell surface and through the cytoskeleton," *Science*, vol. 260, no. 5111, pp. 1124–1127, 1993.

[36] E. A-Hassan, W. F. Heinz, M. D. Antonik, N. P. D'Costa, S. Nageswaran, C.-A. Schoenenberger, and J. H. Hoh, "Relative microelastic mapping of living cells by atomic force microscopy," *Biophysical Journal*, vol. 74, no. 3, pp. 1564–1578, 1998.

[37] Q. S. Li, G. Y. Lee, C. N. Ong, and C. T. Lim, "Afm indentation study of breast cancer cells," *Biochem Biophys Res Commun*, vol. 374, no. 4, pp. 609–13, 2008.

[38] C. Rotsch, F. Braet, E. Wisse, and M. Radmacher, "Afm imaging and elasticity measurements on living rat liver macrophages," *Cell Biol Int*, vol. 21, no. 11, pp. 685–96, 1997.

[39] H. Haga, S. Sasaki, K. Kawabata, E. Ito, T. Ushiki, and T. Sambongi, "Elasticity mapping of living fibroblasts by afm and immunofluorescence observation of the cytoskeleton," *Ultramicroscopy*, vol. 82, no. 1-4, pp. 253–258, 2000.

[40] N. Caille, O. Thoumine, Y. Tardy, and J.-J. Meister, "Contribution of the nucleus to the mechanical properties of endothelial cells," *Journal of Biomechanics*, vol. 35, no. 2, pp. 177–187, 2002.

[41] F. Guilak, J. R. Tedrow, and R. Burgkart, "Viscoelastic properties of the cell nucleus," *Biochem Biophys Res Commun*, vol. 269, no. 3, pp. 781–6, 2000.

[42] J. Solon, I. Levental, K. Sengupta, P. C. Georges, and P. A. Janmey, "Fibroblast adaptation and stiffness matching to soft elastic substrates," *Biophys J*, vol. 93, no. 12, pp. 4453–61, 2007.

[43] R. Sunyer, X. Trepat, J. J. Fredberg, R. Farre, and D. Navajas, "The temperature dependence of cell mechanics measured by atomic force microscopy," *Phys Biol*, vol. 6, no. 2, p. 025009, 2009.

[44] P. Bunker, *Molecular Symmetry and Spectroscopy*. Canadian Science Publishing (NRC Research Press), 2nd revised edition ed.

[45] A. Jablonski, "Efficiency of anti-stokes fluorescence in dyes," *Nature*, vol. 131, no. 3319, pp. 839–840, 1933.

[46] J. Lakowicz, *Principles of Fluorescence Spectroscopy*. Springer US, 2007.

[47] B. Valeur and M. Berberan-Santos, *Molecular Fluorescence: Principles and Applications*. Wiley, 2013.

[48] G. G. Stokes, "On the change of refrangibility of light," *Philosophical Transactions of the Royal Society of London*, vol. 142, no. 0, pp. 463–562, 1852.

[49] M. Minsky, *Microscopy apparatus, patent: US3013467A* *https : //patents.google.com/patent/US*3013467*A/en 12.08.2018*.

[50] J. Pawley, *Handbook of Biological Confocal Microscopy*. Springer US, 2012.

[51] G. Kino and T. Corle, *Confocal Scanning Optical Microscopy and Related Imaging Systems*. Elsevier Science, 1996.

[52] U. Kubitscheck, *Fluorescence Microscopy: From Principles to Biological Applications*. Wiley, 2017.

[53] M. Mulisch and U. Welsch, *Romeis - Mikroskopische Technik*. Springer Berlin Heidelberg, 2015.

[54] J. Stockert and A. Blazquez-Castro, *Fluorescence Microscopy in Life Sciences*. Bentham Science Publishers, 2017.

[55] A. Ettinger and T. Wittmann, "Fluorescence live cell imaging," *Methods Cell Biol*, vol. 123, pp. 77–94, 2014.

[56] L. Song, E. J. Hennink, I. T. Young, and H. J. Tanke, "Photobleaching kinetics of fluorescein in quantitative fluorescence microscopy," *Biophys J*, vol. 68, pp. 2588–2600, 1995.

[57] V. Vogel, D. Schubert, and C. Stiebing, *Fluoreszenzspektroskopie* *http : //www.biophys.uni − frankfurt.de/ wille/prakt/anleitungen/*04$_f$*luoreszenz.pdf 20.08.2018*.

[58] W. Renier, A. Joubert, Z. Bencokova, J. Gastaldo, C. Massart, and N. Foray, "Consequences of the bleed-through phenomenon in immunofluorescence of proteins forming radiation-induced nuclear foci," *Int J Radiat Biol*, vol. 83, no. 8, pp. 543–9, 2007.

[59] L. Björn, *Photobiology: The Science of Light and Life.* Springer New York, 2015.

[60] M. Kreft, M. Stenovec, and R. Zorec, "Focus-drift correction in time-lapse confocal imaging," *Ann N Y Acad Sci*, vol. 1048, pp. 321–30, 2005.

[61] P. Mittal, *Oscillations, Waves and Acoustics.* I.K. International Publishing House Pvt. Limited, 2010.

[62] O. Dössel, *Bildgebende Verfahren in der Medizin: Von der Technik zur medizinischen Anwendung.* Springer Berlin Heidelberg, 2016.

[63] Z. Nazarchuk, V. Skalskyi, and O. Serhiyenko, *Acoustic Emission.* Foundations of Engineering Mechanics, Springer International Publishing, 2017.

[64] S. Rupitsch, *Piezoelectric Sensors and Actuators: Fundamentals and Applications.* Springer Berlin Heidelberg, 2018.

[65] D. Collins, *What are piezo actuators?*
https : //www.linearmotiontips.com/what − are − piezo − actuators/
16.08.2018.

[66] Y. Ronald, *Cavitation.* World Scientific Publishing Company, 1999.

[67] S. Thuroff, C. Chaussy, G. Vallancien, W. Wieland, H. J. Kiel, A. Le Duc, F. Desgrandchamps, J. J. De La Rosette, and A. Gelet, "High-intensity focused ultrasound and localized prostate cancer: efficacy results from the european multicentric study," *J Endourol*, vol. 17, no. 8, pp. 673–7, 2003.

[68] K. Yasui, *Acoustic Cavitation and Bubble Dynamics.* Springer International Publishing, 2017.

[69] A. E. Theuer, *Vorrichtung zur Zerstörung von Tumorzellen und Tumorgewebe, patent: DE102008030213*
*http : //www.freepatentsonline.com/DE*102008030213*.html 18.08.2018.*

[70] H. Ballo, P. Koldovsky, T. Hoffmann, V. Balz, B. Hildebrandt, C. D. Gerharz, and H. Bier, "Establishment and characterization of four cell lines derived from human head and neck squamous cell carcinomas for an autologous tumor-fibroblast in vitro model," *Anticancer Res*, vol. 19, no. 5B, pp. 3827–36, 1999.

[71] Sigma-Aldrich, "Dok 94122104."

[72] Sciencell-Research-Laboratories, *Human Oral Keratinocytes 2610*
https : //www.sciencellonline.com/human − oral − keratinocytes.html
20.08.2018.

[73] Sciencell-Research-Laboratories, *Oral Keratinocyte Medium* *https : //www.sciencellonline.com/oral − keratinocyte − medium.html 20.08.2018.*

[74] ThermoFisher-Scientific, *CellMask™ Green Plasma Membrane Stain* *http : //www.thermofisher.com/order/catalog/product/C*37608 *21.08.2018.*

[75] Spirochrome, *Cytoskeleton Kit (SiR-Actin and SiR-Tubulin)* *https : //www.cytoskeleton.com/live − cell − reagents/spirochrome/ cytoskeleton − kit 21.08.2018.*

[76] A. Holzinger, "Jasplakinolide: an actin-specific reagent that promotes actin polymerization," *Methods Mol Biol*, vol. 586, pp. 71–87, 2009.

[77] ThermoFisher-Scientific, *Hoechst 33342, Trihydrochloride, Trihydrate - 10 mg/mL Solution in Water* *http : //www.thermofisher.com/order/catalog/product/H*3570 *21.08.2018.*

[78] ThermoFisher-Scientific, *MitoTracker™ Orange CMTMRos* *http : //www.thermofisher.com/order/catalog/product/M*7510 *21.08.2018.*

[79] Olympus, *Fluoview—Always Evolving, http : //anyflip.com/dndt/ogiq/basic 23.08.2018.*

[80] B. Bramfitt and A. Benscoter, *Metallographer's Guide: Practice and Procedures for Irons and Steels.* ASM International, 2001.

[81] Zeiss, *Numerical Aperture and Resolution https : //www.zeiss.com/microscopy/int/solutions/reference/all − tutorials/basic − microscopy/coverslip − thickness − correction.html 21.08.2018.*

[82] T. Scientific, "Amira for advanced image processing and quantification," 09 2018.

[83] Oxford-instruments, *Voloom, http : //www.bitplane.com/imaris/voloom 04.06.2018.*

[84] M. Merzin, *Applying stereological method in radiology. Volume measurement. http : //lepo.it.da.ut.ee/ markkom/volumest/, 05.09.2018.*

[85] P. Instrumente, "P-840 preloaded piezo actuators."

[86] T. ilastik developers, *Ilastik: the interactive learning and segmentation toolkit, http : //ilastik.org/, 04.09.2018.*

Publications

M. Strugačevac, N. Ullrich, C. Wiek, J. Schipper, M. Getzlaff, and J. Kristin. *Development of a new software for (semi-) automatic segmentation of 3D-objects.* Submitted to *Review of Scientific Instruments*, October 2018.

Conference contributions

M. Strugačevac, N. Bartels, T. Löffler, C. Wiek, J. Kristin, M. Glaas, J. Schipper, and M. Getzlaff. *Investigation of the cells behaviour exposed to acoustic waves* (Poster presentation). Dynamic cell III, March 2018, Manchester, UK.

N. Bartels, M. Strugačevac, J. Kristin, C. Wiek, J. Schipper, and M. Getzlaff. *Cytoskeletal morphology of oral keratinocytes and oral carcinoma cells* (Poster presentation). Dynamic cell III, March 2018, Manchester, UK.

M. Strugačevac, N. Bartels, T. Löffler, C. Wiek, M. Glaas, J. Schipper, and M. Getzlaff. *Treatment of cancer cells with acoustic waves* (Talk).DPG-Frühjahrstagung, March 2018, Berlin, Germany.

S. Krüger, T. Löffler, M. Strugačevac, J. Kristin, C. Wiek, J. Schipper, and M. Getzlaff. *Adjustment of pulsed laser radiation for stroboscopic experiments* (Poster presentation). DPG-Frühjahrstagung, March 2018, Berlin, Germany.

L. Hentschel, M. Strugačevac, C. Wiek, J. Kristin, M. Glaas, J. Schipper, and M. Getzlaff. *Lentiviral infection leads to blue fluorescent labeling of cancer cells* (Poster presentation). DPG-Frühjahrstagung, March 2018, Berlin, Germany.

T. Löffler, S. Krüger, M. Strugačevac, J. Kristin, C. Wiek, M. Glaas, J. Schipper, and M. Getzlaff. *Characterization of a piezoelectric actuator for output power and thermal behaviour* (Poster presentation). DPG-Frühjahrstagung, March 2018, Berlin, Germany.

N. Bartels, M. Strugačevac, N. Ullrich, J. Kristin, C. Wiek, J. Schipper, and M. Getzlaff. *Cytoskeletal morphology of oral keratinocytes and oral carcinoma cells* (Poster presentation). DPG-Frühjahrstagung, March 2018, Berlin, Germany.

L. Rohde, M. Strugačevac, N. Bartels, C. Wiek, J. Kristin, M. Glaas, J. Schipper, and M. Getzlaff. *Is the size of a cell nucleus an indicator for cancer?* (Poster presentation). DPG-Frühjahrstagung, March 2018, Berlin, Germany.

M. Plettenberg, M. Strugačevac, C. Wiek, J. Kristin, M. Glaas, J. Schipper, and M. Getzlaff. *Comparison of the cytoskeleton of squamous cells using fluorescence microscopy* (Poster presentation). DPG-Frühjahrstagung, March 2018, Berlin, Germany.

N. Bartels, M. Strugačevac, C. Wiek, J. Kristin, M. Glaas, J. Schipper, and M. Getzlaff. *Investigations on the cell morphology of oral mucosa cancer and non-cancer cells* (Talk). DPG-Frühjahrstagung, March 2018, Berlin, Germany.

M. Strugačevac, N. Bartels, M. Plettenberg, L. Rohde, S. Steeger, C. Wiek, J. Kristin, M. Glaas, J. Schipper, and M. Getzlaff. *Comparison of the cell morphology between healthy and cancerous oral mucosa* (Poster presentation). 10. znanstveni sastanak HFD-a, October 2017, Baška, Croatia.

L. Hentschel, M. Strugačevac, C. Wiek, J. Kristin, M. Glaas, J. Schipper, and M. Getzlaff. *Blue fluorescent protein as marker for carcinoma cells* (Poster presentation). Physics of Cancer, October 2017, Leipzig, Germany.

M. Strugačevac, N. Bartels, M. Plettenberg, L. Rohde, S. Steeger, C. Wiek, J. Kristin, M. Glaas, J. Schipper, and M. Getzlaff. *Comparison of the cell morphology between healthy and cancerous oral mucosa* (Poster presentation). Physics of Cancer, October 2017, Leipzig, Germany.

M. Strugačevac, S. Steeger, J. Kristin, M. Glaas, J. Schipper, and M. Getzlaff. *Comparative cytoskeleton and elasticity investigation on healthy and cancerous oral mucosa* (Poster presentation). 19^{th} IUPAB congress and 11^{th} EBSA congress, March 2017, Edinburgh, UK.

M. Strugačevac, S. Steeger, J. Lietz, J. Kristin, M. Glaas, J. Schipper, and M. Getzlaff. *Investigations of squamous cell carcinoma cells and dysplastic oral keratinocytes* (Talk). DPG-Frühjahrstagung, March 2017, Dresden, Germany.

J. Lietz, M. Strugačevac, A. Almaci, J. Kristin, M. Glaas, J. Schipper, and M. Getzlaff. *Staining of squamous cell carcinoma cells and dysplastic oral keratinocytes* (Poster presentation). DPG-Frühjahrstagung, March 2017, Dresden, Germany.

N. Bartels, M. Strugačevac, S. Steeger, J. Lietz, J. Kristin, M. Glaas, J. Schipper, and M. Getzlaff. *Investigations of the cytoskeleton of squamous cell carcinoma cells and oral keratinocytes* (Poster presentation). DPG-Frühjahrstagung, March 2017, Dresden, Germany.

M. Strugačevac, S. Steeger, N. Bartels, J. Lietz, J. Kristin, M. Glaas, J. Schipper, and M. Getzlaff. *Investigations of Single Squamous Cell Carcinoma Cells* (Poster presentation). Physics of Cancer, October 2016, Leipzig, Germany.

Acknowledgements

Firstly, I would like to thank Prof. Dr. Mathias Getzlaff and Prof. Dr. med. Dr. h.c. Jörg Schipper for the opportunity to do my doctoral thesis in the working group at Institute of Applied Physics at Heinrich-Heine-University in Düsseldorf in cooperation with Düsseldorf University Hospital, Department of Otorhinolaryngology. Moreover, many thanks for the mentoring and the continuous support of my doctoral study and related research.

Many thanks to Düsseldorf School of Oncology for the possibility to take part on the lectures and workshops relevant for my work as well as the financial support.

My sincere thanks goes to the personnel of the Düsseldorf University Hospital, Department of Otorhinolaryngology and their research laboratory who supported me during the whole thesis. Especially Dr. med. Julia Kristin and Dr. Constanze Wiek who supported me with their knowledge of medicine and biology important to carry out this work.

Many thanks to my colleagues and students at the Institute of Applied Physics for the encouragement, the assistance and the shared time. Above all, I would like to thank Dr. Hendrik Bettermann for the support from the start of my thesis to the very end and proofreading of this thesis. Moreover, many thanks to Mr. Tobias Löffler for the technical support and laboratory work.

Additionally, I would like to thank the Institute of Molecular Physical Chemistry for giving me the access to the laboratory and research facilities as well as to their co-workers Dr. Annemarie Greife and Dr. Ralf Kühnemuth for the assistance during my work in the laboratory.

I would like to acknowledge Center of Advanced Imaging for providing the microscope and their manager Dr. Stefanie Weidtkamp-Peters for the technical support.

Finally, many thanks to my families for all the personal support they gave and give. Most of all, I would like to thank Mr. Niklas Ullrich for the development of the software required for data evaluation as well as for proofreading of this thesis. Moreover, Mr. Ullrich was the greatest support not just during my work in Düsseldorf, but over the course of the last years.

Eidesstattliche Versicherung

Ich versichere an Eides Statt, dass die Dissertation von mir selbständig und ohne unzulässige fremde Hilfe unter Beachtung der "Grundsätze zur Sicherung guter wissenschaftlicher Praxis an der Heinrich-Heine-Universität Düsseldorf" erstellt worden ist.
Ferner erkläre ich, dass ich nicht anderweitig mit oder ohne Erfolg versucht habe, eine Dissertation einzureichen oder mich der Doktorprüfung zu unterziehen.

Düsseldorf, den 19. November 2018

Maja Strugačevac